

Application of Nonlinear Dynamic Systems and Joint-Time Frequency Analyses for Biomedical Signals

Lead Guest Editor: Kunal Pal

Guest Editors: Sumit Chakravarty and Arfat Anis





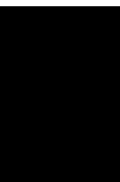
**Application of Nonlinear Dynamic Systems and
Joint-Time Frequency Analyses for Biomedical
Signals**

Journal of Healthcare Engineering

**Application of Nonlinear Dynamic
Systems and Joint-Time Frequency
Analyses for Biomedical Signals**

Lead Guest Editor: Kunal Pal

Guest Editors: Sumit Chakravarty and Arfat Anis



Copyright © 2023 Hindawi Limited. All rights reserved.

This is a special issue published in "Journal of Healthcare Engineering." All articles are open access articles distributed under the Creative Commons Attribution License, which permits unrestricted use, distribution, and reproduction in any medium, provided the original work is properly cited.

Associate Editors

Xiao-Jun Chen , China
Feng-Huei Lin , Taiwan
Maria Lindén, Sweden

Academic Editors


Cherif Adnen, Tunisia
Saverio Affatato , Italy
Óscar Belmonte Fernández, Spain
Sweta Bhattacharya , India
Prabadevi Boopathy , India
Weiwei Cai, USA
Gin-Shin Chen , Taiwan
Hongwei Chen, USA
Daniel H.K. Chow, Hong Kong
Gianluca Ciardelli , Italy
Olawande Daramola, South Africa
Elena De Momi, Italy
Costantino Del Gaudio , Italy
Ayush Dogra , India
Luobing Dong, China
Daniel Espino , United Kingdom
Sadiq Fareed , China
Mostafa Fatemi, USA
Jesus Favela , Mexico
Jesus Fontecha , Spain
Agostino Forestiero , Italy
Jean-Luc Gennisson, France
Badicu Georgian , Romania
Mehdi Gheisari , China
Luca Giancardo , USA
Antonio Gloria , Italy
Kheng Lim Goh , Singapore
Carlos Gómez , Spain
Philippe Gorce, France
Vincenzo Guarino , Italy
Muhammet Gul, Turkey
Valentina Hartwig , Italy
David Hewson , United Kingdom
Yan Chai Hum, Malaysia
Ernesto Iadanza , Italy
Cosimo Ieracitano, Italy

Giovanni Improta , Italy
Norio Iriguchi , Japan
Mihajlo Jakovljevic , Japan
Rutvij Jhaveri, India
Yizhang Jiang , China
Zhongwei Jiang , Japan
Rajesh Kaluri , India
Venkatachalam Kandasamy , Czech Republic
Pushpendu Kar , India
Rashed Karim , United Kingdom
Pasi A. Karjalainen , Finland
John S. Katsanis, Greece
Smith Khare , United Kingdom
Terry K.K. Koo , USA
Srinivas Koppu, India
Jui-Yang Lai , Taiwan
Kuruva Lakshmanna , India
Xiang Li, USA
Lun-De Liao, Singapore
Qiu-Hua Lin , China
Aiping Liu , China
Zufu Lu , Australia
Basem M. ElHalawany , Egypt
Praveen Kumar Reddy Maddikunta , India
Ilias Maglogiannis, Greece
Saverio Maietta , Italy
M.Sabarimalai Manikandan, India
Mehran Moazen , United Kingdom
Senthilkumar Mohan, India
Sanjay Mohapatra, India
Rafael Morales , Spain
Mehrbakhsh Nilashi , Malaysia
Sharnil Pandya, India
Jialin Peng , China
Vincenzo Positano , Italy
Saeed Mian Qaisar , Saudi Arabia
Alessandro Ramalli , Italy
Alessandro Reali , Italy
Vito Ricotta, Italy
Jose Joaquin Rieta , Spain
Emanuele Rizzuto , Italy






Dinesh Rokaya, Thailand
Sébastien Roth, France
Simo Saarakkala , Finland
Mangal Sain , Republic of Korea
Nadeem Sarwar, Pakistan
Emiliano Schena , Italy
Prof. Asadullah Shaikh, Saudi Arabia
Jiann-Shing Shieh , Taiwan
Tiago H. Silva , Portugal
Sharan Srinivas , USA
Kathiravan Srinivasan , India
Neelakandan Subramani, India
Le Sun, China
Fabrizio Taffoni , Italy
Jinshan Tang, USA
Ioannis G. Tollis, Greece
Ikram Ud Din, Pakistan
Sathishkumar V E , Republic of Korea
Cesare F. Valenti , Italy
Qiang Wang, China
Uche Wejinya, USA
Yuxiang Wu , China
Ying Yang , United Kingdom
Elisabetta Zanetti , Italy
Haihong Zhang, Singapore
Ping Zhou , USA

Contents




Monitoring of Sleep Breathing States Based on Audio Sensor Utilizing Mel-Scale Features in Home Healthcare

Yu Fang , Dongbo Liu , Zhongwei Jiang , and Haibin Wang 
Research Article (13 pages), Article ID 6197564, Volume 2023 (2023)

A Review on the Applications of Time-Frequency Methods in ECG Analysis

Bikash K. Pradhan , Bala Chakravarty Neelappu , J. Sivaraman , Doman Kim , and Kunal Pal 
Review Article (34 pages), Article ID 3145483, Volume 2023 (2023)

A New Approach to Noninvasive-Prolonged Fatigue Identification Based on Surface EMG Time-Frequency and Wavelet Features

Fauzani N. Jamaluddin , Fatimah Ibrahim , and Siti A. Ahmad 
Research Article (15 pages), Article ID 1951165, Volume 2023 (2023)

Research Article

Monitoring of Sleep Breathing States Based on Audio Sensor Utilizing Mel-Scale Features in Home Healthcare

Yu Fang ^{1,2}, Dongbo Liu ^{1,2}, Zhongwei Jiang ², and Haibin Wang ¹

¹School of Electrical Engineering and Electronic Information, Xihua University, Chengdu 610000, China

²Graduate School of Science and Technology for Innovation, Yamaguchi University, Ube 755-0096, Japan

Correspondence should be addressed to Dongbo Liu; daniel_lb@126.com

Received 4 February 2022; Revised 3 July 2022; Accepted 24 November 2022; Published 9 February 2023

Academic Editor: Kunal Pal

Copyright © 2023 Yu Fang et al. This is an open access article distributed under the Creative Commons Attribution License, which permits unrestricted use, distribution, and reproduction in any medium, provided the original work is properly cited.

Sleep-related breathing disorders (SBDs) will lead to poor sleep quality and increase the risk of cardiovascular and cerebrovascular diseases which may cause death in serious cases. This paper aims to detect breathing states related to SBDs by breathing sound signals. A moment waveform analysis is applied to locate and segment the breathing cycles. As the core of our study, a set of useful features of breathing signal is proposed based on Mel frequency cepstrum analysis. Finally, the normal and abnormal sleep breathing states can be distinguished by the extracted Mel-scale indexes. Young healthy testers and patients who suffered from obstructive sleep apnea are tested utilizing the proposed method. The average accuracy for detecting abnormal breathing states can reach 93.1%. It will be helpful to prevent SBDs and improve the sleep quality of home healthcare.

1. Introduction

Healthcare-related issues have become the hot spots of society around the world. Among them, sleep quality plays an important role in health management. Poor sleep quality caused by sleep-related breathing disorders will impact peoples' daily life seriously. SBDs mainly include obstructive sleep apnea (OSA), central sleep apnea (CSA), and the mixed type. OSA which means the obstruction of the upper airway primarily due to the flabby tongue and uvula, is the most common SBD, CSA would cause sleep breathing apnea by the problem of the brain, and another type is the case mixed with the OSA and CSA [1]. The breathing abnormalities of SBDs are apnea, hypopnea, and snore. An apnea event lasts more than 10 seconds, and it can lead to a lower oxygen supply to the brain [2]. The ventilation of hypopnea will reduce to less than 50% of normal ventilation, and it will cause the value of oxygen levels to decline by more than 4% compared with the median. Snore is generated by a partial obstruction of the upper airway and is recognized as a vital sign of SBDs prevention [3]. The most harmful thing about these abnormal breathing states is the reduction of the oxygen supplement to the heart and brain. SBDs will lead to

the complications of cardiovascular diseases and increase the risk of diabetes, cerebral stroke, and Alzheimer's disease [4, 5].

SBDs are not exclusive to the older as we thought, they will occur for different age groups and the morbidity is increasing in recent twenty years [6]. There is much evidence of the general population lacking awareness of SBDs, more than 20% of adults are suffering from SBDs with different levels, yet less than 25% of SBDs sufferers realized that they have been disturbed by the bad sleep health condition [1]. And the high cost of the existing clinical means keeps people from getting tests and treatment.

In the clinic, polysomnography (PSG) is the golden standard and the only way to provide the Apnea-Hypopnea Index (AHI) exactly for diagnosing SBDs. However, dozens of sensors used for PSG are not only costly but also complicated for common patients [7]. Hence, a smart and portable monitoring measure with the least sensors is imperative for home healthcare of SBDs.

The smart wearable with sensors is a new trend in the smart monitoring system of long-life diseases [8, 9], especially for the increasing demand for home healthcare. Researchers have applied different kinds of sensors, such as

light sensors [10] and inertial sensors, to monitor the sleep condition by respiratory rate and breathing pattern analysis [11]. Researchers used the ultrasonic radar to normal and abnormal breathing activity [12] and used a thermal imaging camera to diagnose breathing disorders [13]. Researchers also used the sound sensors set near the nose and mouth to record the breathing sound signal for detecting apnea and hypopnea events by a set of pattern recognition rules [14]. Some researchers recorded tracheal signals from the throat to acquire the respiratory rate or set the sound sensor to the skin in a suprasternal notch to evaluate the breathing pattern in the high-frequency range [15, 16]. In previous studies, the sound sensors with smaller contact areas and easier operation are applied to record the breathing sound signal for sleep breathing monitoring [17]. As described above, these abnormal breathing states of SBDs will lead to decreasing ventilation while inspiration and expiration. The changes of ventilation can be reflected by different breathing states, such as snoring, apnea, hypopnea, and irregular breathing rate. Based on the production mechanism and physical significance of the abnormal breathing states, it is potential to detect the abnormality and health situation of sleep by breathing sound signals via a smart system with sound sensors.

In the research area of sleep monitoring based on breathing sound signals, many researchers focused on the respiratory rate detection based on the genetic algorithm [18], Hilbert transform [19], and neuro-fuzzy method [20] to analyze SBDs. In our previous study [21], a moment waveform analysis was proposed to segment the breathing cycles for respiratory rate detection. And snoring detection has been discussed to evaluate the level of SBDs [22]. And some researchers used the respiratory phase analysis to detect apnea [23]. Xie et al. proposed a deep learning method with a 2D spectrogram to detect snoring in various sleeping positions, based on constant Q transformation [24]. Shen et al. used CNN and LSTM to identify the snoring of OSAHS patients based on MFCC, LPCC, and LPMFCC and extracted the AHI index to evaluate the severity of OSAHS [25].

It can be found that the segmentation of breathing sound and the detection of breathing states are crucial for sleep monitoring and SBDs diagnosis. However, there are two problems. One problem is how to reduce the computational complexity of the analysis algorithms for the long-time data, that is, the real-time capability. Another one is how to guarantee the accuracy of the detection results. Most of the existed research always focused on a short period of the breathing signal, and the accuracy of the analysis results is not sufficient for healthcare. Our research aims to detect abnormal breathing states related to the SBDs such as apnea, hypopnea, and irregular breathing in a simple and fast way by a portable system.

This study keeps the ventilation of oxygen and carbon dioxide while sleep in mind and proposes a method to detect sleep breathing states based on Mel frequency cepstrum analysis by a portable acquisition system of breathing sound signal. In Section 2, the acquisition of breathing sound signal

utilizing the sound sensor is introduced. The test condition and testers are also referred briefly. Then, the segmentation of breathing cycles is sketched in Section 3 as the pre-processing for the further analysis. Section 4 describes the proposed detection method based on Mel frequency cepstrum analysis in detail, including the feature extraction and the identified rules of different sleep breathing states. Experiments and results can be found in Section 5. Finally, the discussion and conclusion are summarized in Sections 6 and 7, respectively.

2. Wearable Acquisition System with Sound Sensor

A wireless sound sensor and a commercial headset (Plantronics, M165) were applied to record sleep breathing data during the whole night. The M165 is very light and easily-operated. It is indeed a cheap and easy use for smart sleep healthcare in daily life. The acquired breathing data will be transmitted to a smartphone by Bluetooth and stored in mp3 format which is convenient for computerized analysis. The parameters of audio files can be set by an APP developed by our team. In this study, the sampling frequency is 44.1 kHz. The environment of data acquisition is shown in Figure 1. The headset is fixed to the nose by a strip of cosmetic tape. As we mainly focus on the changes in breathing airflow, the breathing sound signal from the nose and mouth can be recorded as long as the headset does not fall off and the tester is almost unaffected while sleeping whether at home or not.

At the beginning of preprocessing, the original sample frequency will be down-sampled to 11.025 kHz to reduce the computation amount. The real sleep breathing sound signal recorded by our system is shown in Figure 2. Figure 2(a) is one-night sleep breathing sound data. The recording lasts about 5 hours, and the intensity of breathing changes greatly. Figure 2(b) is a part of stable normal breathing sound data from the fifth hour and Figure 2(c) is a part of complex breathing sound data from the third hour. There are some obvious breathing pauses shown in Figure 2(c), and they are related to the obstruction of the airway. Hence, there is a high potential to identify different abnormal breathing states, such as apnea, hypopnea, unstable respiratory rate, and snore, from the breathing sound signal acquired via a portable and wireless sensor. Eight volunteers are selected as testers, including four in twenties, two in thirties, and two in Fifties. The study was approved by the ethics committee of Chengdu Region General Hospital (No. 2015 research 01). All testers' consent was obtained before participating in the study. The twenties and thirties were tested by Epworth sleepiness score (ESS), the scores were all less than 9, which was normal. The elder testers are diagnosed with moderate OSA and severe OSA by PSG with AHI = 16 and 32, respectively. All the testers have monitored for the whole night lasting more than five hours. The breathing cycles of one-night data are counted, and the breathing states are manually labeled under the guidance of a professional physician for further analysis.

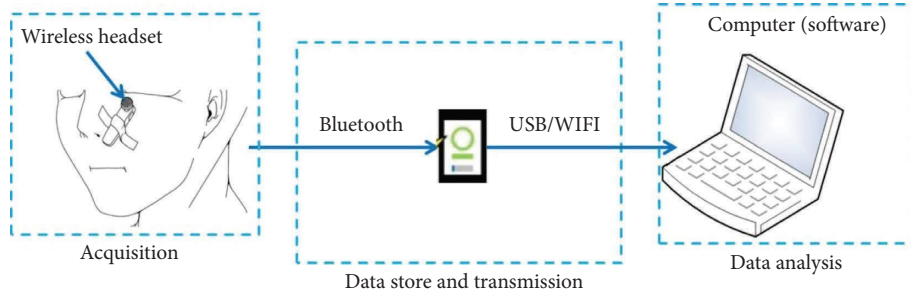


FIGURE 1: The wearable acquisition system via a wireless sensor.

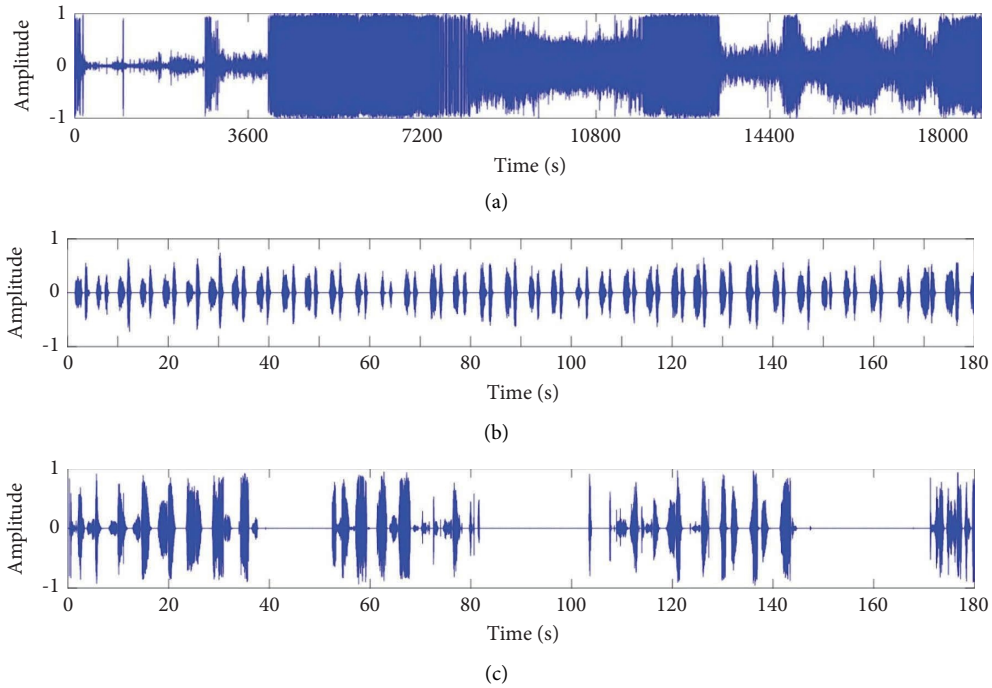


FIGURE 2: The original waveforms acquired by the portable system. (a) The sleep breathing sound signal of one-night test; (b) the part of normal breathing signal from recording 2(a); and (c) the part of abnormal breathing signal from recording 2(a).

3. Segmentation of Sleep Breathing Signal Based on Characteristic Moment Waveform Analysis

To identify the breathing state accurately, the breathing cycle should be segmented for further analysis. A brief introduction of the segmentation method is presented in this section. The details can be found in our previous work [21].

The enhanced processing for amplitude contrast diminution has been performed first to reduce the effect of the weak breathing issues during the whole night's sleep.

The precondition assumes the noise part of the sleep breathing sound signal as a signal with zero-mean and unit variance. Suppose the sleep breathing sound signal is $r(t)$, the random noise signal is $n(t)$, and the real output signal is $y(t) = r(t) + n(t)$, time characteristic waveform (TCW) of sleep breathing sound signal, denoted by $c(t, \delta)$, defined as the variance of the output $y(t)$ can be given by the following equations:

$$c(t, \delta) = \int_{t-\delta}^{t+\delta} (y(\tau) - \bar{y}(t))^2 d\tau = \int_{t-\delta}^{t+\delta} y(\tau)^2 d\tau - 2\delta\bar{y}(t)^2, \quad (1)$$

$$\bar{y}(t) = \frac{1}{2\delta} \int_{t-\delta}^{t+\delta} y(\tau) d\tau. \quad (2)$$

Then, the characteristic moment waveform (CMW) is calculated by the thought of image shape identification in image processing with another time scale l , which is represented by $I(t, \delta, l)$. It is calculated according to the following equation:

$$I(t, \delta, l) = \int_{t-l}^{t+l} (\tau - t)^2 c(\tau, \delta) d\tau. \quad (3)$$

For a discrete signal with length N , the computations of TCW and CMW only need $8N$ and $15N$ additions and multiplications, respectively. The algorithm can process the whole night data fast, and it will be helpful for real-time monitoring.

According to our experimental statistic, the scale l is usually set to (1.5, 3), about half of the sleep breathing cycle. The time scale δ is set as 0.1, about 1/10 of the phase duration. After choosing the suitable time scales, TCW and CMW can be extracted by equations (1) to (3). C_{\min} of CMW is the local minimum point sequence which would be calculated first. Then, the local maximum points sequence T_{\max} of TCW can be found by a computation window with C_{\min} as the central points. The local maximum point sequence of CMW can be obtained as the cycle segmentation points and adjusted according to T_{\max} . Finally, the incorrectly segmented breathing pauses will be combined utilizing a threshold value by the average amplitude of the test data.

The breathing cycle segmentation result of partial normal breathing signal is shown in Figure 3.

4. Detection of Breathing States via Mel Frequency Cepstrum Analysis

During the whole night's sleep, the sleep breathing state changes greatly. Besides the apnea, there are the hypopnea events, snore events, and others as shown in Figure 4. In Figure 4, two types of irregular breathing events are found and shown by blue and orange boxes. They are all related to the obstruction of the upper airway. The breathing parts marked by blue boxes display the changed respiratory rate. By hearing, they mix with noise caused by the movements of the nose and mouth. It is easy to find that the breathing parts of orange boxes have higher amplitude with the extended or merged inspiration/expiration. And they sound similar to labored breathing and can be classified as a kind of snore.

Differing from the apnea with a clear definition in the time domain, other complex breathing states cannot be detected in the time domain. According to the previous research, the distribution of frequency energy would be very different between the normal and abnormal breathing states. From the time-frequency representation, the breathing case with apnea has much more energies below 500 Hz and above 3500 Hz compared with the normal case. It provides a probable way to distinguish the different breathing states in the frequency domain.

4.1. The Conventional MFCCs Analysis. Psychophysical studies have shown that human perception of the frequency content of sounds does not follow a linear scale. The Mel frequency cepstrum coefficients (MFCCs) were proposed as it is very similar to perceptual linear predictive analysis of sound [26]. MFCCs were derived from the short time spectrum of a signal and were widely used both for speech and speaker recognition [27, 28]. MFCCs have already been applied to extract features of respiratory sound in combination with learning machines to recognize the wheeze for respiratory disorders [29, 30].

First of all, framing and windowing are applied for the conventional MFCC algorithm. Then, fast Fourier transform (FFT) is used to transform the signal of each frame from the time domain to the frequency domain. Then, the energy

spectrum is calculated. Next, the energy signal is filtered by the Mel-scale filter bank and processed in the logarithm orderly. At last, discrete cosine transform would transform the signal into the time domain and extract a series of coefficients.

As the core of MFCCs, the relationship between Mel frequency and real frequency is defined as follows:

$$\text{Mel}(f) = \frac{1000 * \lg(1 + (f/700))}{\lg(1 + (1000/700))}, \quad (4)$$

where f is the real frequency and $\text{Mel}(f)$ is the Mel-scale frequency. As the human perception of the frequency content is almost linear below 1 kHz and nonlinear over 1 kHz, 1000 is a key parameter to determine the relationship of f and $\text{Mel}(f)$ simulating the character of the human ear. 700 is the parameter that affects the relationship's changing trend between f and $\text{Mel}(f)$.

For the frequencies under 1000 Hz, the Mel scale can be approximated to a linear scale. Mel frequency can represent the details of the low-frequency range more accurately than the high-frequency range. Hence, it can capture formants that lie in the low-frequency range.

The Mel filter bank is designed based on Mel-scale frequency. The Mel-scale frequency distributes uniformly-spaced in Mel scale, simulating the critical frequency bands of the human ear. The center of each triangle window is the starting of the next one.

The logarithm is used to compress the components above 1000 Hz. And it can translate the multiplicative components into the additive ones and reduce the computation complexity [26]. A logarithm can provide the frequency energy distribution of a one-time point in the form of addition. Finally, the Mel frequency cepstrum coefficients will be extracted by discrete cosine transform.

Our purpose is to find the relationship between the frequency energy distribution and the monitoring time. The results of the processing after the logarithm should be paid attention to in this study.

4.2. Analysis of Breathing Sound Signal Based on Mel Frequency Cepstrum Analysis. Here, we proposed a method of parameters extraction to detect different breathing states, and the flowchart is displayed in Figure 5.

As shown in Figure 5, window screening is the first step and the length of the rectangle window is set as 1024 sample points, about 100 ms according to the sampling frequency. The window moves forward by overlapping the half of itself to keep enough details of the observation. Then, the frequency energy distribution of the breathing sound signal would be calculated by power spectrum density (PSD) in the second step. The PSD estimation is an important part of modern signal processing and reflects the energy distribution of the frequency component of the signal. The autoregressive (AR) method is the most frequently used parametric method because the estimation of AR parameters can be performed easily by solving the linear question. Here, Yule-Walker's method is used to make the power spectrum density instead of the energy of the FFT result. The order of

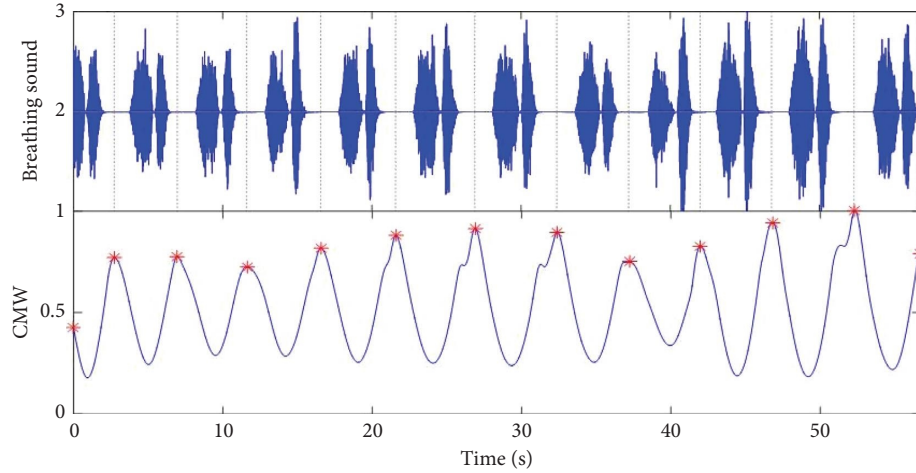


FIGURE 3: Segmentation result by CMW.

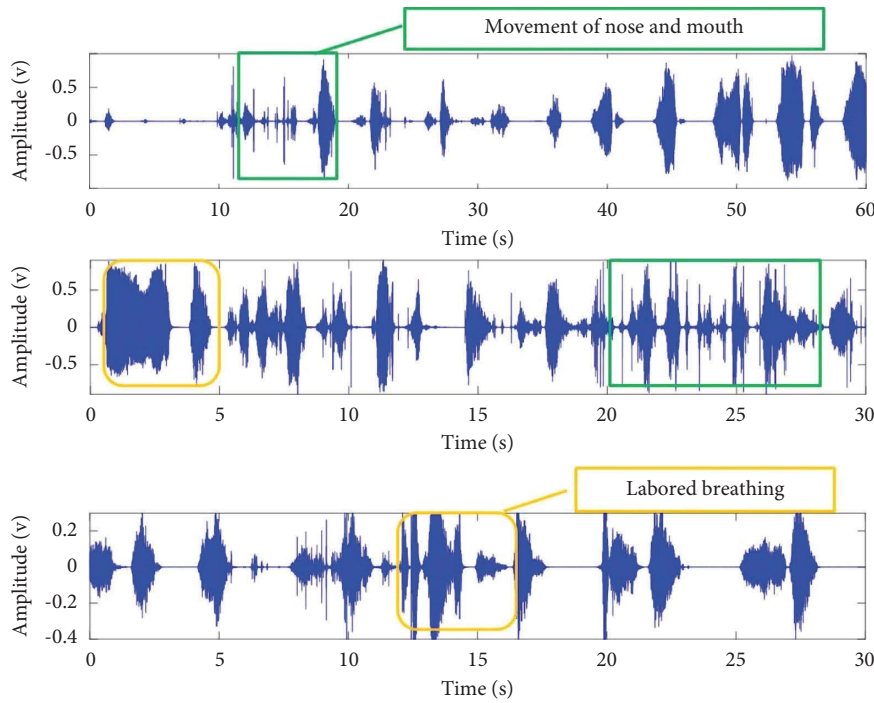


FIGURE 4: Three parts of abnormal sleep breathing sound data.

an autoregressive prediction model for the signal is set as 32 [31].

In the third step, the energy of the signal is filtered by the Mel frequency filter banks including 20 triangle filters. The triangle filter bank is selected by default in speech processing shown in Figure 6, which simulates the auditory characteristics of the human ear. The mathematical expression of the triangular window is simple, reducing the amount of computation.

And the 20-dimension Mel-scale features are extracted after the logarithm operation in the fourth step. The horizontal of the feature matrix represents frames of observation time. The vertical of the matrix represents the Mel-scale filters of the filter bank.

To stand out the frequency energy distribution of each frame, a new feature set has been proposed in the fifth step, the core of our proposed method. The procedure of the proposed method to extract the effective features is described in detail. The sketch map of extraction for one breathing cycle can be found in Figure 7 to illustrate the algorithm.

- (a) Extract the Mel-scale features of one segmented breathing cycle according to the first four steps of the flowchart in Figure 5.

The Mel-scale features $f_{i,j}$ can be displayed by the stretch map shown in Figure 7(b). i is the label of the triangle filters of the Mel frequency filter bank in the frequency domain, from 1 to 20. j is the number of

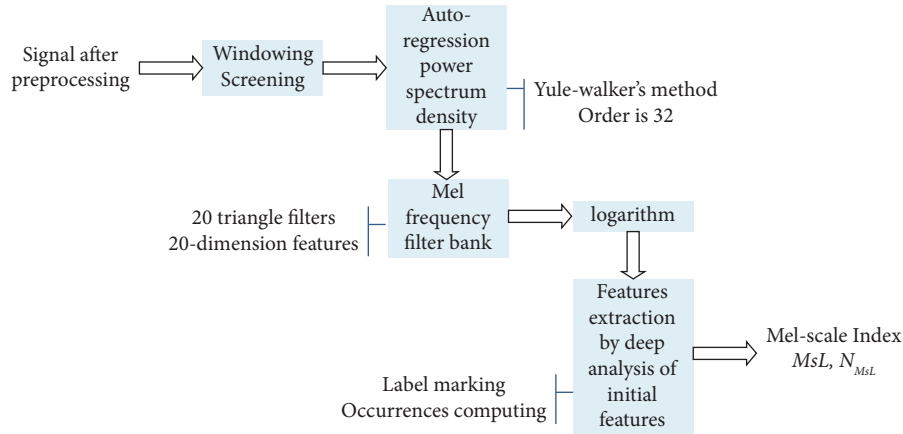


FIGURE 5: The flowchart of the modified Mel frequency cepstrum analysis.

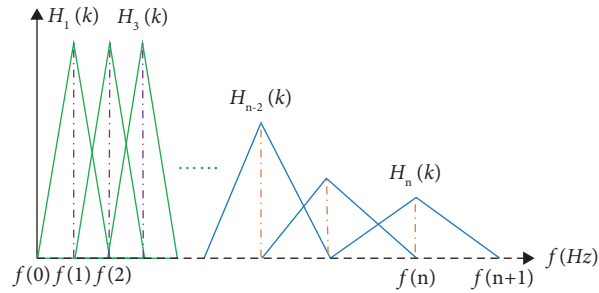


FIGURE 6: Schematic diagram of the triangular filterbank.

frames in the time domain, from 1 to N . N is the total number of frames of each breathing cycle.

- (b) Find the maximum point of each column of $f_{i,j}$, denoted by $A_{i,j}$.

i is corresponding to the label of the Mel-scale filter and represents a fixed Mel-scale frequency range. We proposed it as Mel-scale label (MsL) as shown in Figure 7(c). The X -axis is the frame number, and Y -axis is the MsL. MsL can be explained by the main part of frequency energy distributing in one observed duration in the time domain.

- (c) Compute the present times of each MsL to represent the distribution of frequency energy in each cycle, marked as N_{MsL} which is shown in the bar chart of Figure 7(d). MsL and N_{MsL} are proposed to detect the abnormal breathing sound signal. For the normal breathing cycle shown in Figure 7(a), it is found that the label number i of MsL is from 4 to 14 in the duration of inspiration and expiration compared with the breathing stopping intervals as shown in Figure 7(c). So, the frequency energy of this breathing cycle is mainly filtered by the No. 4 to No. 14 Mel-scale filter as same as the results of N_{MsL} shown in Figure 7(d).

After all the five steps, we can use MsL and N_{MsL} to analyze the components of the breathing sound signal and to detect the abnormal breathing states finally. The results of

detecting abnormal breathing states will be demonstrated in the next section.

5. Experiment

5.1. Analysis of Breathing Sound Signal by the Proposed Identification Method. The label of Mel-scale features, MsL, and the corresponding N_{MsL} in each segmented breathing cycle during one-night monitoring can be extracted. The energy of distribution in a fixed frequency range is useful to present the features of different breathing states. We mainly separate snoring, normal breathing, and abnormal breathing components of the breathing signal.

It is found that the MsL in the low-frequency range can represent the snore component. The normal breathing component is usually represented by MsL in the middle-frequency range. The abnormal breathing components including apnea, hypopnea, and irregular breathing rate can be expressed by MsL in the high-frequency range. Checking results manually by ear and eye is the reference under the guidance of a professional doctor.

So, three MsL sets are proposed, i.e., low-frequency label set, middle-frequency label set, and high-frequency label set and marked as FL, FM, and FH, respectively, in Figure 8.

For different individuals, there would be a little difference when we partition these three MsL sets. Based on the experimental attempts, the common part of each MsL set is selected for the further analysis, that is, MsL_2 for the snore detection, MsL_4 to MsL_7 for the normal breathing state

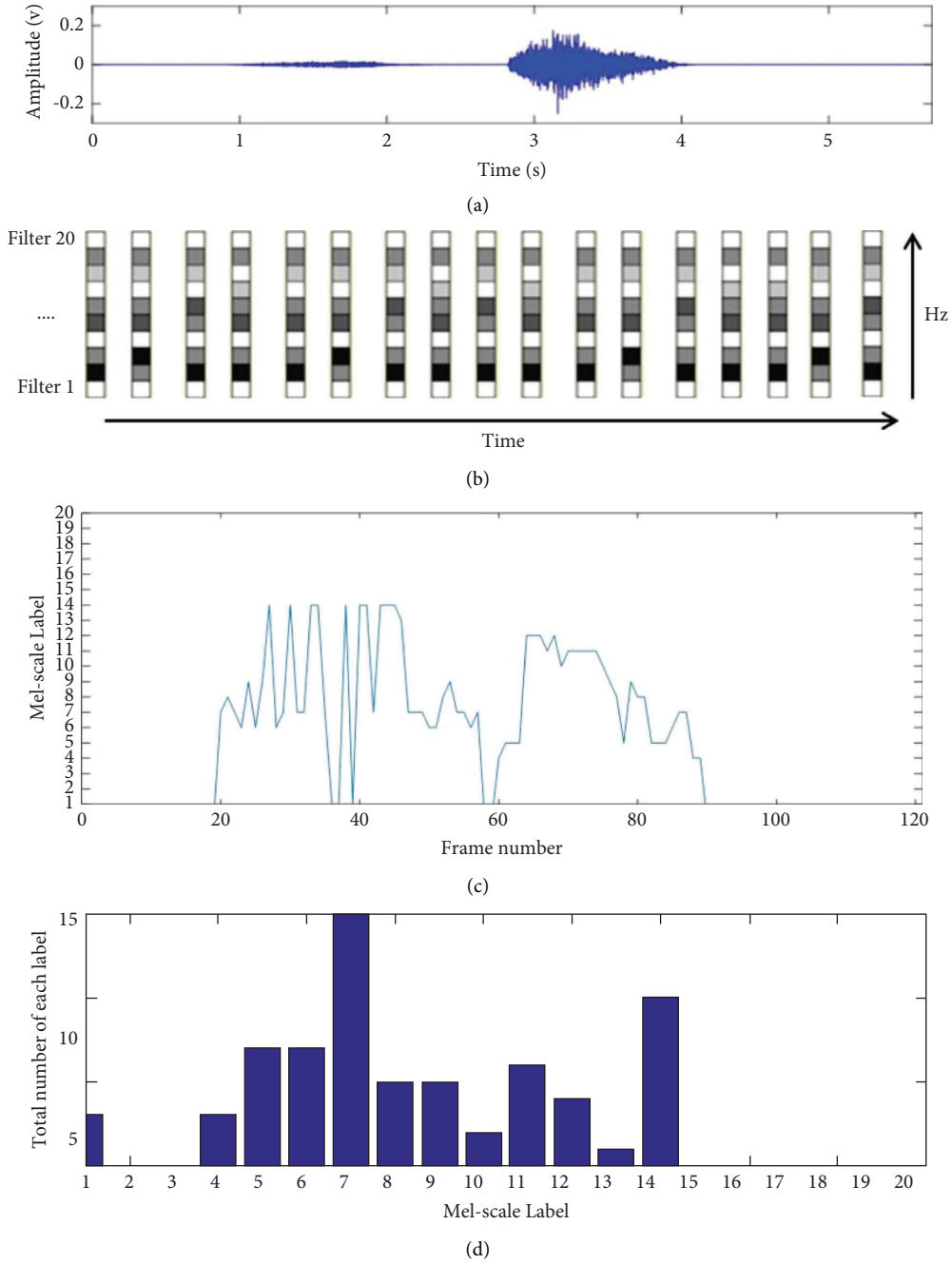


FIGURE 7: Extraction of Mel-scale indexes for a breathing cycle. (a) The waveform of a breathing cycle; (b) the sketch map of Mel-scale features; (c) the 1st index, MsL; and (d) the 2nd index, N_{MsL} .

detection, and MsL₁₅ to MsL₁₇ for the abnormal breathing state detection. To detect different breathing components in each breathing cycle, threshold values are applied and displayed by red lines in Figure 8. As the time duration of inspiration and expiration lasts about 2.5 seconds in one breathing cycle according to our experimental dataset, the total N_{MsL} equals the total number of frames, about 50 times. Hence, according to the experiment results and observation, the threshold values for FM and FH are set by 40% of the total N_{MsL} of each MsL, about 20 times. And the threshold value of FL is set by 20% of the total number C_{L_i} of each MsL, about 10 times.

If N_{MsL} is larger than the red threshold line, the corresponding cycle can be symbolized by 1, the opposite is 0. It is obvious that the breathing cycles with abnormal component always accompany the snoring component. The abnormal component and normal component do not exist at the same time in the usual case from Figure 8. So, it is the potential to detect different kinds of breathing states based on these three MsL sets.

If there is '1' of FH, the breathing state can be detected as abnormal. If there is '0' of FH, combined with the detection results of FM, heavy breathing can be identified from the normal states which can be checked by the ear.

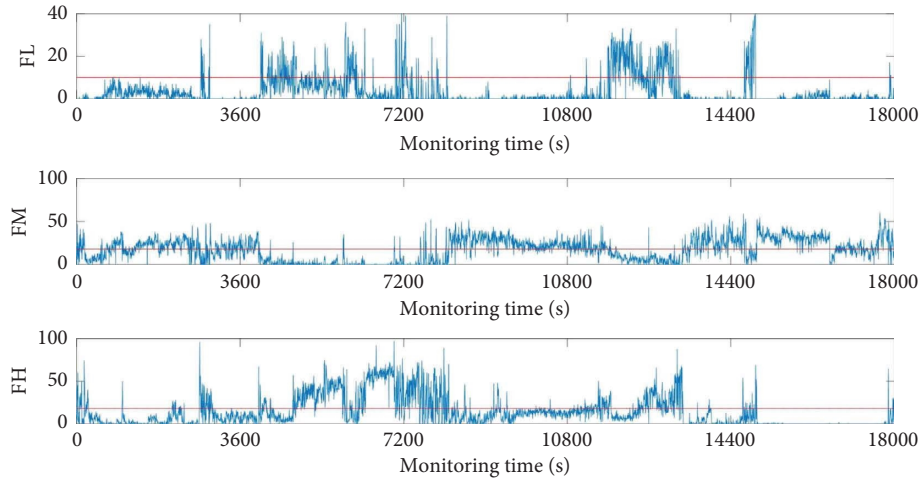


FIGURE 8: N_{MsL} of FL, FM, and FH is used to detect breathing components.

The snore can be divided into the normal type and the abnormal type. Normal snore is related to simple snoring, and abnormal snore is related to SBDs. However, they all should be concerned. So, the snore is detected separately from other abnormal breathing states and listed for a useful index. If there is '1' in FL, the breathing cycle is identified as breathing with snore.

The study focuses on the ratio of abnormal breathing states during the monitoring for sleep healthcare management in the early stage. Obviously, the subclassifying of breathing types is a rough judgment now and it will be applied to a deeper discussion of accurate analysis for SBDs in the future work.

5.2. Application for the Sleep Breathing States Detection.

The identified results by MsL sets for an OSA tester (AHI = 16) are shown in Figure 9. Figure 9(a) displays the detection results of normal/abnormal sleep state. The abnormal sleep breathing cycle is denoted by '1' and the normal sleep breathing is '0' based on the identification rules introduced in the last subsection. It is easy to compute the time duration of normal and abnormal breathing state lasting during the whole night. In this case, the normal breathing lasts 2.8 hours, and the abnormal breathing lasts 2.2 hours. Figure 9(b) displays the detection result of snoring. The breathing cycle with snore is marked as '1,' and the snore lasts 1.8 hours of the whole night totally.

The time duration of breathing stop from the audio waveforms can distinguish the apnea and typical hypopnea from normal breathing states. For apnea, the breathing stop is larger than 10 s. As the ventilation of hypopnea will reduce to less than 50% of the normal ventilation, the breathing stop of the typical hypopnea is calculated from 6 s to 10 s according to the clinical definition of apnea and hypopnea [2]. Irregular breathing rate can be picked up by comparing with the normal parts.

From the original breathing waveforms of A1 to A3 shown in Figure 10, two parts of the breathing signal in each

section are shown orderly. It can be found that there is obvious apnea (such as A1-1, A3-1, and A3-2), hypopnea (such as A1-2), irregular breathing (such as A1-1, A2-1, and A2-2), and breathing with noise caused by the body movement (such as A2-1) from the waveforms in time domain clearly. Sections A1 to A3 belong to the abnormal breathing states with snore.

From the original breathing waveforms of N1 and N2 shown in Figure 11, these two sections are normal stable breathing, and breathing of N2 is snoring. The red line in Figure 10 is the envelope of the spectrum, and it is easy to find that there is a large energy in the middle-frequency range (500–1500 Hz), representing the normal breathing component for both N1 and N2. The amplitude of N2 is higher than N1. And the higher ratio of frequency energy distributes below 500 Hz is the main feature of snore shown in section N2.

Applying the proposed method based on Mel-scale features, the monitoring results of all the testers are listed in Table 1. We can find the total time of the whole night monitoring and the time durations of different breathing states. To evaluate the sleep quality, the ratio of the normal breathing during the night is computed by the following equation:

$$R_{\text{Sleep}} = \frac{T_{\text{Normal}}}{T_{\text{Monitoring}}}, \quad (5)$$

where R_{Sleep} is used to test the quality of sleep by the detection of normal breathing state, T_{Normal} is the total time duration of normal breathing state lasting, and $T_{\text{Monitoring}}$ is the total time duration of the sleep monitoring. It will be a meaningful index to know and manage sleep health in one's daily life.

According to the detected results of breathing states, the ratio of normal breathing states is over 70% for testers no. 1, 2, 3, and 5 which is higher than the OSA testers no. 7 and 8, which were diagnosed by PSG. Testers No. 4 and 6 have lower ratios of normal breathing state and there are indeed a lot of apnea and hypopnea events during the monitoring

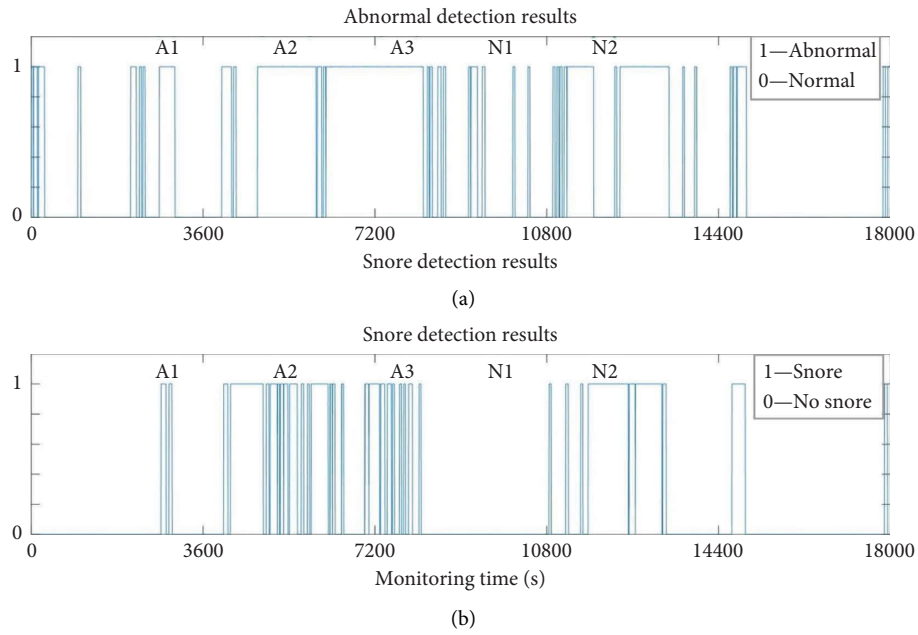


FIGURE 9: Monitoring results by MsL sets for an OSA tester. (a) Detection of normal and abnormal breathing states. (b) Detection of snoring state.

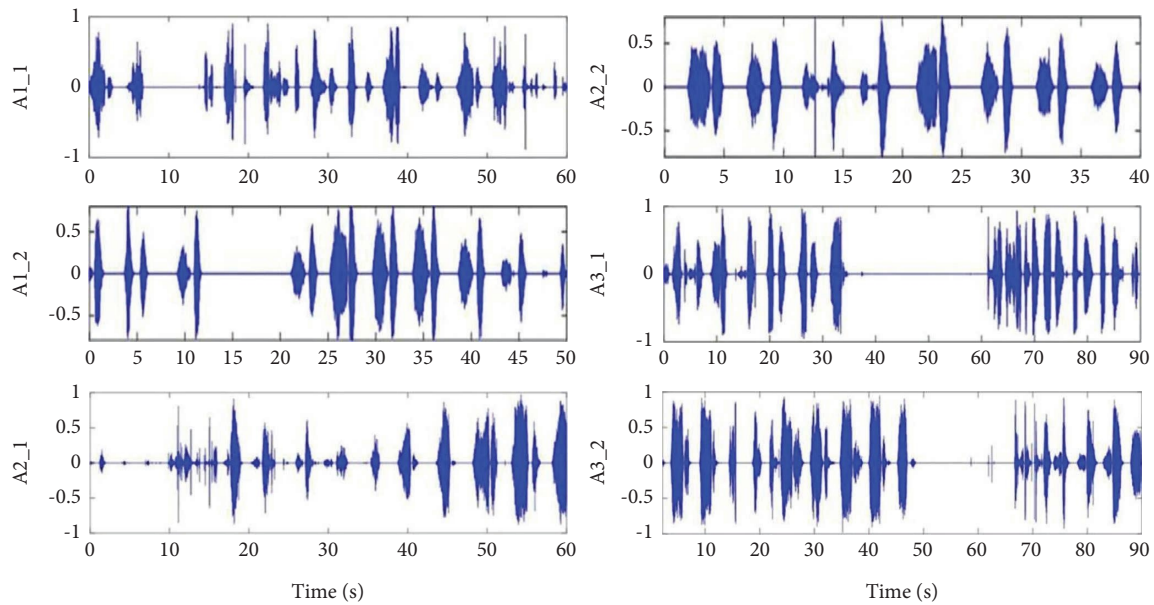


FIGURE 10: Validation of the abnormal breathing state detection by the proposed method.

procedure by checking up on the original breathing signal. Testers no. 4 and 6 were diagnosed as severe rhinitis by the doctor during the experimental period. Actually, after the relief from rhinitis symptoms, the results of monitoring are within the normal range. The extreme cases of young testers can also show the efficiency of the proposed method.

Moreover, it is found that the testers with a low ratio of normal breathing state always snore with a longer time

duration. Hence, snore is really an important sign related to the analysis and prevention of sleep breathing-related disorders.

The accuracy of detecting normal and abnormal breathing states can be given based on the prepared manual labels in our experiment, and the accuracy of our proposed method of the testers can reach 95.2% shown in Table 1, and the average value is 93.1%.

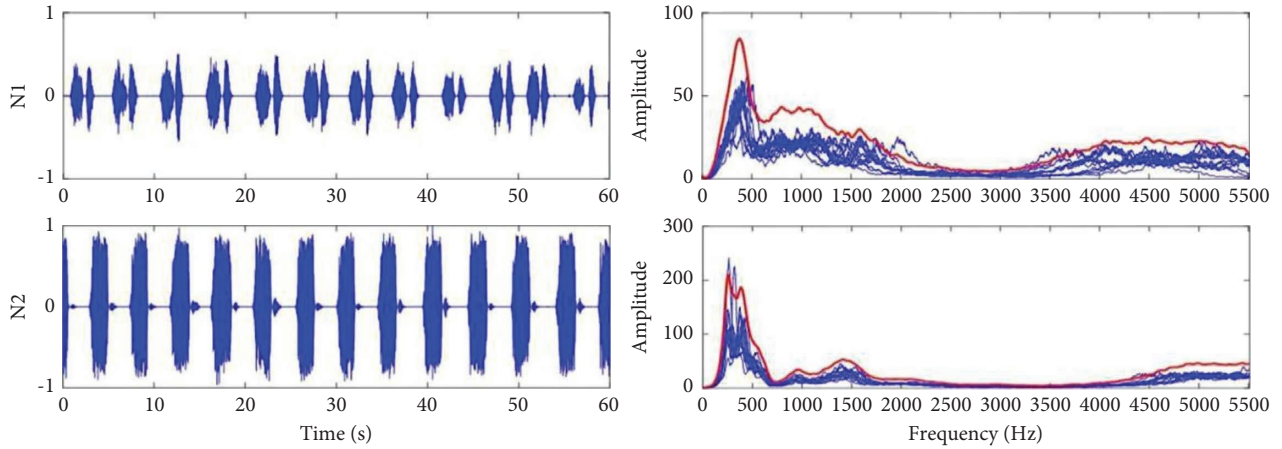


FIGURE 11: Validation of the normal breathing state detection by the proposed method.

TABLE 1: Detection results of sleep breathing states of testes.

Tester no	Years	Time (hour)	Normal (hour)	Abnormal (hour)	Snoring (hour)	Accuracy of S/N (%)	Normal ratio (%)	Accuracy of A/N (%)
1	20	7.7	6	1.7	0.5	93.5	77.9	93.2
2	21	7.5	5.6	1.9	0.3	96.0	74.7	94.4
3	21	6.8	4.9	1.9	0.1	98.5	72.1	91.9
4	20	6	2.4	3.6	2.2	96.4	40	90.2
5	31	7.5	5.5	2	1	90.8	73.3	94.9
6	34	8	4.2	3.8	3.2	97.6	52.5	92.2
7	58	5	2.8	2.2	1.8	97.5	56	95.2
8	60	6.8	2.3	4.5	3.8	98.2	33.8	92.7

6. Discussion

In the studies of breath state detection by breath sound signal, some researchers used the measurement of energy to detect apnea events during the breath and breath hold [23]. From [24] in Table 2, it can be seen that the MFCC feature parameters are the most effective in classifying snores among the three features used. Using MFCC combined with the LSTM method can achieve 87% accuracy. At the same time, the AHI index was also estimated. Although there is a particular gap with the AHI value detected by PSG, it can be used as an auxiliary reference in the classification of OSAHS. It can also be found that the average accuracy of snoring recognition of OSA patients and normal people is 95.3% by combining deep learning and two-dimensional spectral features in [25]. Literature [23] used spectral energy and VAD criterion threshold for apnea detection for simulated apnea signals and achieved an accuracy of 97%. Still, it is not applied to the actual breathing signals of OSA patients, nor does it mention hypopnea detection.

The method in this paper does not use classical machine learning and deep learning methods, so the amount of calculation is small. Moreover, the threshold displays the fact between the characteristic parameters and the breathing signal. At the same time, the normal and abnormal breathing and snoring sounds are distinguished. The accuracy rate of 93.1% can be achieved by judging normal and abnormal

breathing. The judgment of abnormal breathing includes apnea, hypopnea, and other respiratory disturbance events. However, due to the small amount of breathing data and individual differences among testers, there is a state of misjudging normal breathing as snoring in snoring detection. It is necessary to refine the types of abnormal breathing and accurately find them for the intervention in continuous work.

Some researchers combined a sound sensor, accelerometer, and pulse oximeter to get AHI index for SBDs [16]. Moreover, the degree of blood oxygen saturation (SpO₂) acquired by the pulse oximeter is a vital index for the respiratory system in the clinic. The SpO₂ will decrease when there is an obstruction in the upper airway; that is, apnea, hypopnea, and irregular breathing will accompany the lower value of SpO₂.

Hence, SpO₂ has been monitored for the testers as well and the abnormal breathing states can be evaluated by subtracting a fixed value from the medium value of SpO₂. In our experiment, it is easy to find that the results of SpO₂ are included in the scope of the proposed detection. The comparison results with SpO₂ are given in Figure 12. The red line represents the median value of the tester's SpO₂. It can be seen that the period when SpO₂ has a significant decrease compared to the median value is detected as an abnormal breathing state which matches the detection results.

TABLE 2: Summary of previous studies on breathing states detection by acoustic signal.

Authors	Method	Features	Dataset	Snore detection results	Abnormal detection results
[23]	Voice activity detection algorithm	FFT	50 normal people breath 20 cycles and hold their breath to make the apnea	Not mentioned	Apnea detection accuracy more than 97%
[24]	CNN + RNN	CQT spectrogram	Part of full night recordings from 38 subjects	Accuracy: 95.3%	Not mentioned
[25]	CNN + LSTM	MFCC, LPCC and LPMFCC	Whole night recoding from 32 volunteers	Accuracy: 87%	Calculate AHI values
This study	Threshold values for individuals	Mel-scale-based features	Full nights recoding from 8 testers	Accuracy: 96.1%	Accuracy: 93.1%

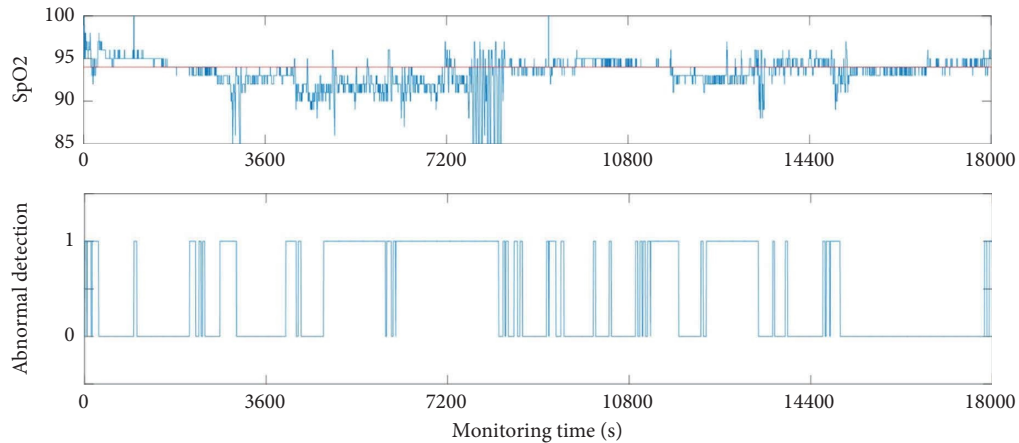


FIGURE 12: Comparison detection results with SpO2.

However, the abnormalities caused by the light obstruction of the airway can be pointed out by the proposed detection, which is not clearly defined. It may be related to the threshold values set by our proposed detection. More types of abnormal breathing states will be discussed deeply in future work. And because the tapes may become loose and the microphone's location may change occasionally, the acquisition system should be developed. And the classification and identification of breathing states are further refined. The analysis of the hypopnea state is limited by the small amount of experimental data and cannot be further refined and analyzed.

In other words, the tester dataset should be enlarged and the types of abnormal breathing states should be discussed in detail. We will optimize the ranges of MsL sets to analyze the components of breathing sound signal, such as dividing different frequency ranges to show more precise results. The relationship between our definitions of abnormal breathing and the pathological characteristics of SBDs will be discussed deeply in further study.

7. Conclusion

In this study, the sound sensor and microphone in a headset with Bluetooth were utilized to record and transmit the breathing sound signal during the whole night. The portable and wireless acquisition system proposed in this paper has less impact on sleep quality and can be operated simply anywhere. And the MFCCs are introduced from speech signal processing to the processing of breathing signal for sleep monitoring in-home healthcare. The MsL representing the main distribution of frequency energy in each frame is proposed to detect the different sleep breathing states. In addition, the data acquisition operation is simple, the cost of detection is low, and the accuracy can satisfy individual monitoring needs. Recognition of respiratory status and detection of abnormal breathing can be popularized in daily monitoring. It can also be used as an aid for clinical diagnosis based on a more detailed analysis of the results. The study is limited by the small amount of experimental data, so the classification and identification of breathing need to be

further improved, and the adaptability and accuracy of the algorithm need to be further enhanced. Although it has particular reference significance for the long-term sleep monitoring of individuals, the algorithm is still unstable in monitoring different people.

The core of the Mel frequency analysis is to reflect the relationship between the monitoring time and the frequency energy simulating the acoustic character of the human ear. For each frame in the time domain, the MsL is extracted by finding the maximum value of the frequency energy in each Mel scale. Then, the present times of each MsL are computed to show the frequency energy distribution of each segmented breathing cycle. Three MsL sets are determined corresponding to the normal breathing component, abnormal breathing component, and snore component, denoted by FM, FH, and FL. Finally, with the suitable threshold values and comprehensive evaluation rules, the normal breathing state, abnormal state, and snore state can be detected successfully. The types of sleep breathing states should be discussed deeply and classified accurately for examination and analysis of SBDs. And for different individuals, long-time monitoring and big data analysis are necessary to acquire more precise monitoring results for the prevention and treatment of SBDs in the future.

Data Availability

The data used to support the findings of this study are available from the corresponding author upon request.

Conflicts of Interest

The authors declare that they have no conflicts of interest.

Acknowledgments

This study was supported by the National Natural Science Foundation of China (Grant no. 61901393), the Ministry of Education "chunhui project" of China (Grant no. Z2018118), the National Natural Science Foundation of China (Grant no. 61571371), and the Talented Penson Projects of School (Grant nos. Z201087 and Z202088).

References

- [1] World Sleep Day, "Celebrate healthy sleep on world sleep day," in *Proceedings of the News Conference of World Sleep Day*, Beijing, China, March 2017.
- [2] J. A. Dempsey, S. C. Veasey, B. J. Morgan, and C. P. Donnell, "Pathophysiology of sleep apnea," *Physiological Reviews*, vol. 90, pp. 47–112, 2010.
- [3] U. R. Abeyratne, S. De Silva, C. Hukins, and B. Duce, "Obstructive sleep apnea screening by integrating snore feature classes," *Physiological Measurement*, vol. 34, no. 2, pp. 99–121, 2013.
- [4] C. Doukas, T. Petsatodis, C. Boukis, and I. Maglogiannis, "Automated sleep breath disorders detection utilizing patient sound analysis," *Biomedical Signal Processing and Control*, vol. 7, no. 3, pp. 256–264, 2012.
- [5] J.-Y. Huang, J.-R. Zhang, C.-J. Mao et al., "Effects of obstructive sleep apnoea hypopnoea and rapid eye movement sleep behavior disorder on cognitive impairment in Parkinson's disease," *Journal of Clinical Neurology*, vol. 29, no. 6, pp. 417–420, 2016.
- [6] China Daily, *2016 white Paper on Sleep and Occupational Safety*, China Daily, Beijing, China, 2016.
- [7] Z. Moussavi, A. Elwali, R. Soltanzadeh, C. A. MacGregor, and B. Lithgow, "Breathing sounds characteristics correlate with structural changes of upper airway due to obstructive sleep apnea," *EMBC*, vol. 2015, pp. 5956–5959, Article ID 7319748, 2015.
- [8] M. A. Serhani, M. E. Menshawy, and A. Benharref, "SME2EM: smart mobile end-to-end monitoring architecture for life-long diseases," *Computers in Biology and Medicine*, vol. 68, pp. 137–154, 2016.
- [9] Q. Jiang, J. Ma, C. Yang, X. Ma, J. Shen, and A. C. Shehzad, "Efficient end-to-end authentication protocol for wearable health monitoring systems," *Computers and Electrical Engineering*, vol. 63, pp. 1–14, 2017.
- [10] C. Massaroni, D. Lo Presti, D. Formica, S. Silvestri, and E. Schena, "Non-contact monitoring of breathing pattern and respiratory rate via RGB signal measurement," *Sensors*, vol. 19, no. 12, pp. 2758–2815, 2019.
- [11] A. Cesareo, Y. Previtali, E. Biffi, and A. Aliverti, "Assessment of breathing parameters using an inertial measurement unit (IMU)-Based system," *Sensors*, vol. 19, no. 1, pp. 88–24, 2018.
- [12] A. Al-Naji, A. J. Al-Askery, S. K. Gharghan, and J. Chahl, "A system for monitoring breathing activity using an ultrasonic radar detection with low power consumption," *Journal of Sensor and Actuator Networks*, vol. 8, no. 2, pp. 32–17, 2019.
- [13] A. Prochzka, H. Charvtov, O. Vysata, J. Kopal, and J. Chambers, "Breathing analysis using thermal and depth imaging camera video records," *Sensors*, vol. 17, pp. 1–10, 2017.
- [14] H. Alshaer, G. R. Fernie, E. Maki, and T. Douglas Bradley, "Validation of an automated algorithm for detecting apneas and hypopneas by acoustic analysis of breath sounds," *Sleep Medicine*, vol. 14, no. 6, pp. 562–571, 2013.
- [15] G. Sierra, V. Telfort, B. Popov, L. G. Durand, R. Agarwal, and V. Lanzo, "Monitoring respiratory rate based on tracheal sounds. First experiences," in *Proceedings of the IEEE Engineering in Medicine and Biology Society Conference 2004*, pp. 317–320, California, CA, USA, September 2004.
- [16] S. Saha, M. Kabir, N. Montazeri Ghahjaverestan et al., "Portable diagnosis of sleep apnea with the validation of individual event detection," *Sleep Medicine*, vol. 69, pp. 51–57, 2020.
- [17] M. Tenhunen, E. Huupponen, J. Hasan, O. Heino, S. L. Himanen, and L. Himanen, "Evaluation of the different sleep-disordered breathing patterns of the compressed tracheal sound," *Clinical Neurophysiology*, vol. 126, no. 8, pp. 1557–1563, 2015.
- [18] F. Jin, F. Sattar, D. Y. T. Goh, and I. M. Louis, "An enhanced respiratory rate monitoring method for real tracheal sound recordings," in *Proceedings of the 17th European Signal Processing Conference*, pp. 642–645, Scotland, UK, August 2009.
- [19] Y. Nam, B. A. Reyes, and Ki H. Chon, "Estimation of respiratory rates using the built-in microphone of a smartphone or headset," *Ieee Journal of Biomedical and Health Informatics*, vol. 20, no. 6, pp. 1493–1501, 2016.
- [20] R. Palaniappan, K. Sundaraj, and S. Sundaraj, "Adaptive neuro-fuzzy inference system for breath phase detection and breath cycle segmentation," *Computer Methods and Programs in Biomedicine*, vol. 145, pp. 67–72, 2017.
- [21] Y. Fang, Z. Jiang, and H. Wang, "A novel sleep respiratory rate detection method for obstructive sleep apnea based on characteristic moment waveform," *Journal of Healthcare Engineering*, vol. 018, pp. 1–10, Article ID 21902176, 2018.
- [22] T. Emoto, U. R. Abeyratne, M. Akutagawa, S. Konaka, and Y. Kinouchi, "High frequency region of the snore spectra carry important information on the disease of sleep apnoea," *Journal of Medical Engineering and Technology*, vol. 35, no. 8, pp. 425–431, 2011.
- [23] L. Almazaydeh, K. Elleithy, M. Faezipour, and A. Abushakra, "Apnea detection based on respiratory signal classification," *Procedia Computer Science*, vol. 21, pp. 310–316, 2013.
- [24] J. Xie, X. Aubert, X. Long et al., "Audio-based snore detection using deep neural networks," *Computer Methods and Programs in Biomedicine*, vol. 200, Article ID 105917, 2021.
- [25] F. Shen, S. Cheng, Z. Li, K. Yue, W. Li, and L. Dai, "Detection of snore from OSAHS patients based on deep learning," *Journal of Healthcare Engineering*, vol. 2020, pp. 1–10, Article ID 8864863, 2020.
- [26] T. Ganchev, N. Fakotakis, and G. Kokkinakis, "Comparative evaluation of various MFCC implementations on the speaker verification task," in *Proceedings of the SPECOM-2005*, no. 1, pp. 191–194, Patras, Greece, October 2005.
- [27] P. Wang, C. S. Lim, S. Chauhan, J. Y. A. Foo, and V. Anantharaman, "Phonocardiographic signal analysis method using a modified hidden markov model," *Annals of Biomedical Engineering*, vol. 35, no. 3, pp. 367–374, 2007.
- [28] R. Zhang and J. Liu, "An improved multi-band spectral subtraction using mel-scale," *Procedia Computer Science*, vol. 131, pp. 779–785, 2018.
- [29] M. Bahoura, "Pattern recognition methods applied to respiratory sounds classification into normal and wheeze classes," *Computers in Biology and Medicine*, vol. 39, no. 9, pp. 824–843, 2009.
- [30] I. Mazic, M. Bonkovic, and B. Dzaja, "Two-level coarse-to-fine classification algorithm for asthma wheezing recognition in children's respiratory sounds," *Biomedical Signal Processing and Control*, vol. 21, pp. 105–118, 2015.
- [31] S. Sun, H. Wang, Z. Jiang, Y. Fang, and T. Tao, "Segmentation-based heart sound feature extraction combined with classifier models for a VSD diagnosis system," *Expert Systems with Applications*, vol. 41, no. 4, pp. 1769–1780, 2014.

Review Article

A Review on the Applications of Time-Frequency Methods in ECG Analysis

Bikash K. Pradhan ¹, **Bala Chakravarty Neelappu** ¹, **J. Sivaraman** ¹, **Doman Kim** ^{2,3},
and **Kunal Pal** ¹

¹Department of Biotechnology and Medical Engineering, National Institute of Technology Rourkela, Rourkela 769008, India

²Graduate School of International Agricultural Technology, Seoul National University, Pyeongchang-gun, Gangwon-do 25354, Republic of Korea

³Institute of Food Industrialization, Institutes of Green Bioscience and Technology, Seoul National University, Pyeongchang-gun, Gangwon-do 25354, Republic of Korea

Correspondence should be addressed to Kunal Pal; kp.al.nitrkl@gmail.com

Received 30 March 2022; Revised 25 May 2022; Accepted 24 November 2022; Published 1 February 2023

Academic Editor: Aiping Liu

Copyright © 2023 Bikash K. Pradhan et al. This is an open access article distributed under the Creative Commons Attribution License, which permits unrestricted use, distribution, and reproduction in any medium, provided the original work is properly cited.

The joint time-frequency analysis method represents a signal in both time and frequency. Thus, it provides more information compared to other one-dimensional methods. Several researchers recently used time-frequency methods such as the wavelet transform, short-time Fourier transform, empirical mode decomposition and reported impressive results in various electrophysiological studies. The current review provides comprehensive knowledge about different time-frequency methods and their applications in various ECG-based analyses. Typical applications include ECG signal denoising, arrhythmia detection, sleep apnea detection, biometric identification, emotion detection, and driver drowsiness detection. The paper also discusses the limitations of these methods. The review will form a reference for future researchers willing to conduct research in the same field.

1. Introduction

The electrocardiogram (ECG) signal has been an indicator of human health. It is the graphical representation of the electrical activity of the heart muscles occurring due to their contraction and relaxation [1]. A single cardiac cycle is labeled using different waves: P, Q, R, S, and T. The location and amplitudes of these waves are used primarily in ECG analysis during medical practices. It helps to predict the onset of cardiovascular diseases, irregularities in heart rhythm, stress levels, human emotions, and so on. A standardized ECG signal is represented via twelve leads, each calculated using a set of limb and chest leads. Conventionally, the ECG waves were visually observed and analyzed by an expert. The evaluation includes detecting any subtle change in the time series information that takes in morphological details such as the RR interval, QT segment, ST segment, QRS complex, and so on [2], and their statistical

variations. Unfortunately, it is not always possible to track the minute changes in the morphological parameters (intervals, peaks, and waves) of the ECG signal.

The ECG signal is nonstationary; i.e., the statistical properties of the signal, such as mean, variance, and higher-order moments, change with time. A nonstationary time series of data contains systematic noise (trends, jumps, and datum shifts) that may change its statistical values. Hence, the time series data analysis is not enough for a meaningful interpretation. Also, the employment of traditional signal processing methods based on stationary assumptions is insufficient. Therefore, the decomposition of the time-series data into another domain, frequency or time-frequency, is used for easy analysis [3]. Fourier transform (FT) is the most widely employed method for frequency analysis. The technique uses the sinusoidal basis function to represent a time series signal in the frequency domain. The amplitudes of the measured sinusoids at different frequencies form

a spectrum. It is one of the transformation methods that has changed the world of signal processing and have diverse application in feature extraction, denoising, and so on. However, FT does not have any information in the time domain.

Joint time-frequency analysis is a valuable method that expresses a signal in the time-frequency distribution [4]. It helps disclose the constituent frequency component of the signals and their time-varying nature. Several time-frequency analysis methods have been proposed to analyze ECG signals in various application domains. These methods include but are not limited to the short-time Fourier transform (STFT), continuous wavelet transforms (CWT), discrete wavelet transforms (DWT), empirical mode decomposition (EMD), and Wigner–Ville distribution (WVD) [5, 6], and so on. These methods help extract the vital signal components such as distortions, noises, and hidden patterns of the ECG waves and have been extensively used in various applications. Also, these methods form the base of several advanced joint time-frequency techniques. Typical examples are arrhythmia detection, heart disease diagnosis, peak detection, signal denoising, and emotion detection [7–9].

Despite the more inclusive application of the joint time-frequency analysis, it is unfortunate that no dedicated review is found in the literature that discusses different time-frequency methods for the ECG application. The reason may be that the time-frequency methods are a massive field with various possible applications. Hence, placing a vast amount of information in a single review is not easy. However, based on our limited knowledge, we have attempted to extensively review some selected time-frequency methods and their use in various ECG signal processing applications in this article (Figure 1). The current paper is organized into four different sections. Section 2 gives background information on the time-frequency methods. The usefulness of these time-frequency methods in various ECG applications has been discussed in Section 3. Section 4 deliberates the limitations, challenges, and future scope, followed by Section 5, concluding the study. Table 1 contains the list of abbreviations used in this article.

2. Background Information of the Time-Frequency Analysis Methods

The time-domain analysis gives the best time resolution but no frequency information. Consequently, the frequency domain analysis provides the best frequency resolution without time-related details. A proper time-frequency technique can overcome the disadvantage of one-dimensional analysis and provide signal information in the time and frequency domain. Some of the most widely used time-frequency analysis methods have been discussed in this section.

2.1. Short-Time Fourier Transform. In 1946, D. Gabor [10], a Hungarian scientist, proposed the short-time Fourier transform (STFT). In STFT, the Fourier transform (FT) is

applied for a limited duration. The process follows a segmented analysis where the original signal is first divided into smaller segments of length “ L ” using a window. The Fourier transform (FT) of each segment is then calculated. In other words, the STFT provides the spectral information of each segment of the signals. For a continuous-time signal $x(t)$, STFT coefficients can be represented mathematically using the following:

$$X(\tau, \omega) = \int_{-\infty}^{\infty} x(t)w(t - \tau)e^{-j\omega t} dt, \quad (1)$$

where $X(\tau, \omega)$ is the FT, w is the window function, τ and ω represent the time and frequency axis.

The original signal “ $x(t)$ ” can be retrieved using the inverse STFT. It is represented using the following equation:

$$x(t) = \frac{1}{2\pi} \int_{-\infty}^{\infty} \int_{-\infty}^{\infty} X(\tau, \omega)e^{-j\omega t} d\tau d\omega. \quad (2)$$

For calculating the STFT of a discrete-time signal, a discrete Fourier transform (DFT) can be used in place of FT. Mathematically, it is represented using the following equation:

$$X[m; k] = \sum_{n=0}^{L-1} x[m+n]e^{-j\omega nk}. \quad (3)$$

Here, m is the starting point of the localized DFT, k is the DFT index, and L is the length of the window or segment. $X[m; k]$ are the Fourier coefficients that depend on the time (n) and frequency (ω).

STFT is a complex-valued function of two variables and requires a 4D plot of time, frequency, magnitude, and phase for the proper interpretation, which is practically not possible. Thus, the phase information is not considered while plotting the STFT spectrogram. In other words, time, frequency, and magnitude values represent an STFT spectrogram. Furthermore, a color-coding method is applied for the magnitude range, where a darker color represents a smaller magnitude value and vice versa. It is important to note that the size of the window shows a profound effect on the frequency resolution. A wider window provides a few time segments, resulting in lower precision in time but a high-frequency resolution. On the other hand, a narrow time window gives a high time resolution but a low-frequency resolution. Since the window length is fixed in the STFT method, the time and frequency resolution are fixed for the entire signal length. Figure 2 is a sample representation of an ECG segment of duration 1 sec. (sampling frequency 360 Hz) and its STFT at varying window lengths ($L = 2, 9,$ and 18). It is evident from Figure 2 that with an increase in the window length, the changes in the time-domain values are less visible. On the contrary, the frequency domain changes are becoming more profound.

2.2. Continuous Wavelet Transform. The wavelet transform (WT) is a processing tool that has been widely used in signal and image processing and speech analysis. In 1984, two French scientists, Grossmann and Morlet, first coined the

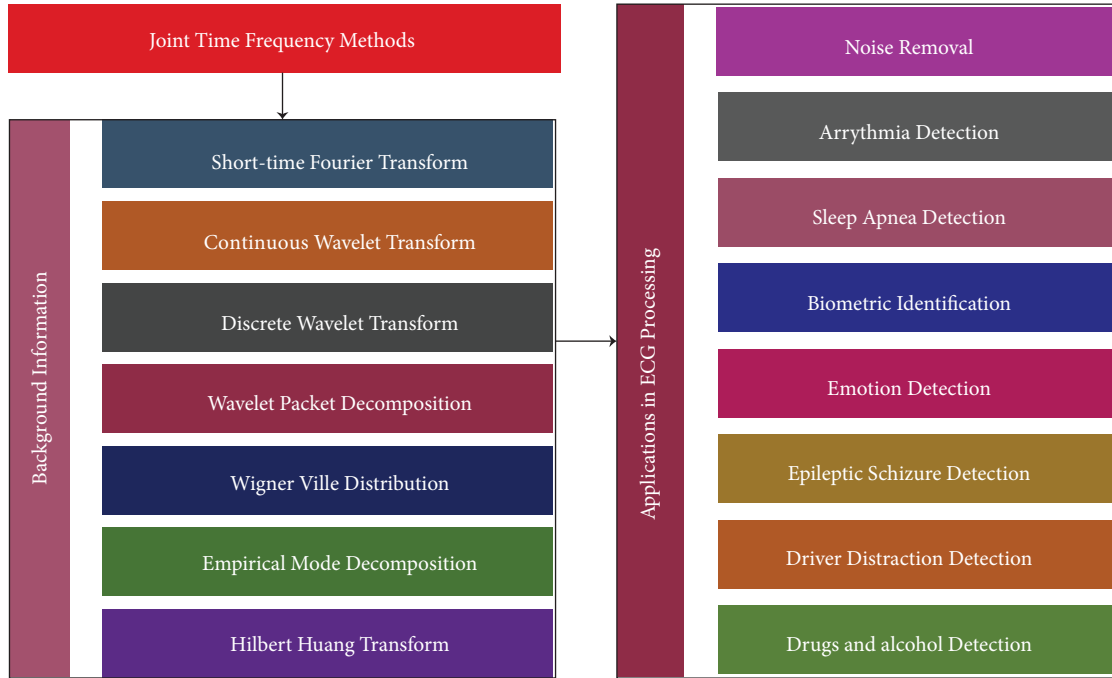


FIGURE 1: Block diagram of the current study.

term “wavelet” and described it as a wave-like structure [11]. A wavelet has an amplitude that starts and ends at zero. The amplitude integral of the wavelets is zero. A detailed historical background of the wavelets is presented in [12, 13]. Several wavelet functions are available with diverse shapes and characteristics. Some common wavelets include Haar, Daubechies, Coiflet, and Symlet. The WT method solves the resolution problem associated with FT by providing a suitable resolution both in time and frequency. It is made possible by adopting a variable window function, wherein the window function shrinks and widens multiple times. The continuous wavelet transform (CWT) decomposes a given signal into different coefficients. Herein, a basis function called the mother wavelet is dilated and translated. Mathematically, the CWT is represented using

$$\text{CWT}_{\tau,s,\Psi}(x) = \frac{1}{\sqrt{s}} \int_{-\infty}^{\infty} x(t) \Psi_{\tau,s}^*(t) dt, \quad (4)$$

where $\Psi_{\tau,s}(t) = 1/\sqrt{s} \Psi(t - \tau/s)$ and $*$ represents the conjugate function.

In equation (4), the term “ $1/\sqrt{s}$ ” is used to normalize the mother wavelet (Ψ). The transformed signal generated after employing the CWT depends on the scaling factor (s) and the translation factor (τ). The scaling factor shows an inverse association with frequency. A lower value of s leads to a rapid change in the wavelet and is used to detect the higher frequencies of the signal and capture the fast-varying details. On the contrary, a higher value of s helps perceive the lower frequency components and captures the slow varying details of the signal.

The reconstruction of the original signal can be obtained using

$$x(t) = \frac{1}{2\pi\Psi} \int_{-\infty}^{\infty} \int_{-\infty}^{\infty} \frac{1}{s^2} \text{CWT}_{\tau,s,\Psi}(x) e^{-j(t-\tau/s)} d\tau ds. \quad (5)$$

Scalogram is the absolute value of the continuous wavelet transform (CWT) as a function of time and frequency. Compared to the spectrogram, a scalogram provides more information as it gives the signal features at different scales. Figure 3 represents a sample ECG signal and its scalogram. As mentioned earlier, it is evident from the figure that the perceived frequency band is getting narrower with an increase in scale. ECG scalogram images are preferably used with deep learning models and have shown potential in various biomedical applications, including arrhythmia detection, apnea detection, and fall detection. The disadvantage of CWT is that it is highly redundant and shows a significant overlap between the wavelets at each scale and between the scale [14]. Furthermore, it is associated with higher computational complexity.

2.3. Discrete Wavelet Transform. Stromberg [15], a Swedish mathematician, proposed the mathematical foundation for the discrete wavelet transform (DWT) in 1980 [16]. A significant drawback of CWT is that the scaling factor (s) and translation factor (τ) value changes rapidly and, hence, calculates the coefficients of the wavelet for all possible scales. Thus, the method yields much new information [17], which is difficult to process. On the contrary, DWT addresses the aforementioned issues of CWT by representing the signal at a discrete time and as a set of wavelet coefficients. In DWT, the signal passes through a low-pass filter (LPF) and a high-pass filter (HPF) that splits the signal into half of the original frequency range [18, 19]. The low-pass filter output is the approximation component (A), and the

TABLE 1: Lists of acronyms.

ECG	Electrocardiogram
STFT	Short-time fourier transform
WT	Wavelet transforms
DWT	Discrete wavelet transforms
WPD	Wavelet packet decomposition
EMD	Empirical mode decomposition
WVD	Wigner-Ville distribution
PWVD	Pseudo Wigner-Ville distribution
SWT	Stationary wavelet transforms
IMF	Intrinsic mode function
HT	Hilbert transform
HHT	Hilbert–Huang transform
EEMD	Ensemble empirical mode decomposition
CEEMD	Complete ensemble empirical mode decomposition
LMD	Local mean decomposition
FDM	Fourier decomposition method
SWT	Stationary wavelet transforms
DTCWT	Dual tree complex wavelet transforms
TQWT	Tunable Q-wavelet transform
LSWA	Least square wavelet analysis
EWT	Empirical wavelet transforms
VMD	Variational mode decomposition
MEMD	Multivariate empirical mode decomposition
CEEMDAN	Complete ensemble EMD with adaptive noise
SVM	Support vector machine
DAE	Deep autoencoder
PPR	Peak positive rate
ANN	Artificial neural network
LDA	Linear discriminate analysis
PCA	Principal component analysis
LDA	Linear discriminant analysis
SNR	Signal to noise ratio
MSR	Mean square error
PSR	Phase space reconstruction
FT	Fourier transforms
DFT	Discrete Fourier transforms
CWT	Continuous wavelet transforms
LPF	Low pass filter
HPF	High pass filter
A	Approximation coefficients
D	Detailed coefficients
ACF	Autocorrelation function
IACF	Instantaneous autocorrelation function
BW	Baseline wander
CVD	Cardiovascular diseases
AF	Atrial fibrillation
VF	Ventricular fibrillation
VT	Ventricular tachycardia
CNN	Convolutional neural network
RCNN	Recurrent convolutional neural network
KNN	K-nearest neighbor
PCA	Principal component analysis
QDA	Quadratic discriminate analysis
OSA	Obstructive sleep apnea
CSA	Central sleep apnea
CVMD	Complex variational mode decomposition
EDR	ECG-derived respiration
HBI	Heartbeat interval
Res Net	Residual neural network
ELM	Extreme learning machine
RF	Random forest

TABLE 1: Continued.

NB	Naive Bayes
DT	Decision tree
DTW	Dynamic time wrapping
GOA	Grasshopper optimization algorithm
NLM	Nonlocal mean
FIBFs	Fourier intrinsic band function
SURE	Stein's unbiased risk estimate

high-pass filter output is the detailed component (D). The approximation component is further decomposed to form another set of approximation and detailed components in each subsequent level. Figure 4 represents the wavelet filter belts for DWT, where the $x(n)$ is the original signal, and A and D bear their usual meaning.

DWT can be of two types based on whether each filter's output is down-sampled by two or not. If the filter output is down-sampled during the decomposition process, it is called a decimated DWT. Undecimated DWT, also known as stationary wavelet transform (SWT), is the method that doesn't incorporate the down-sampling operation at the filter output. Thus, in the case of SWT, the length of the approximation and the detailed coefficient are the same as the original signal. Usually, the term DWT represents the decimated method by default and is most commonly used due to its lower computational complexity than the undecimated method.

For a time-series signal, $x(n)$ has the number of samples m , i.e., n ranges from 0 to $m-1$. The scaling function $W_\varphi(j_0, k)$ and the wavelet function $W_\Psi(j, k)$ for the forward wavelet transform can be represented using the following equations:

$$W_\varphi(j_0, k) = \frac{1}{\sqrt{m}} \sum_n x(n) \varphi_{j_0, k}(n), \quad (6)$$

$$W_\Psi(j, k) = \frac{1}{\sqrt{m}} \sum_n x(n) \Psi_{j, k}(n). \quad (7)$$

Then, the signal $x(n)$ can be represented (equation (8)) using the scaling and wavelet functions.

$$x(n) = \frac{1}{\sqrt{m}} \sum_k^\infty W_\varphi(j_0, k) \varphi_{j_0, k}(n) + \sum_{j=j_0}^\infty \sum_k^\infty W_\Psi(j, k) \Psi_{j, k}(n), \quad j \geq j_0. \quad (8)$$

Equation (8) is also known as an inverse discrete wavelet transform. Figure 5 represents a sample representation of an ECG signal and its DWT coefficients after the 3rd level of decomposition using the db2 mother wavelet.

2.4. Wavelet Packet Decomposition (WPD). Wavelet packet decomposition (WPD) extends the DWT, where the approximation and detailed coefficients are decomposed in the

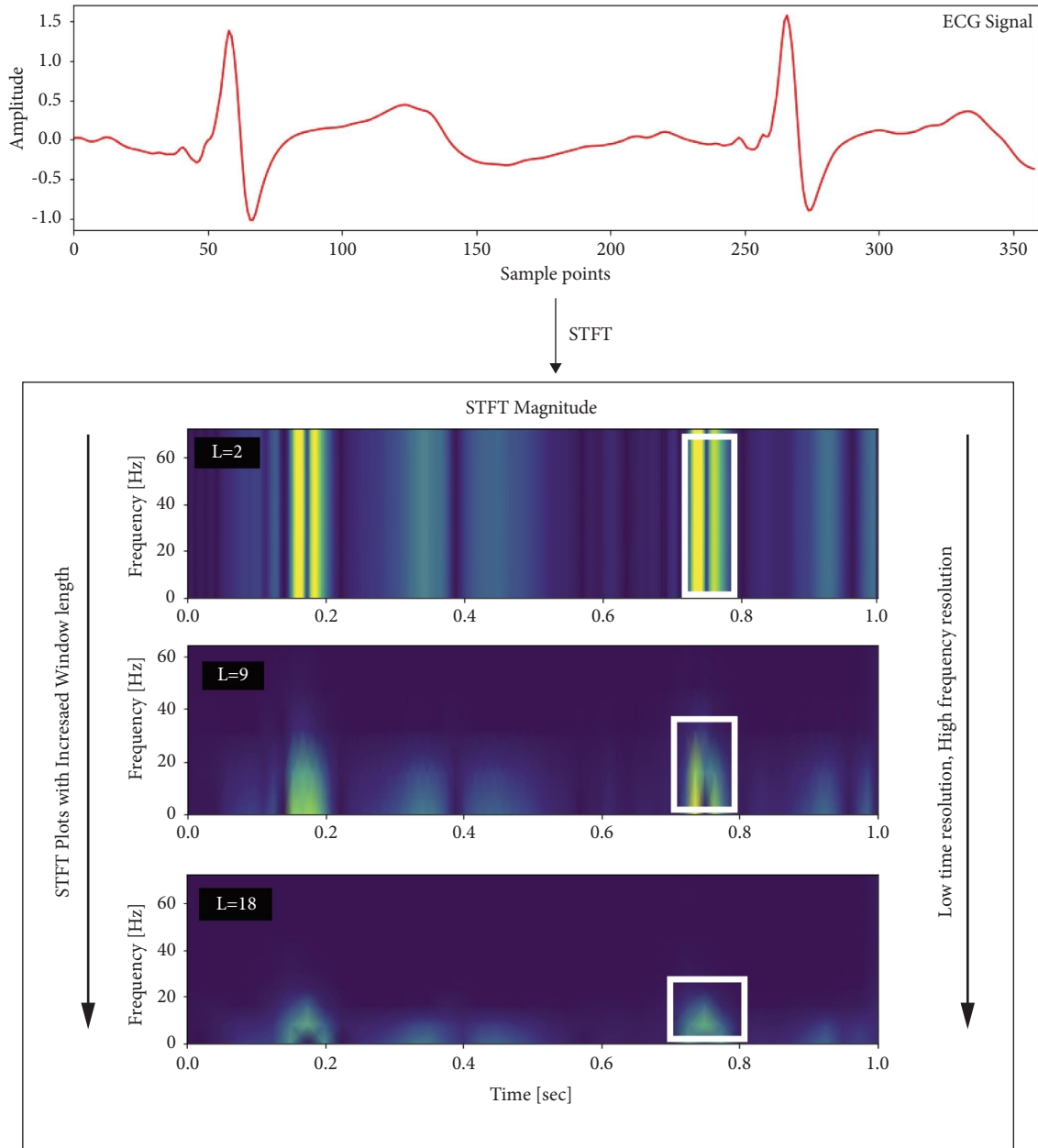


FIGURE 2: A sample ECG signal and its STFT at different window lengths.

subsequent level. Hence, WPD provides a better frequency and time resolution compared to DWT. Figure 6 represents the wavelet filter belts for WPD, where $x(n)$, A, and D bear their usual meaning, as described in Section 2.3. Similar to the DWT, the WPD can be of two types: decimated and undecimated. Generally, WPD follows the decimated method. A sample ECG signal and its wavelet coefficients after the 2nd level of decompositions using the db2 mother wavelet are represented in Figure 7.

2.5. Wigner-Ville Distribution (WVD). Wigner [20], a Hungarian physicist in the year 1932, proposed the basis of the Wigner-Ville distribution (WVD) function. WVD is the quantitative representation of signal energy in the time-

frequency domain. This method uses the autocorrelation function for the calculation of the power spectrum. The autocorrelation function (ACF) compares a signal ($x(t)$) to itself for all possible time shifts (τ) and is represented using the following equation:

$$ACF_x = \int x(t)x(t + \tau)dt. \quad (9)$$

In the ACF, the signal is integrated over a period of time, which makes it a function dependent only on τ . However, the WVD uses a variation of the ACF called the instantaneous autocorrelation function (IACF) to maintain the time parameter, and it is represented using the following equation:

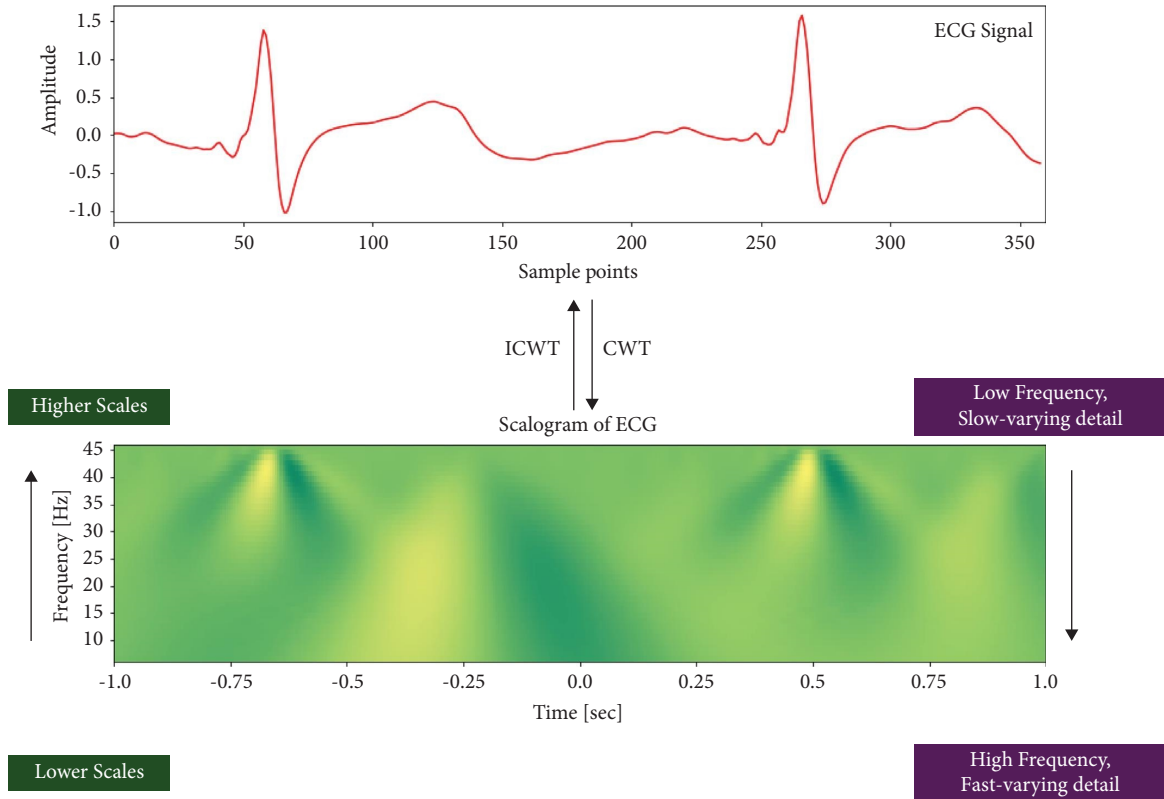


FIGURE 3: A sample ECG signal and its scalogram at a scale range of 0–45.

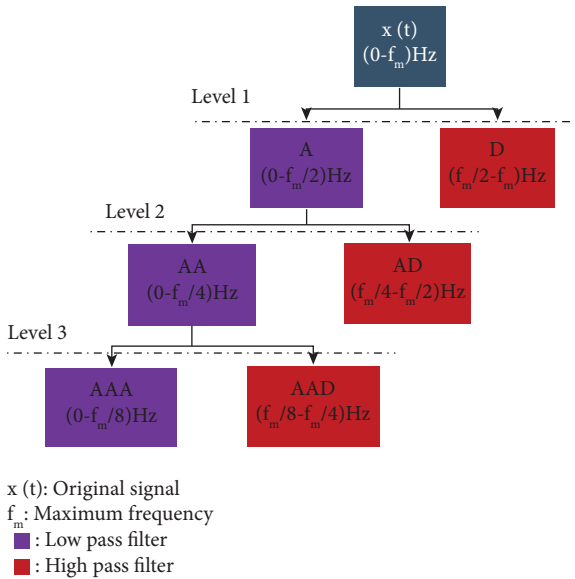


FIGURE 4: A representation of the DWT decomposition tree at level 3.

$$IACF = x\left(t + \frac{\tau}{2}\right)x^*\left(t - \frac{\tau}{2}\right). \quad (10)$$

The WVD function compares the signal information with its own at different times and frequencies. It can be viewed as the FT of the IACF.

Mathematically, it is defined using the following equation (11):

$$WVD_x(t, \omega) = \frac{1}{2\pi} \int_{-\infty}^{\infty} x\left(t + \frac{\tau}{2}\right)x^*\left(t - \frac{\tau}{2}\right)e^{-j\omega\tau}d\tau. \quad (11)$$

Compared to STFT, WVD gives better spectral resolution as it does not suffer from leakage. However, when a signal has several frequency components, it may be affected by the cross-term [21]. A cross-term occurs when multiple parts exist in the input signal, analogous in time and frequency beats. The cross-term can be minimized by modulating the WVD function by applying a sliding averaging window in the time-frequency plane. It is regarded as pseudo-WVD (PWVD) [22] and is more widely used than WVD. However, it reduces the effect of cross-terms to some extent but does not eliminate it.

Mathematically, the PWVD is represented using the following equation (12):

$$PWVD_x(t, \omega) = \frac{1}{2\pi} \int_{-\infty}^{\infty} h(t)x\left(t + \frac{\tau}{2}\right)x^*\left(t - \frac{\tau}{2}\right)e^{-j\omega\tau}d\tau. \quad (12)$$

Figure 8 represents the PWVD of an ECG signal (360 Hz, duration 1 sec). Each data point in the WVD plot is represented with three signal variables: amplitude, time, and frequency.

2.6. Empirical Mode Decomposition. Empirical mode decomposition (EMD) is a local and data-driven adaptive method that is mainly applied to nonlinear and non-stationary signals. EMD splits a signal into many nanocomponent functions called Intrinsic Mode Functions (IMFs) [23]. The IMF holds

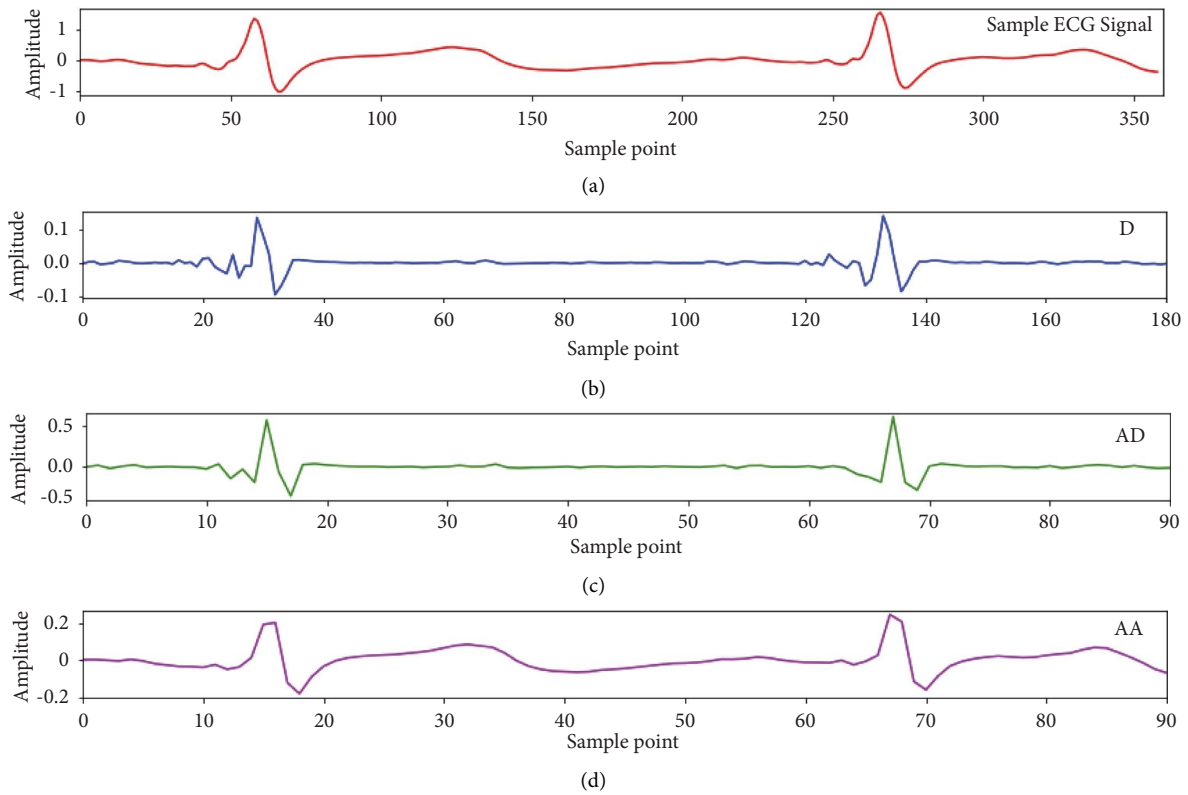


FIGURE 5: (a) A sample ECG signal and (b-d) its DWT coefficients after the 2nd level of decomposition using a db2 mother wavelet.

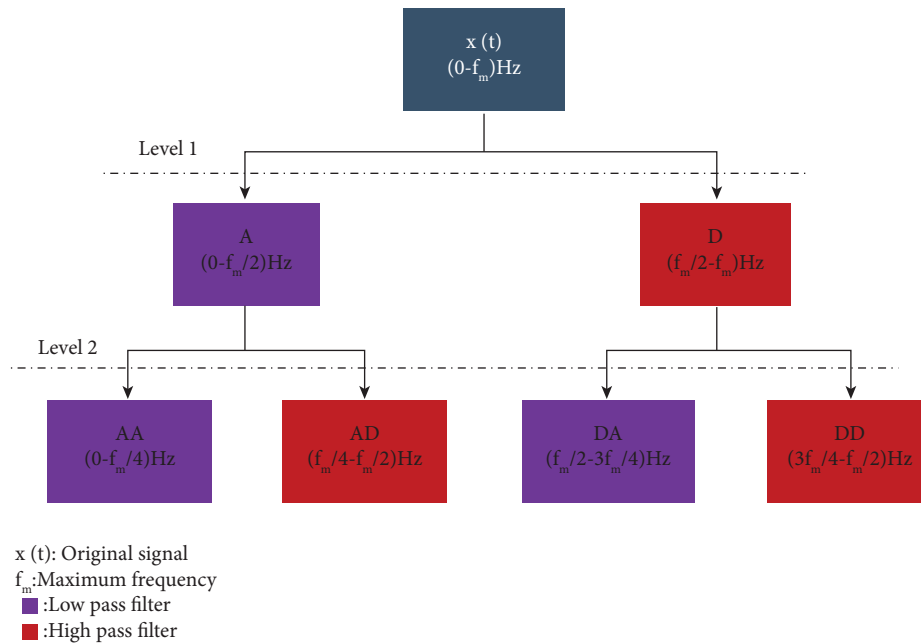


FIGURE 6: A representation of the DWT decomposition tree at level 3.

a relationship between phase and frequency. An IMF must satisfy two conditions: (1) For a given signal, the number of zero crossings and the number of extrema must be equal to zero; if not, it must differ by one. (2) The mean of the envelope created due to the local maxima (peak of a wave) and the local

minima (valley) is zero. In other words, the IMF represents only the simple oscillatory modes present in a signal. However, it does not ensure a perfect instantaneous frequency in all conditions. In [24], Peng et al. (2005) proposed an algorithm to extract the IMFs of a signal.

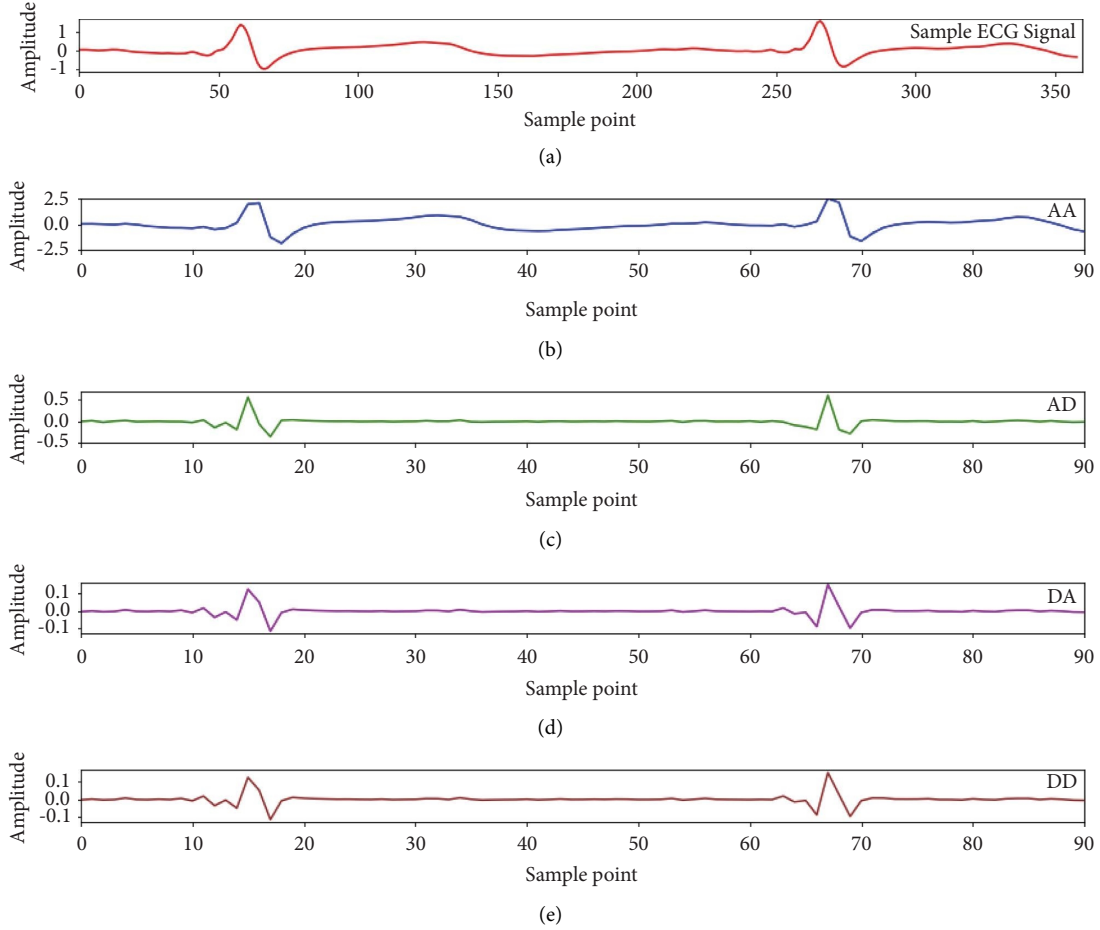


FIGURE 7: (a) A sample ECG signal and (b-e) its WPD coefficients after the 2nd level of decomposition using the db2 mother wavelet.

After the decomposition process, the original signal is characterized as the combination of the extracted IMFs and the residues r_{i+1} . Mathematically, it can be represented using the following equation (13):

$$x(t) = \sum_{i=1}^n \text{IMF}_i + r_{i+1}. \quad (13)$$

Figure 9 represents a sample ECG signal and the set of extracted IMFs and residues (Figure 8(b)). The figure also illustrates the instantaneous frequencies (Figure 9(c)). It can be observed from the figure that the lower IMFs capture fast oscillatory modes. On the contrary, the higher-order IMFs capture the slow oscillation modes. The limitation of the traditional EMD method is mode mixing in the case of signals with closely spaced frequencies [25].

2.7. Hilbert Huang Transform. The Hilbert Huang Transform (HHT) is an extension of EMD. It is the application of the Hilbert transform (HT) to the extracted IMFs. After finding all the IMFs from the original signal, the HT is applied to get the $d_i(t)$ from each IMF_i . Mathematically, it is represented using the following equation (14):

$$z_i(t) = \text{IMF}_i + jd_i(t) = A_i e^{j\theta_i}, \quad (14)$$

where $z_i(t)$ is the analytic signal obtained using the Hilbert transform of the IMFs.

$$A_i = \sqrt{\text{IMF}_i^2 + d_i(t)^2},$$

$$\theta_i(t) = \tan^{-1} \frac{d_i(t)}{\text{IMF}_i}, \quad (15)$$

$$\omega_i = \frac{d\theta_i}{dt}.$$

Replacing IMF_i with $z_i(t)$ in equation (14) and neglecting the value of r_{i+1} , it yields

$$x(t) = \text{Real} \left(\sum_{i=1}^n A_i e^{j\theta_i(t)} \right), \quad (16)$$

where $\theta(t)_i = \int_0^t \omega_i(t) dt = \arctan(d_i/\text{IMF}_i)$.

At the output, the HHT produces an orthogonal pair for each IMF that is phase-shifted by 90°. In addition to the orthogonal pair, the IMF calculates the instantaneous variation in its magnitude and frequency over time. Hence, HHT can be a helpful method when analyzing nonlinear and nonstationary time series data.

2.8. Some Modified Joint Time-Frequency Methods. The aforementioned joint time-frequency methods form the basis of many advanced methods, which have been proposed

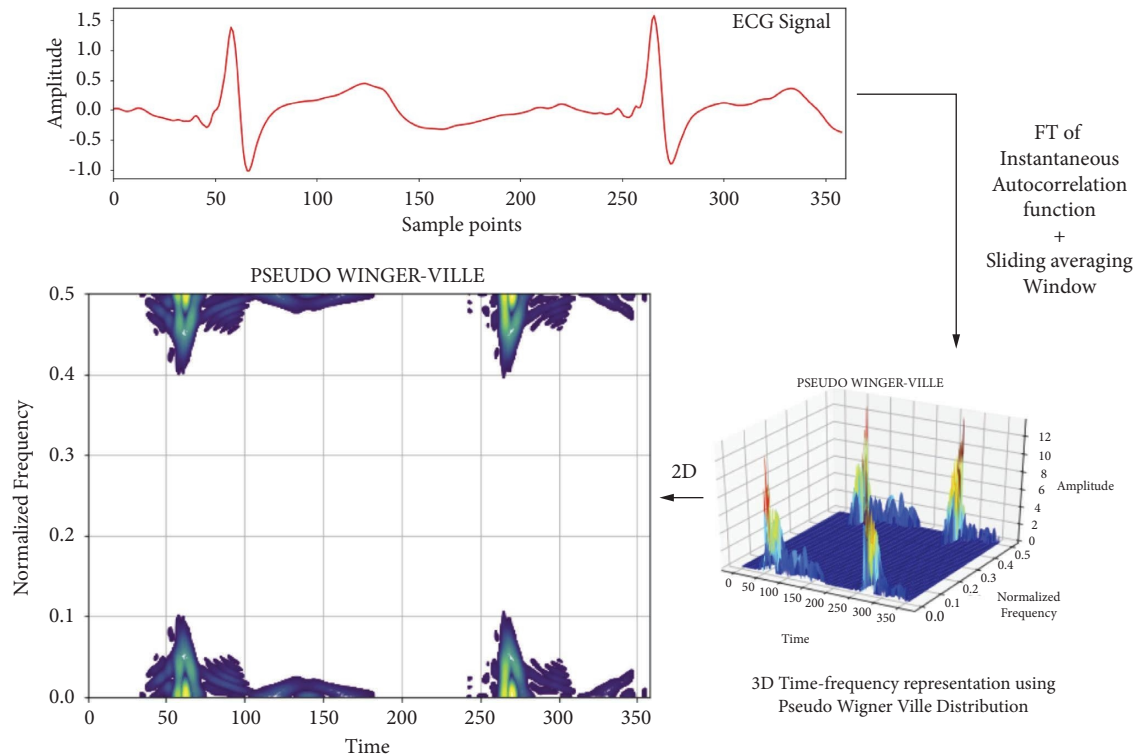


FIGURE 8: A representative figure of a sample ECG signal and its pseudo-Wigner-Ville plot.

in recent years. These advanced methods try to eliminate the limitations associated with the original techniques. Hence, these advanced methods have gained much attention in many signal-processing applications. Initially, it has been a general consideration that the Fourier transform method is applicable only for the spectral analysis of stationary signals. However, a modified Fourier transform method was recently developed for nonlinear and nonstationary signals application. This method is called the Fourier decomposition method (FDM) and has been employed as a time-frequency analysis tool [26]. Several-modified wavelet analysis methods, including least-square wavelet analysis (LSWA) and least-square cross wavelet analysis (LSCWA), have also been proposed [27]. Numerous variations in wavelet transformation methods have been reported recently. This includes tunable Q-wavelet transform (TQWT) [28], stationary wavelet transform (SWT) [29], empirical wavelet transform (EWT) [30], and dual-tree complex wavelet transform (DTCWT) [31]. The advantage of the TQWT is that it does not require the adjustment of the wavelet base function and can easily be adjusted according to the signal [32]. SWT shows the local time-frequency characteristics of a signal and has multiresolution analysis capability [33]. The EWT method is an adaptive wavelet method that uses a wavelet subdivision scheme. The method segments a signal's spectrum and perfectly reconstructs the input signal [34]. DTCWT shows several advantages compared with DWT. These include approximate shift-invariance, directional selectivity, and perfect reconstruction of the original signal [34]. Also, compared to other numerical methods, DTCWT is faster and more effective.

The empirical mode decomposition (EMD) method has also received several improvements in the last decade and has formed the base for a number of decomposition methods [35], that include variable mode decomposition (VMD) [36], complex variable mode decomposition (CVMD) [37], Local mean decomposition (LMD) [38], ensemble empirical mode decomposition (EEMD) [39], multidimensional EEMD [40], complex EMD (CEMD) [41], Complete EEMD with adaptive noise (CEEMDAN) [42], and multivariate empirical mode decomposition (MEMD) [43]. VMD is an adaptive EMD method where the signal decomposes into many band-limited IMFs. The main advantage of VMD over EMD is that it eliminates the effect of mode-mixing during the decomposition process [44]. The LMD method produces a set of product functions after the decomposition process. Here, the time-frequency distribution of the original signal could be acquired from the instantaneous amplitude and frequency of the product functions [45]. The EEMD and CEEMDAN methods also eliminate the mode mixing issues of the EMD method by performing the decomposition over an ensemble of the signal with Gaussian white noise [46].

Modifications in the Wigner–Ville distribution functions resulted in pseudo-Wigner–Ville distribution (PWVD) [47] and smoothed pseudo-Wigner–Ville distribution (SPWVD) [48]. The HHT, as mentioned above, is also an advanced method of EMD, where the Hilbert spectral analysis is employed for each IMFs. The following section reports applying the aforementioned time-frequency methods in various ECG signal processing studies.

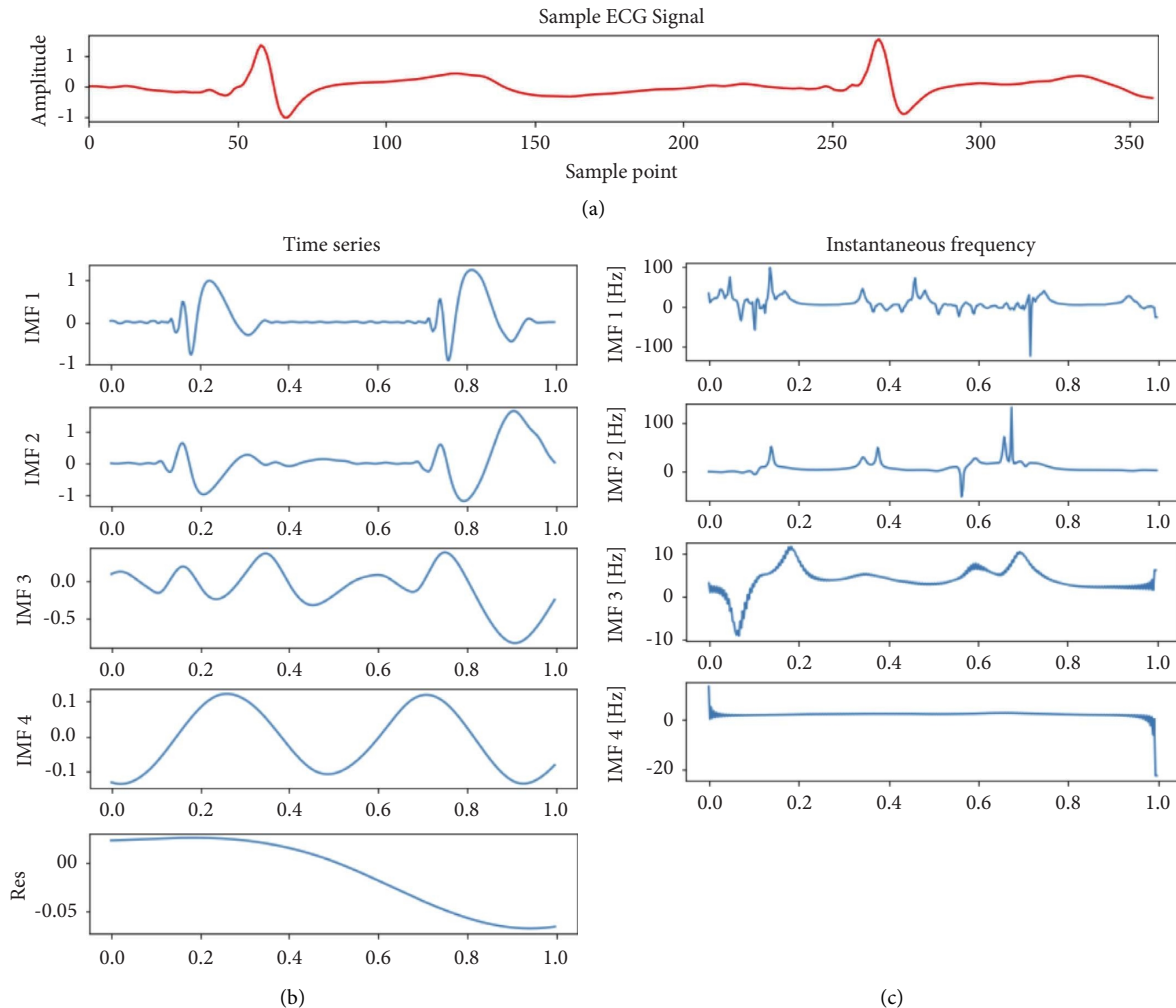


FIGURE 9: (a) A sample ECG signal, (b) IMFs and residue of the ECG signal after EMD, and (c) the instantaneous frequency of each IMF.

3. Applications in ECG Signal Analysis

The advancement in ECG signal processing methods has diversified its applications, both biological and non-biological. Including various joint time-frequency methods in ECG processing has made the process efficient to a significant extent. The biological applications may include, but are not limited to, detecting abnormalities in heart rhythm, the onset of a seizure, sleep apnea, and so on. On the other hand, the nonbiological applications may consist of emotion detection, biometric identification, drug and alcohol detection, the removal of noise from the ECG signal, and so on. This section contains some of the most notable applications of joint time-frequency methods in ECG analysis.

3.1. Noise Removal. The acquisition of the clinical ECG signal is a noninvasive procedure that involves amplifying the biopotential signals using high-gain amplifiers obtained with surface electrodes placed over the skin. A conducting gel is also applied between the skin and electrode surfaces to reduce the skin-contact impedance and maintain proper conductivity. During the acquisition of the ECG signals, the

signal may get contaminated with different noises. The primary noise sources in an ECG signal are power line interference, electrode instability due to improper adherence of the surface electrodes to the skin surface, and muscle activity. These noises are correlated with the original signal with a similar temporal distribution. However, they differ by intensity level. The noise signal possesses a variety of frequency bands, where the low, medium, and high-frequency bands signify the baseline wander (BW), power line interference, and electromyographic noise, respectively.

3.1.1. Baseline Wanders. The BW noise is prominent in the ECG signal at less than 1 Hz. Several factors may lead to this noise, including changes in electrode-skin polarization voltage, respiration, motion artifacts, and electrode, and cable movement. The peak amplitude and duration may vary according to electrode properties, skin contact impedance, electrolytes used, and electrode movement. This noise causes a shift in the isoelectric line during recording, hence, the name BW. The baseline drift is usually seen at a shallow frequency of 0.014 Hz in the ECG recordings.

3.1.2. Powerline Noise. The power line noise is mainly associated with the signal-carrying cables of the device. These cables are prone to electromagnetic interference at 50 Hz or 60 Hz. The two allied mechanisms that aid in powerline interference are capacitive and inductive coupling. However, in the case of the ECG, inductive coupling is more significant.

3.1.3. EMG Noise. The ECG data are acquired using surface electrodes placed over the human skin. It is important to note that various muscles are present underlying the human skin tissue. The contraction and relaxation of these muscles lead to the corruption of the ECG signals with the EMG signals from the underlying muscle tissues. The EMG noise is more defined in the case of differentlyabled persons, kids, and persons with tremor issues.

3.1.4. Electrode Contact Noise. As mentioned above, a conductive gel is usually used on the skin surface before the electrode placement, which acts as a dielectric medium and ensures good conductivity between the two electrodes (the skin surface and the measuring electrode). Electrode contact noise occurs when there is a change in the contact position of the electrodes to the skin. The loosening of the electrode contact may also contribute to the noise. Additionally, poor conductivity between the electrode and the skin surface decreases the amplitude and increases the probability of disturbance by reducing the signal-to-noise ratio (SNR). Maintaining the skin contact impedance as low as possible is advisable to ensure better conductivity between the skin surface and the measuring electrode.

The noise components in the signal contribute to its wrong interpretation, faulty observation, and inefficient feature extraction. Hence, removing the contaminants from the signal is crucial before further processing. Initially, moving average filters were used for this purpose, but they lost a lot of information due to averaging [49]. Various digital and adaptive filters were reported for baseline wander removal and motion artifacts [50]. However, determining the correct filter parameter is a difficult task. Again, these methods primarily focus on a single noise source. Time-frequency methods became popular as they can help remove multiple noises simultaneously. Various time-frequency methods, including wavelet transforms [51], EMD [52], WPD [53], and their variants, have been used in the literature for noise reduction. The conventional denoising steps include signal decomposition, identifying the decomposed signals where most of the noise is content, filtering these noises, and reconstructing the original signal. Figure 10 represents the basic steps involved in ECG denoising. Table 2 contains a comprehensive list of published papers that employed time-frequency-based methods to denoise the ECG signals in recent years.

3.2. Arrhythmia Detection. Cardiovascular disease (CVD) is one of the prime reasons for human death. As per reports, it contributed to 31% of the worldwide death in 2016. Out of

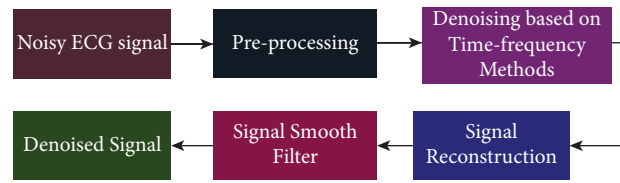


FIGURE 10: The basic signal processing steps involved in ECG signal denoising.

these, 85% are due to a heart attack. Timely and early detection of the onset of the disease can help in reducing these statistics. Arrhythmia is a common manifestation of CVD known as heart rhythm disorder. It happens when there is an anomaly in the electrical conduction pattern of the heart. Though there are several forms of arrhythmia, namely, sinus node arrhythmia, atrial arrhythmia, junctional arrhythmia, and atrioventricular block [77], atrial fibrillation/arrhythmia is the most common. Usually, the irregular heartbeat does not show any harmful symptoms until it reaches a higher state, leading to a stroke, congestive heart failure, long-term or short-term paralysis, and sometimes even death. Thus, early detection of the progression of AF is crucial. The conventional way of diagnosing CVD is through a patient's medical history and clinical tests. However, this method requires highly heterogeneous data and a medical expert for accurate prediction and interpretation, making the process inefficient. Also, the problem is more significant in places with a shortage of proper medical facilities. Therefore, for decades, researchers have been opting for a machine-based automatic system that uses physiological signals (ECG) for monitoring and diagnosis. Most of these diagnostic procedures follow a standard method, including ECG signal acquisition, decomposition, feature extraction, and classification for arrhythmia. The current section addresses different time-frequency-based methods in arrhythmia detection and their present status. Although several time-frequency methods have been employed for arrhythmia detection, wavelet-based methods have been widely explored in recent years. The discrete wavelet transform (DWT) is most prevalent due to its easy implementation. Figure 11 represents the block diagram of a DWT-based beat classification method, followed by Rizwan et al. (2022) [78]. Besides DWT, other methods, such as WPD and CWT, have also been employed. The CWT method is not widely used as the inverse CWT is not available in many standard toolboxes (MATLAB, Python, etc.) due to its high computational cost [79]. However, in many studies, the DWT and CWT were combined to improve classification accuracy. WPD, on the other hand, resulted in a larger feature set compared to the DWT method and showed potential in classifying arrhythmia. However, it is associated with high computational complexity. Some other time-frequency methods and their variants that have also been recently explored include EMD, HHT, WVD, and STFT. The STFT has been combined with deep neural networks such as recurrent neural networks (RNN) and convolutional neural networks (CNN) to obtain efficient results. Table 3 lists some of the recently published articles and discusses the time-frequency methods used, the

TABLE 2: List of published papers in the last five years that have used the time-frequency methods for denoising ECG signals.

Literature	Type of noise	Time-frequency method used	Method
El Bouny et al. (2017) [54]	—	Ensemble EMD (EEMD)	The EEMD method was employed to determine the IMFs, then the IMFs containing sufficient information about the QRS complexes were determined using kurtosis. Two EEMD interval thresholding methods were applied to reduce the noise, and then the original ECG signal was reconstructed.
Rachakonda and Mahesh (2019) [55]	Single or combined noise	WPD and complete ensemble empirical mode decomposition (CEEMD)	Herein, both WPD and CEEMD methods were employed separately, and then their efficacy in reducing the noise was compared. The process follows three typical steps: signal decomposition, short-term temporal feature extraction, and decision rule.
Low and Choo et al. (2018) [56]	Baseline noise, high and low-frequency noises	DWT	Electrocardiogram and phonocardiogram signals were denoised using the DWT with a thresholding technique.
Fehér (2017) [57]	Baseline wandering and high-frequency noise	DWT	The DWT method generated the wavelet coefficients with a suitable mother wavelet. The baseline wander was removed by scaling the average coefficient. Consequently, the high-frequency noise was removed by employing Stein's unbiased risk estimate (SURE) algorithm to the detailed coefficients. Finally, the signal was reconstructed.
Warrier et al. (2020) [58]	All noise type	DWT, EMD	The DWT and EMD methods and two other techniques (singular value decomposition and artificial neural network) were employed individually and combinedly to find the best suitable way to reduce noise in the ECG signal.
Kapoor and Birok (2020) [59] Thakran (2020) [60]	Overall noise	EEMD	Herein, the noise removal procedure follows two phases. The IMF's were generated from the noisy signal using the EEMD method in the first phase. By measuring the spectral flatness and the fuzzy thresholding, the noisy IMFs were identified and filtered with the help of a genetic particle filter. Finally, the signal was reconstructed.
Zhang et al. (2019) [61]	Overall noise	DWT	After decomposing the ECG signal using the DWT method, the noisy wavelet coefficients requiring thresholding were identified using wavelet energy. These coefficients were filtered using a sub-band smoothing filter, and finally, the signal was reconstructed.
Xiong et al. (2019) [62]	In-band noise	EMD	A novel EMD-based denoising method was proposed by analyzing the frequency bands of the IMF components and studying the random noise.
Li et al. (2017) [63]	Power line noise	WPD	A wavelet denoising method was proposed by employing wavelet decomposition, adaptive thresholding, and reconstruction steps.

TABLE 2: Continued.

Literature	Type of noise	Time-frequency method used	Method
Kumar et al. (2018) [64]	Overall noise, noise present in the P and T-wave	EMD	The EMD with the nonlocal mean (NLM) technique was used for denoising the ECG signals. The method uses the differential standard deviation for denoising.
Patro et al. (2021) [65]	Overall noise content	EMD	First, the noisy IMFs were identified after decomposition using EMD. The signal noise was removed using hard thresholding, and then the signal was reconstructed from the filtered IMFs.
Vargas and Veiga (2020) [66]	Baseline wander, power line interference	EMD	The IMFs were processed using a decision method based on the Viterbi algorithm, and then the original signal was reconstructed using the processed IMFs.
Dwivedi et al. (2020) [67]	Powerline interference, baseline wander	EMD	The SWT method was employed for each IMFs to remove the noise content and then reconstructed using the processed IMFs.
Alyasseri et al. (2018) [68]	Overall noise content	DWT	It employs the β -shill-climbing method to determine the best suitable wavelet parameter that produces the minimum mean square error (MSE) between the original and denoised signals.
Taralunga et al. (2015) [69]	Powerline interference (PLI)	HHT	The power line interference was removed by employing an adaptive filter based on HHT.
Singhal et al. (2020) [70]	BW and PLI	FDM	The study uses the FDM decomposition method to remove the baseline wander and power line interference.
Dwivedi et al. (2021) [67]	PLI noise	EMD + SWT, EEMD + SWT	The IMFs were computed using the two EMD methods. Then, each IMF was decomposed using a 3-level SWT method, and the signals were reconstructed using only the detailed coefficients. The results suggested that the inclusion of the SWT method along with EMD and EEMD has reduced the noise up to 9 dB.
Malik et al. (2021) [71]	50 Hz sinusoidal noise, white noise	SWT	The SWT and NLM filtering methods were employed on the decomposed IMFs to remove the AC noise and white noise from the ECG signal.
Kumar et al. (2021) [72]	Overall noise content	SWT	The denoising technique based on SWT was compared with other filter-based denoising methods. The result suggested that the SWT method outperforms the rest and also restored the R peak.
Malghan and Kumar Hota (2021) [73]	Muscle artefact	VMD	The study proposes a unique filtering technique based on the grasshopper optimization algorithm (Goa) based VMD method that uses the dynamic time warping (DTW) distance concept. The method was also compared with the existing methods and showed better performance in eliminating the muscle artifacts.

TABLE 2: Continued.

Literature	Type of noise	Time-frequency method used	Method
Liu et al. (2018) [74]	PLI and muscle artefacts	EMD and EEMD	The noisy ECG signal was first decomposed using the EMD or EEMD method to obtain the IMFs. Then, the IMFs with a signal-to-noise ratio lower than the threshold values were removed, and the ECG signal was reconstructed using the rest of the IMFs.
Mohguen and Bouguezel (2021) [75]	Overall noise content	EEMD	The IMFs obtained after employing the EEMD algorithm applies a modified thresholding method to reduce the noise and preserve the QRS complex.
Malik et al. (2022) [76]	BW and PLI	EMD + lifting wavelet transform (LWT)	A multilevel LWT method was applied to the IMFs of the ECG signals. The obtained coefficients containing the noise were set to zero using a hard thresholding method. The signal is then reconstructed using the inverse method.
Prashar et al. (2020) [51]	Overall noise content	DTCWT	The noisy signals were decomposed using the DTCWT technique. A thresholding method was employed to eliminate the noise, and then the original signals were reconstructed. Herein, a set of thresholding techniques has been evaluated. The result showed that universal modified threshold level-dependent thresholding with the nonnegative garrote function outperformed the other methods.

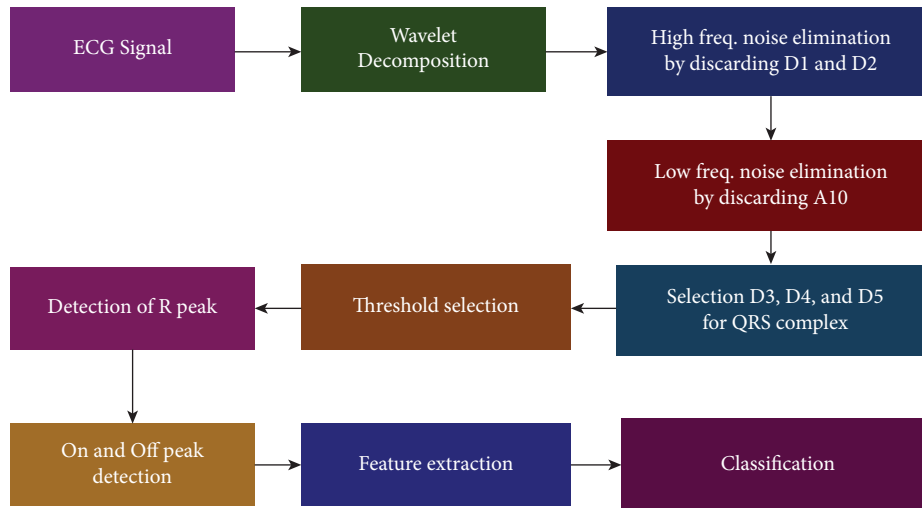


FIGURE 11: Block diagram of a DWT-based Beat classification method (reproduced from [78]).

features computed, and the classification method followed for automatic cardiac arrhythmia detection.

3.3. Sleep Apnea Detection. A good quality of sleep is crucial for leading a healthy life. Sleep apnea is the most common pathological condition that affects sleep quality [118]. It arises due to repetitive airflow obstruction and causes disturbed breathing during sleep time [119]. As per a recent report, around 1 billion people across the globe are affected by sleep apnea [120]. Nine hundred thirty-six million people aged between 30 and 69 have mild to severe obstructive sleep apnea (OSA), whereas 425 million have moderate-to-severe OSA. It has been reported that sleep apnea raises the cardiac disease risk by three times, the accident rate by seven times, and stroke by four times. OSA in the later stage can cause severe cardiovascular and neurocognitive problems if left untreated. Hence, early and timely detection of the disease is crucial. The conventional way of measuring sleep apnea is by performing polysomnography, in which the patient is asked to sleep after attaching several electrodes and sensors for the measurement. The test was performed in a controlled environment. However, the procedure is highly uncomfortable for the patient and may degrade sleep quality. Also, a dedicated person is required who can continuously monitor various physiological signals associated with brain activity, eye movement, muscle activity, etc. The process is time-consuming and expensive [121]. Accordingly, there is a need for a simple, low-cost, and automated method for its detection.

In recent years, researchers have implemented various physiological signals to detect OSA. However, the ECG signal is the most widely used physiological signal for the said purpose. This is because the acquisition of the ECG signal requires only a single-lead recording, which makes the measurement process simpler than other methods. Figure 12 describes the basic steps involved in sleep apnea detection. The current section discusses the application of different time-frequency analysis methods to the ECG signals to

detect OSA. Hassan et al. (2015) used a single-lead ECG signal to classify the OSA in their research. They employed EMD, higher-order statistical features, and an extreme learning machine (ELM) for classification purposes. The authors reported a maximum accuracy of 83.77%. In [123], the authors used an eight-level wavelet packet analysis method on a short-duration (5 s) ECG signal to differentiate between central sleep apnea (CSA) and obstructive sleep apnea (OSA). CSA occurs when the brain is unable to send proper signals to the muscles associated with breathing. It is different from OSA, where normal breathing is hindered due to upper airway obstruction. In a similar study [124], the authors used wavelet-based ECG features to differentiate the CSA and OSA using an auto-regressive ANN classifier. They achieved a classification accuracy of 78.3%. Several other time-frequency methods, including DWT, and HHT, have also been used to classify sleep apnea. Table 4 summarizes some recently published articles in the field that use time-frequency methods during ECG processing.

3.4. Biometric Identification. Identification technologies are crucial in safety, security, and information protection [138]. The earlier approaches, including security keys, passwords, and certificates, are no longer secure as there is a high chance that they may be stolen or forgotten. Hence, biometric identification technology has emerged with great efficiency, considering the anatomical and physiological differences [138, 139]. Typical biometric examples include fingerprints, iris, and face IDs [140]. Even though these methods have been used with great popularity, they are not perfect enough as they can be forged. Recently, it has been found that the ECG signal can be used as a biometric as it is universal, stable, and easily measurable [141]. Again, the ECG of an individual solely depends upon the body shape, gender, age, emotional and the heart's physiological status. It makes the ECG a unique signal. In general, visually differentiating the ECG signal of two individuals is very challenging due to the subtle changes in amplitude and duration. Hence, this

TABLE 3: List of published papers in the last five years that have used the time-frequency methods for arrhythmia detection.

Author, year	Time-frequency method used	Feature used	Inference
Gupta et al. (2020) [80]	STFT	Katz fractal dimension, frequencies of QRS complex, an average of successive R-R peak distance	In this study, the authors proposed to employ STFT and chaos analysis to extract the ECG features. These features were then used to efficiently classify the arrhythmia with a positive predictive value and sensitivity of 99%.
Haleem et al. (2021) [81]	STFT	ECG spectrogram	The spectrogram of the ECG beats from each group was calculated and then employed in a convolutional neural network (CNN) for classification purposes. Overall classification accuracy of 95% was achieved.
Sultan Qurraie and Ghorbani Afkhami (2017) [82]	WVD	ECG time-domain features, higher-order statistics, and pseudo-energy features	A decision tree-based classifier was used for the classification of arrhythmia. The total sensitivity and positive predictivity of 99.67% and 98.92% were achieved with the proposed method.
Abdeldayem and Bourlai (2018) [83]	STFT	Time-domain textured-based feature, time-frequency domain textured-based feature	The proposed method uses the ECG texture-based features in both temporal and spectro-temporal domains for the beat classification. These features were employed with a support vector machine (SVM) and k-nearest neighbor. Maximum classification accuracy of 96% was achieved in the SVM model.
Mateo and Talavera (2021) [84]	STFT with fixed window size	Wavelet power spectral density features: Median, variance, skewness, and kurtosis	The extracted features were used to develop a deep-learning model to detect atrial and ventricular premature contraction. The results showed an accuracy of 96.7%.
Le et al. (2021) [85]	STFT	Time-series features, spectrogram features, and spectrogram metadata features	The extracted features from the ECG signals were used as input for deep learning models: CNN and RCNN. The results showed a higher accuracy of 98% in the RCNN when the multimodal features were used.
Alqudah et al. (2021) [86]	STFT,	Log-frequency spectrogram, and mel frequency spectrogram	Different deep learning-based classifiers were compared to detect arrhythmia using different ECG spectrograms. An overall accuracy of 93.7% was achieved.
L.-M. Tseng and V. S. Tseng (2020) [87]	STFT and continuous wavelet transform (CWT)	Two-dimensional frequency domain feature	The current method uses the 2D-STFT/CWT and CNN to detect ventricular fibrillation (VF). An accuracy of 97% was achieved using the proposed method.
Hao et al. (2019) [88]	WT and STFT	Spectrogram	The spectrogram calculated using 1 s, 3 s, and 6 s ECG segments was used as input for the dense CNN to classify abnormal beats automatically.
Huang et al. (2019) [89]	STFT	Spectrogram	The ECG beats were transformed into 2D time-frequency spectrographic images and then used as input for the CNN model to detect the arrhythmia. The results showed an average classification accuracy of 99%.

TABLE 3: Continued.

Author, year	Time-frequency method used	Feature used	Inference
Wang et al. (2021) [90]	CWT	CWT scalogram and RR interval features	The MIT-BIH arrhythmia database was used, and the features were computed from the ECG segments. The CNN model was used for classification purposes, and an accuracy of 98% was achieved.
Anwar et al. (2018) [91]	DWT	Teager energy operator, morphological features, and RR interval	The study used hybrid features, obtained from the ECG signal's ECG morphology, RR interval, and DWT coefficients. The set of features after dimensionality reduction was then employed in a neural network for classification. The result suggested an improved accuracy of more than 99% for both class-oriented and subject-oriented schemes.
Sinha and Das (2020) [92]	DWT	Nonlinear features, statistical features	The study introduced a DWT-based multistage feature selection and classification approach to classify different arrhythmia types. Using the integrated feature set, the SVM classifier achieved a maximum accuracy of 99.22%
Mahgoub et al. (2018) [93]	DWT	Energy features	The study used the energy distribution of the ECG signals from each DWT level to compare and classify the arrhythmia types. The algorithm showed an accuracy of >95%.
Mohanty et al. (2019) [94]	DWT	Temporal features, spectral features, and statistical features	The extracted features from the decomposed signals were ranked by their correlation attribute, and then the ranked features were employed as input for the decision tree classifier and SVM classifier. The decision tree classifier differentiates ventricular tachycardia and ventricular fibrillation with the highest accuracy of 99.23%.
Tuncer et al. (2019) [95]	DWT	1-Dimensional hexadecimal local pattern features	The proposed method achieved a maximum accuracy of 95% in classifying 17 different types of arrhythmias using the nearest neighbor classifier.
Usha Kumari et al. (2021) [96]	DWT	Wavelet features	The study uses an SVM classifier by employing the DWT features. Three different types of arrhythmias: normal sinus rhythm, cardiac arrhythmia, and congestive heart failure, were classified with a lower computation complexity. Maximum accuracy of 95.92% was achieved using the method.
Dalal and Ingale (2021) [97]	DWT	RR interval and statistical features	DWT features were extracted using the 10 s ECG signals. Three different classification methods: convolutional neural network, multilayered perceptron (MLP), and random forest, were used to detect five different types of cardiac arrhythmia automatically. A classification accuracy of 98.78% was achieved using the CNN model.

TABLE 3: Continued.

Author, year	Time-frequency method used	Feature used	Inference
Bera and Gupta (2019) [98]	DWT	Features using (DWT), deep autoencoder (DAE), and principal component analysis (PCA)	The extracted features were inputs for two different classifiers: SVM and KNN. Maximum average sensitivity and positive peak rate (PPR) of 99.9% were achieved in classifying six arrhythmia types.
Wang et al. (2020) [99]	WPD	Multivariate statistical features	The current study employed the wavelet packet transform and correlation function on the ECG signals to construct histograms. After that, multivariate statistical features were extracted and used as input for the ANN models. A maximum accuracy of 98.8% was achieved in detecting atrial fibrillation.
Wang et al. (2019) [100]	WPD	RR interval features, morphological features and statistical features	Three sets of features were extracted and fused, and then the dimensionality was reduced using the PCA method. The reduced feature set was then employed as the input for the random forest classifier. The proposed methods showed the highest accuracy of 99% in detecting the arrhythmia types.
Sharma et al. (2019) [101]	WPD	Entropy features and fractal dimension feature	Fuzzy entropy, Renyi entropy, and fractal-dimensional features were extracted from the wavelet decomposed ECG signals. These features were used as the input for the KNN classifier to classify five arrhythmia classes. The result showed the highest accuracy of 98%.
Qaisar et al. (2021) [102]	WPD	Subband features	The study proposed a frequency content-based subband coefficient selection method for arrhythmia detection. A set of machine learning classifiers were compared. The highest accuracy of 97% was achieved.
Wang et al. (2020) [103]	WPD	Statistical feature, morphological feature, RR interval feature, and entropy feature	WPD was used for the computation of wavelet packet entropy. The entropy feature and all other features were used as an integrated feature set and then employed as input for the CNN model to classify four arrhythmias. The result showed a maximum accuracy of 93.4% in classifying cardiac arrhythmia.
Altan et al. (2018) [104]	WPD	Morphological feature and higher-order statistical feature	The features were extracted from segmented short-term ECG signals. These features were used to classify five arrhythmias types using a multistage deep belief network classifier. A maximum accuracy of 94.15% has been achieved with the proposed method.
Mohanty et al. (2021) [105]	EMD	Temporal, spectral, and statistical features	The ECG signals were decomposed by the EMD method. IMFs were used for computing the features. A decision tree classifier and SVM model were used to detect VT/VF conditions. Maximum classification accuracy of 98.69% was achieved.

TABLE 3: Continued.

Author, year	Time-frequency method used	Feature used	Inference
Izci et al. (2018) [106]	EMD	Spectral features	Features extracted from the IMFs that contained high-frequency information were used as input to the classification model. Three classifiers, namely, SVM, naive Bayesian, and LDA, were used as classification models to differentiate six types of arrhythmias. A maximum accuracy of 87% was achieved using the proposed methods.
Mohapatra and Mohanty (2021) [107]	EMD	Average power and coefficient of dispersion	Six IMFs from each ECG signal were used for feature extraction. The CNN model was used for the classification of cardiac arrhythmia. An accuracy of 95.98% was achieved during the classification process.
Sahoo et al. (2020) [108]	EMD + VMD	RR interval features, EMD, and VMD features	A set of 15 features was extracted and ranked using a ranker search approach and applied to the SVM classifier. Five types of arrhythmias were classified using the proposed method, with the highest classification accuracy of 95.35%.
Sabut et al. (2021) [109]	WT + EMD + VMD	Spectral features, statistical features, and entropy features	In this study, three decomposition methods were used to decompose the ECG signals, namely, WT, EMD, and VMD. A set of features was then computed from each decomposed ECG signal. These features were then employed in the deep neural network (DNN) classifier. An accuracy of 99.2% has been achieved in detecting ventricular tachycardia (VT) and ventricular fibrillation (VF).
Kayikcioglu et al. (2020) [110]	Hilbert transform (HT)	Frequency distribution-based feature	The study was based on a four-class classification method that classified an ECG beat as healthy, depressed ST segment, elevated ST segment, or arrhythmic. The frequency distribution-based feature was extracted using the HT. These features were then employed as the input for the classification models, namely the KNN, SVM, and ensemble classifier. The KNN classifier showed a maximum accuracy of 94.23%.
Zhang et al. (2021) [111]	HT + WVD	2D time-frequency plots	The current study uses a hybrid time-frequency analysis that is based on HT and WVD. The process transforms a 1D ECG signal into 2D time-frequency plots. In the residual neural network (ResNet) classifier, these images were fed as input with a maximum accuracy of 99.75%.
Kumar et al. (2020) [112]	FDM	Statistical features	A list of statistical features was computed from the decomposed signal and employed in an SVM classifier. It classifies the normal and abnormal ECG with an accuracy of 99%

TABLE 3: Continued.

Author, year	Time-frequency method used	Feature used	Inference
Fatimah et al. (2021) [113]	FDM	Statistical and entropy features	The fourier intrinsic band functions (FIBFs) were first computed from the ECG signals using the FDM method. A set of features from the FIBFs were extracted, and then the significant features were identified using Kruskal–Wallis’s test. The selected features were then employed in a group of classifiers. An accuracy of more than 99% in detecting myocardial infarction was achieved using the kNN classifier
Jha and Kolekar (2020) [114]	TQWT	Approximate coefficients	The ECG beats were decomposed using a sixth-level tunable Q-wavelet transform, and 12 approximate features from the decomposed signal were computed. A maximum accuracy of 99% in detecting the arrhythmia was obtained using an SVM classifier and the extracted features.
Liu et al. (2019) [115]	TQWT	Time, frequency, nonlinear, and entropy features	The features were extracted from the decomposed ECG segments and then employed as input to five ML models. The kNN classifier showed improved accuracy of 86% when the dual QTWT features were used.
Zeng et al. (2020) [116]	TQWT + VMD + phase space reconstruction (PSR)	Euclidean distance-based features	The 12-lead ECG signal and the Frank lead were used to build a 4D cardiac vector. The TQWT method was used to decompose the cardiac vector, and then the predominant subbands from each decomposed signal were computed using the VMD method. The phase space reconstruction (PSR) was employed to extract nonlinear dynamics by calculating a set of euclidean distance-based features. These features were employed in a neural network, and a maximum accuracy of 97% was achieved in detecting the abnormal ECG signal.
Kar et al. (2020) [117]	DTCWT	—	The ECG signals were decomposed using the DTCWT method and then employed in a convolutional neural network. Overall classification accuracy of 99% in detecting cardiac arrhythmia diseases was achieved using the proposed method

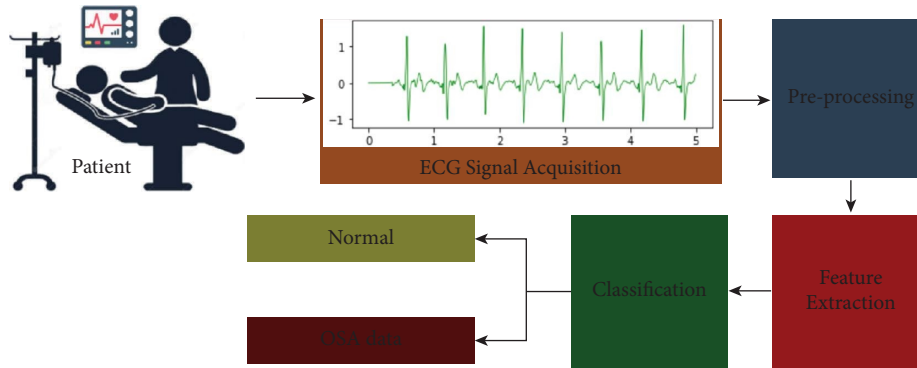


FIGURE 12: Steps in sleep apnea detection using an ECG signal (modified from [122]).

method of pattern recognition has been employed for easy, quick, and reliable identification. The ECG signals used for biometric authentication are either one-channel, two-channel, three-channel, or 12-channel. Among these, the single-lead ECG is the most common due to its simplicity. However, it is unclear whether simplicity leads to better performance; hence, in some of the studies, 12 lead ECG data has also been used.

The ECG biometric identification process follows three crucial steps: preprocessing, feature extraction, and classification. In [142, 143], the authors showed that ECG exhibits a unique and discriminatory pattern and can be categorized according to the classifier employed. However, it is essential to note that the performance of a classifier relies on feature extraction methods [144, 145], where the raw ECG signal is used to extract informative features. In general, the features extracted for the biometric methods can be divided into two broad categories: fiducial and nonfiducial [144]. The fiducial method uses the characteristics of the ECG waves, such as different peaks, waves, and intervals, whereas the nonfiducial method does not use these characteristics.

Several feature extraction methods have been explored in the past. Though there is no generalized rule for determining the significant boundaries of the waves that helps in efficient biometric identification [146], the nonfiducial-based method is preferable. It is the reason that no reference detection is needed in this method [147]. Some examples of the most widely used nonfiducial methods include autocorrelation coefficients [148], wavelet coefficients [149], principal components [150], and time-frequency decomposition methods [151]. In this section, the application of time-frequency decomposition methods in biometric analysis has been discussed. Table 5 represents a recent publication that used different time-frequency decomposition methods for biometric identification. It is evident from the table that empirical mode decomposition (EMD), and discrete wavelet transform (DWT) are the two most widely used methods recently. Some researchers have also followed hybrid methods that combine two different time-frequency features or multiple features, including nonfiducial and fiducial features. The time-frequency method has used several classification methods, such as CNN, SVM, LDA, DT, and CNN. However, in most cases, the CNN model showed good performance compared to the other classifiers. The reason

can be most of the deep learning models generate their own representative features during training.

3.5. Other Applications

3.5.1. Emotion Detection. Emotion is the consistent and separated response to external or internal events. The human emotional state can be defined using eight basic emotions: pleasure, sadness, anger, joy, curiosity, fear, and surprise. All other emotions can be a mixture of these primary emotional states. It has been reported in the literature that physiological signals are affected mainly by emotion. Hence, it can be used to detect and classify emotional states. Several studies have used the ECG signal to detect emotional changes [162–165]. In the research of Dissanayake et al. (2019) [166], the authors used three ECG signal-based techniques and the EMD method to recognize the primary human emotions: anger, joy, sadness, and pleasure. They achieved an accuracy gain of 6.8% as compared to the other methods. Another study employed a wavelet-based approach to obtain features at different time scales [167]. The proposed method showed an accuracy of 88.8% in detecting the valence state and 90.2% in detecting the arousal state, respectively. Chettupuzhakkaran and Sindhu (2018) have performed a comparative analysis in different time-frequency methods to detect happy and sad emotions. The authors reported a higher accuracy in DWT's case than in other methods (EMD, HHT, etc.) [168]. Wavelet transform and second-order difference plots were used in [169] to differentiate two emotional states: rest and fear, with a maximum accuracy of 80.24% using an SVM classifier.

3.5.2. Epileptic Seizures Detection. A seizure can be represented as an abrupt electrical disturbance in the brain activity that leads to a change in behavior, movement, and level of consciousness. Also, the onset of seizures affects autonomic nervous system activities. The literature suggests a significant difference in the physiological signals such as ECG and EEG has been observed during a seizure episode. The EEG signals have been used as a potential biomarker for seizure detection. However, significant ECG morphological changes have also been observed during a seizure episode. A shortened QT interval, ST-segment elevation, and T-wave inversion are typical changes in the ECG morphology

TABLE 4: List of published papers in the last five years that have used the time-frequency methods for sleep apnea detection.

Author	Time-frequency method used	Feature used	Inference from the study
Rohan and Kumari (2021) [125]	DWT	Statistical and entropy features	The ECG signals were decomposed up to the 7-level with the DWT method. A set of features were extracted from each decomposed signal. Five types of sleep apnea: normal, obstructive apnea, hypopnea with arousal, apnea with arousal, and central apnea with arousal, were classified using a decision tree classifier. The result showed an accuracy of 98.53% using the proposed method.
Gangan and Sahare (2018) [126]	DWT	Statistical features, ECG-derived respiration (EDR) feature	A number of statistical and EDR features were extracted from the single-lead ECG signal. Herein, the DWT and PCA were used to calculate the EDR feature. The SVM classifier was used to differentiate the normal and diseased samples, and the result showed an accuracy of 40.8%
Zarei et al. (2019)	DWT	Entropy features and nonlinear features	Features extracted from the DWT coefficients of the ECG signals were applied to the SVM classifier. Before classification, a feature selection method called the sequential forward feature selection algorithm was used. Using the selected features, the SVM classifier showed an accuracy of 94.63% in detecting sleep apnea.
Rajesh et al. (2021) [127]	DWT	Power spectrum density feature, waveform complexity, and higher-order moments	Three features were extracted from the ECG subbands obtained after employing the DWT method. The optimum feature set for the classifier was chosen using the particle swarm optimization method. Then the selected features were applied as input to a set of classifiers: SVM, LDA, k-nearest neighbor, and RF. A maximum accuracy of 90% was achieved using the RF classifier.
Suraj et al. (2018) [128]	DWT	Statistical features and entropy features	The study uses the DWT method to diagnose sleep apnea and congestive heart failure. Statistical and entropy features were extracted from the ECG subbands and fed to various ML classifiers. The tree-based classifier showed a maximum accuracy of 100% in differentiating the two data groups.
Chattopadhyay et al. (2018) [129]	DWT	Histogram and kurtosis-based feature	The proposed method used the DWT-based kurtosis and histogram analysis of ECG signals to detect sleep apnea. A significant difference in the kurtosis coefficient of the apnea patient compared to the normal volunteer was found.
Kumari et al. (2021) [130]	DWT	Statistical features	A set of statistical features were extracted from the DWT coefficients of the ECG signal and were employed in various ML classifiers (NB, SVM, and DT). Maximum accuracy of 98.07% was achieved using the DT classifier.

TABLE 4: Continued.

Author	Time-frequency method used	Feature used	Inference from the study
Al-Abed et al. (2021) [131]	STFT	Morphological features and spectrogram feature	STFT was used to compute the spectrogram of the QT interval, T-wave, and ST segment. The results obtained from the spectrogram analysis suggest a significant difference in specific frequency bands between the apneic ECG and normal ECG signals.
Niroshana et al. (2021) [132]	WVD	Scalogram, spectrogram, and WVD features	The current study used a novel fused image-based technique (scalogram, spectrogram, and WVD) and the CNN model for sleep apnea detection. The model showed a classification accuracy of 92.4%.
Dhok et al. (2020) [133]	WVD	Entropy feature and WVD feature	The current study uses the WVD and entropy features to detect two types of sleep apnea. The SVM classifier was used for the classification, and a maximum of 87.45% was achieved.
Singh et al. (2020) [134]	HT	Statistical feature	The study uses heartbeat interval (HBI) and ECG-derived respiration (EDR) data to classify normal and sleep apnea ECG data. The HBI and EDR data were converted to a reconstruction component using the HT, from which the statistical features were computed. These features were used as input to the stack autoencoder-based deep neural network and SVM model that showed a maximum accuracy of 94.3% during classification
Smruthy and Suchetha [135] (2018)	EMD	Morphological and statistical features	The morphological and statistical features were extracted from the IMFs and were used to classify normal and sleep apnea signals using the SVM classifier. An accuracy of 93.33% was achieved during the process.
Sundaram et al. (2018) [136]	EMD	IMF complexity index	The IMF complexity index was used to differentiate the normal sinus rhythm and sleep apnea data. The statistical comparison of the two data sets suggests a significant difference in the IMF index between the sleep apnea and sinus rhythm data.
Mashrur et al. (2021) [137]	EMD + CWT	Scalogram images	The most informative IMFs of the ECG signals were first identified, and the CWT method was used to determine the scalogram. Then, these scalogram plots were fed into the CNN model to classify normal and sleep apnea data. A classification accuracy of 94.30% was achieved using the proposed method.
Fatimah et al. (2020) [121]	FDM	Mean absolute deviation and entropy	1 min ECG segments were considered for the identification of the apnea events. The segments were decomposed using FDM, and then statistical and entropy features were extracted. These features were used as input to the machine learning model, and a maximum accuracy of 92.5% was reported using the SVM classifier.

TABLE 5: List of published papers in the last five years that have used the time-frequency methods for biometric identification.

Author	Time-frequency method	Feature	Inference
Abdeldayem and Bourlai (2018) [152]	STFT + CWT	Spectro-temporal images	The spectro-temporal dynamic images of the ECG signals were taken using the STFT and CWT methods. The method converted a 1D ECG signal into a 2D image, and was then used as input to the CNN network. An identification rate of 97.86% was achieved using the proposed method.
Biran and Jeremic (2020) [153]	STFT	Frechet mean distance	First, the study employs an STFT method to convert a 1D ECG signal to a 2D image. The Frechet mean distance was used to find the similarity between the STFT of different individuals. The result showed an accuracy of 96.45%.
Hammad et al. (2018) [154]	STFT		The STFT method has been used to extract the spectrogram images from the 1D ECG signals. A feature template using the CNN model was generated and then fed to the SVM classifier, and an accuracy of 98% was achieved.
Byeon et al. (2020) [141]	STFT	Spectrogram coefficients	The spectrogram of the ECG signals was computed using the STFT method. Then the spectrogram features were calculated and used as input to ensemble CNN, and a classification accuracy of 99% was achieved using the proposed model.
Bajare et al. (2019)	DWT	—	The study uses the ECG signals in three combinations (lead I, lead II, and combined leads). A set of features was computed from the DWT coefficients and then used as input to a 1D CNN model. The lead II ECG showed a higher biometric recognition accuracy of 96.93%.
Aziz et al. (2019) [155]	EMD	Statistical features and time-frequency features	The features were input into several classification algorithms: SVM, KNN, and DT for the subject identification. An accuracy of 98% was achieved using the SVM classifier.
Wang et al. (2019) [156]	DWT	Sparse autoencoder feature	The subbands of the QRS complex and P- and T-waves were selected using the DWT method. Then, the autoencoder feature set was generated from the chosen bands. A softmax classifier was used for the subject identification and showed an accuracy of 96%.
Khan et al. (2019) [157]	DWT	RR interval, DWT	The ECG signals were decomposed using EMD, and the 1 st two IMFs were selected. A set of time-frequency features were extracted and then used as input to the cubic SVM classifier for biometric detection. A classification accuracy of 98.4% was achieved with the proposed method.
Hadiyoso et al. (2019) [158]	EMD	Statistical feature and entropy feature	A set of statistical and entropy features were extracted from each IMFs of the ECG signal and then employed to LDA for the biometric identification. An accuracy of 93% was achieved in the study.
Hadiyoso et al. (2020) [159]	EEMD + VMD	Renyi entropy	EEMD and VMD methods decompose the ECG signals up to level 5. The Renyi entropy was calculated from each decomposed signal and then used as input to the cubic SVM. The proposed method showed an accuracy of 96.4% in biometric identification.

TABLE 5: Continued.

Author	Time-frequency method	Feature	Inference
Boostani et al. (2018) [160]	EMD + HT	Instantaneous frequency, phase, and amplitude, entropy feature	HT was employed in the selected IMFs, and a set of features was calculated. These features were then employed in a KNN classifier for classifying the individual features. A maximum accuracy of 95% was achieved using the proposed method.
Hadiyoso et al. (2020) [161]	VMD + EEMD	Statistical feature and entropy feature	The VMD and EEMD methods were used for the ECG decomposition. Statistical and entropy-based features were extracted from the decomposed signal and then used as input to an SVM classifier. The model achieved an accuracy of 98% for biometric identification

[170, 171]. Nevertheless, a few research studies found in the literature only uses ECG signals for seizure detection. Most papers have extracted the time-frequency features from the EEG signal or ECG and EEG signals [172–175]. But, in a recent study [176], Yang et al. found that the ECG signal was more efficient than the EEG signal in seizure detection. The authors used the spectrographic images of a short-duration ECG signal using the short-time Fourier transform (STFT). The images were used as the input to the CNN model for automatic seizure detection. Yet, more research based on the ECG-based features of epilepsy detection is needed in the future.

3.5.3. Driver Distraction Detection. Distracted driving is a severe concern for the safety of passengers and drivers. The three primary causes of distraction are taking the eye off the road, taking the hands off the steering, and a disturbed mind while driving. The secondary reasons may include conversations on the phone and active conversations with a passenger. Though social awareness and enhanced government rules have reduced the accident rate, the steps are insufficient. Hence, there is a need for real-time driver distraction detection. The ECG signal has shown potential application in real-time monitoring due to its properties: higher SNR, minimal implementation, easy to wear, and simple recording technology. Moreover, it does not show any latency issues compared to the camera-based detection system. The most crucial step in real-time ECG monitoring is the selection of features. Several time-frequency analysis methods have been reported in this regard. In [177], the authors have used the ECG subbands after decomposition using WPD. A set of WPD coefficients were selected, and three essential features, namely, power, mean, and standard deviation, were extracted from each coefficient. In the study, PCA was used as a dimensionality reduction method. The final feature set was used to classify the driver distraction using LDA and a quadratic discriminant analysis (QDA) classifier. In a similar study [178], the wavelet packet transform detected distraction during a phone call or conversation with a passenger. Dehzangi et al. (2018) have employed fused features extracted from the ECG signal [179]. It includes HRV parameters, spectro-temporal parameters, and power spectral density parameters. STFT was used for the spatiotemporal analysis. The optimal set of features was chosen using a feature selection method and various classifiers. The maximum detection accuracy of the driver distraction was 99.8%. Many studies have combined the ECG signal with other physiological signals such as EEG [180], EMG [181], and EOG.

3.5.4. Drug and Alcohol Detection. Early and timely drug overdose detection is crucial to maintaining health and avoiding major health problems. As per reports, nearly half of the emergency ward cases in the United States are due to drug-related overdose. It has been reported that most drugs influence cardiac functioning. The drug overdose may later lead to adverse cardiovascular events in many cases. Hence, the changes in the ECG signal can be a good indicator of this

drug overdose and can be used for its detection. Early research suggests changes in the ECG signal's morphological parameters after consuming various drugs (e.g., benzodiazepines, acetaminophen, and opioids). In their study, Manini et al. (2017) evaluated the effects of an acute drug overdose on the electrophysiological parameters. A prominent *R* peak and QT dispersion were detected after the drug overdose [182]. In a recent study [183], QT interval prolongation was observed due to the overdose of hydroxychloroquine in COVID patients [183]. Similar findings were reported in the case of other drugs also. Some of the drugs include antidysrhythmic (sotalol), antidepressants (escitalopram, bupropion, citalopram, trazodone, and so on), antipsychotics (haloperidol, quetiapine), sodium channel blockers (amitriptyline, doxepin, imipramine, diphenhydramine, and nortriptyline, and so on), and the antiemetic serotonin antagonist ondansetron [184]. Apart from drugs, alcohol also showed a similar effect on the heart [185]. Recently, a few researchers have attempted to use ECG signals for automatic drug detection. Pradhan and Pal (2020) have reported that it is possible to use time-domain statistical and entropy-based features extracted from the ECG signal to automatically detect the presence of a psychoactive drug, "caffeine," in the body [186]. In a recent study [187], the authors employed three different time-frequency methods, EMD, DWT, and WPD, to automatically detect the caffeinated coffee-induced short-term effect in the ECG signal. The application of ECG signals in seeing the impact of drugs and alcohol is new, and hence, a limited study is available in the literature. The exploration of joint-time frequency methods is insufficient and may be explored extensively in future research.

4. Limitations, Challenges, and Suggestions for Future Research

The main limitation of using the STFT method is that it does not show optimal time-frequency precision. Another disadvantage of the STFT method is that it is used primarily for short-duration ECG signal processing. However, short recordings are preferred during critical heart surgery to initiate the treatment process instead of investigating the longer-duration ECG signals [188]. In such cases, STFT-based signal processing has been proposed with definite success. Also, the STFT method is associated with varying spectral leakage due to applying different window functions. Another critical parameter while using the STFT method is choosing the correct window size. A limited time window shows a good time resolution but degrades the frequency resolution. Likewise, broader windows offer poor time resolution but a good frequency resolution. Hence, many employ more suitable techniques, such as the wavelet transform method (CWT, DWT, WPD, and so on). The wavelet transform can eliminate the problem of the fixed window size by using a varying window length and improving the time-frequency resolution [189]. However, it is unable to capture the edges of the signal adequately. Also, a trade-off exists amid WT's accuracy and computational complexity. Choosing a suitable mother wavelet in the WT is crucial as the accuracy of

a classification task is also affected by the choice of the mother wavelet.

The empirical mode decomposition (EMD) can overcome these limitations. EMD decomposes the signals into several IMF independent of the instantaneous frequency. The method delivers valuable data when little information about the underlying dynamic is available. However, careful application of the technique to any scientific research is required, as it lacks a proper theoretical background and is also associated with mode mixing [189]. Some extensions to the EMD method (including EEMD and VMD) were made to eliminate the disadvantages associated with EMD. VMD is more suitable for the analysis of nonstationary and nonlinear signals. The method shows a high operational efficiency and avoids information loss.

Several studies have implemented advanced time-frequency methods for analyzing and processing bio-potential signals, such as EMG and EEG. For example, the tunable Q-wavelet transform (TQWT), combined with time-frequency features, was used to detect epileptic seizures using the EEG signal [190]. A recent study used the TQWT method to differentiate seven hand movements using the surface-EMG signal [191]. Ahmed et al. (2022) employed the LSWA method and computed the differential entropy features from each EEG segment. The calculated features were then used as input in the CNN model to detect different emotional states [192]. In a recent study, the authors used the EWT and deep learning methods to detect coronavirus disease (COVID) [193]. Despite their diverse applications, these advanced time-frequency methods in ECG signal processing are limited. Hence, in the future, these methods may be employed more efficiently.

Real-time implementation of the time-frequency method in different ECG applications is another big challenge. Most of the available research is based on offline analysis that excludes noisy data. Many recent articles have employed physiological data to monitor epileptic seizures [194], dynamic changes in the brain [195], vigilance [196], sleep quality [197], fatigue [198], and abnormal driving [199]. These methods have primarily used either the brain or muscle signals. Therefore, the real-time implementations of the afore-discussed time-frequency methods in the ECG analysis may be explored in the future.

The current study has reviewed the application of various time-frequency decomposition methods for extracting ECG features. These features were then employed for various ECG-based applications, including arrhythmia detection, sleep apnea detection, biometric identification, noise elimination, and so on. A limitation of applying the feature extraction method is that the new features generated in the process are not always interpretable. Again, when there is a vast dataset, the conventional machine learning models do not perform satisfactorily due to the curse of dimensionality, which later needs feature selection methods. The deep learning models eliminate these issues as they can efficiently handle large datasets. Also, these models create their features, identify the correlated features, and then combine them to promote fast learning without providing explicit instruction. Though many studies have employed deep

learning models with the 2D-ECG data (spectrogram, scalogram, and so on) or the decomposed signals, the field demands extensive analysis. It may be explored in the future.

5. Conclusion

The current study provides a background idea about different time-frequency methods and their biomedical applications in ECG analysis. The study also discusses the recently published articles that have used these methods in various ECG applications. Though it is hard to include such a vast area in a single article, the present paper stresses the current status and recently published articles in the last five years. The following observations can be made based on the current review: DWT is recently the most widely used method, irrespective of its applications. The EMD and its variants are more suitable methods for noise elimination. The 2D-image-based methods such as spectrogram, scalogram, and frequency plots are most widely used with the deep learning models and report higher classification accuracy in arrhythmia detection. However, its use in other ECG-based applications is still limited and needs more attention. Also, the applications of some of the advanced time-frequency methods mentioned in this review demand more consideration in future research. The current review will form a reference and provide a comprehensive idea about applying the time-frequency methods in the ECG signal analysis. Some of the typical applications include detecting arrhythmia and sleep apnea. Also, some nonbiological applications include biometric identification, drug and alcohol detection, driver distraction, emotion detection, and so on. The facts discussed in this review will provide information about the current status of the time-frequency methods. The study will help future researchers to fill in the gaps and overcome the challenges in the said field. The knowledge shared in this review will benefit society by bringing more advanced technologies for disease detection, diagnostic applications, and other nonbiological applications in the future.

Data Availability

No data were used to support this study.

Conflicts of Interest

The authors declare that they have no conflicts of interest.

References

- [1] M. K. Gautam and V. K. Giri, "A neural network approach and wavelet analysis for ECG classification," in *Proceedings of the 2016 IEEE international conference on engineering and technology (ICETECH)*, pp. 1136–1141, IEEE, Coimbatore, India, March 2016.
- [2] H. Gholam-Hosseini and H. Nazeran, "Detection and extraction of the ECG signal parameters," in *Proceedings of the 20th Annual International Conference of the IEEE Engineering in Medicine and Biology Society. Vol. 20 Biomedical Engineering Towards the Year 2000 and Beyond (Cat. No.*

- 98CH36286), pp. 127–130, IEEE, Hong Kong, China, November 1998.
- [3] E. Ghaderpour, S. D. Pagiatakis, and Q. K. Hassan, “A survey on change detection and time series analysis with applications,” *Applied Sciences*, vol. 11, no. 13, 2021.
 - [4] S. Qian and D. Chen, “Joint time-frequency analysis,” *IEEE Signal Processing Magazine*, vol. 16, no. 2, pp. 52–67, 1999.
 - [5] H. Ocak, K. A. Loparo, and F. M. Discenzo, “Online tracking of bearing wear using wavelet packet decomposition and probabilistic modeling: a method for bearing prognostics,” *Journal of Sound and Vibration*, vol. 302, no. 4-5, pp. 951–961, 2007.
 - [6] N. J. Sairamya, M. J. Premkumar, S. T. George, and M. S. P. Subathra, “Performance evaluation of discrete wavelet transform, and wavelet packet decomposition for automated focal and generalized epileptic seizure detection,” *IETE Journal of Research*, vol. 67, no. 6, pp. 778–798, 2021.
 - [7] Z. F. M. Apandi, R. Ikeura, and S. Hayakawa, “Arrhythmia detection using MIT-BIH dataset: a review,” in *Proceedings of the 2018 International Conference on Computational Approach in Smart Systems Design and Applications (ICASSDA)*, pp. 1–5, IEEE, Kuching, Malaysia, August 2018.
 - [8] H. T. Wu, “Current state of nonlinear-type time–frequency analysis and applications to high-frequency biomedical signals,” *Current Opinion in Structural Biology*, vol. 23, pp. 8–21, 2020.
 - [9] H. Tirtom, M. Engin, and E. Z. Engin, “Enhancement of time-frequency properties of ECG for detecting micro-potentials by wavelet transform based method,” *Expert Systems with Applications*, vol. 34, no. 1, pp. 746–753, 2008.
 - [10] D. Gabor, “Theory of communication. Part 1: the analysis of information,” *Journal of the Institution of Electrical Engineers-Part III: Radio and Communication Engineering*, vol. 93, no. 26, pp. 429–441, 1946.
 - [11] P. Goupillaud, A. Grossmann, and J. Morlet, “Cycle-octave and related transforms in seismic signal analysis,” *Geo-exploration*, vol. 23, no. 1, pp. 85–102, 1984.
 - [12] Y. Meyer, *Wavelets and operators*, Cambridge university press, vol. 1, no. 37, Cambridge, UK, 1992.
 - [13] I. Daubechies, *Ten Lectures on Wavelets*, SIAM, Philadelphia, PA, USA, 1992.
 - [14] S. J. Hadi and M. Tombul, “Monthly streamflow forecasting using continuous wavelet and multi-gene genetic programming combination,” *Journal of Hydrology*, vol. 561, pp. 674–687, 2018.
 - [15] J. O. Stromberg, “A modified Franklin system and higher-order spline systems on \mathbb{R}^n as unconditional basis for Hardy spaces,” in *Proceedings of the Conference on Harmonic Analysis in Honor of Antoni Zygmund*, pp. 475–493, Chicago, IL, USA, April 1983.
 - [16] J.-O. Strömberg, “A modified Franklin system and higher-order spline systems on \mathbb{R}^n as unconditional bases for Hardy spaces,” in *Proceedings of the Conference on harmonic analysis in honor of Antoni Zygmund*, vol. 2, pp. 475–494, Wadsworth, OH, USA, January 1982.
 - [17] A. S. Al-Fahoum and A. A. Al-Fraihat, “Methods of EEG signal features extraction using linear analysis in frequency and time-frequency domains,” *International Scholarly Research Notices*, vol. 2014, Article ID 730218, 7 pages, 2014.
 - [18] C. E. Shannon, “A mathematical theory of communication,” *Bell System Technical Journal*, vol. 27, no. 3, pp. 379–423, 1948.
 - [19] A. V. Oppenheim, *Discrete-time Signal Processing*, Pearson Education India, India, 1999.
 - [20] E. P. Wigner, “On the quantum correction for thermodynamic equilibrium,” in *Part I: Physical Chemistry. Part II: Solid State Physics*, pp. 110–120, Springer, Berlin, Germany, 1997.
 - [21] M. Ralston, M. Rauch-Davies, K. Li-Chun, X. Hui-Ping, and Y. Di-Sheng, “General method to reduce cross-term interference in the Wigner-Ville Decomposition,” in *2007 SEG Annual Meeting OnePetro*, Richardson, TX, USA, 2007.
 - [22] Y. Dong and Y. Cui, “Analysis of a new joint time-frequency distribution of suppressing cross-term,” *Research Journal of Applied Sciences, Engineering and Technology*, vol. 4, pp. 1580–1584, 2012.
 - [23] H. Li, X. Deng, and H. Dai, “Structural damage detection using the combination method of EMD and wavelet analysis,” *Mechanical Systems and Signal Processing*, vol. 21, no. 1, pp. 298–306, 2007.
 - [24] Z. Peng, P. W. Tse, and F. Chu, “A comparison study of improved Hilbert–Huang transform and wavelet transform: application to fault diagnosis for rolling bearing,” *Mechanical Systems and Signal Processing*, vol. 19, no. 5, pp. 974–988, 2005.
 - [25] T. Wang, M. Zhang, Q. Yu, and H. Zhang, “Comparing the applications of EMD and EEMD on time–frequency analysis of seismic signal,” *Journal of Applied Geophysics*, vol. 83, pp. 29–34, 2012.
 - [26] P. Singh, S. D. Joshi, R. K. Patney, and K. Saha, “The Fourier decomposition method for nonlinear and non-stationary time series analysis,” *Proceedings of the Royal Society A: Mathematical, Physical and Engineering Sciences*, vol. 473, no. 2199, Article ID 20160871, 2017.
 - [27] E. Ghaderpour and S. D. Pagiatakis, “LSWAVE: a MATLAB software for the least-squares wavelet and cross-wavelet analyses,” *GPS Solutions*, vol. 23, no. 2, pp. 50–58, 2019.
 - [28] S. K. Khare, V. Bajaj, and G. R. Sinha, “Adaptive tunable Q wavelet transform-based emotion identification,” *IEEE Transactions on Instrumentation and Measurement*, vol. 69, no. 12, pp. 9609–9617, 2020.
 - [29] S. Asgari, A. Mehrnia, and M. Moussavi, “Automatic detection of atrial fibrillation using stationary wavelet transform and support vector machine,” *Computers in Biology and Medicine*, vol. 60, pp. 132–142, 2015.
 - [30] A. Bhattacharyya, M. Sharma, R. B. Pachori, P. Sircar, and U. R. Acharya, “A novel approach for automated detection of focal EEG signals using empirical wavelet transform,” *Neural Computing and Applications*, vol. 29, no. 8, pp. 47–57, 2018.
 - [31] M. Ghorat, G. B. Gharehpetian, H. Latifi, and M. A. Hejazi, “A new partial discharge signal denoising algorithm based on adaptive dual-tree complex wavelet transform,” *IEEE Transactions on Instrumentation and Measurement*, vol. 67, no. 10, pp. 2262–2272, 2018.
 - [32] Y. Hu, Q. Zhou, J. Gao, J. Li, and Y. Xu, “Compound fault diagnosis of rolling bearings based on improved tunable Q-factor wavelet transform,” *Measurement Science and Technology*, vol. 32, no. 10, Article ID 105018, 2021.
 - [33] J. M. Deng, H. Z. Yue, Z. Z. Zhuo, H. G. Yan, D. Liu, and H. Y. Li, “A stationary wavelet transform based approach to registration of planning CT and setup cone beam-CT images in radiotherapy,” *Journal of Medical Systems*, vol. 38, no. 5, pp. 40–49, 2014.
 - [34] W. Deng, S. Zhang, H. Zhao, and X. Yang, “A novel fault diagnosis method based on integrating empirical wavelet transform and fuzzy entropy for motor bearing,” *IEEE Access*, vol. 6, pp. 35042–35056, 2018.

- [35] U. B. D. Souza, J. P. L. Escola, and L. d. C. Brito, "A survey on Hilbert-Huang transform: evolution, challenges and solutions," *Digital Signal Processing*, vol. 120, Article ID 103292, 2022.
- [36] M. F. Isham, M. S. Leong, M. H. Lim, and Z. A. Ahmad, "Variational mode decomposition: mode determination method for rotating machinery diagnosis," *Journal of Vibroengineering*, vol. 20, no. 7, pp. 2604–2621, 2018.
- [37] Y. Wang, F. Liu, Z. Jiang, S. He, and Q. Mo, "Complex variational mode decomposition for signal processing applications," *Mechanical Systems and Signal Processing*, vol. 86, pp. 75–85, 2017.
- [38] J. S. Smith, "The local mean decomposition and its application to EEG perception data," *Journal of The Royal Society Interface*, vol. 2, no. 5, pp. 443–454, 2005.
- [39] Z. Wu and N. E. Huang, "Ensemble empirical mode decomposition: a noise-assisted data analysis method," *Advances in Adaptive Data Analysis*, vol. 1, no. 1, pp. 1–41, 2009.
- [40] Y. Yao, S. Sferra, C. Ibarra-Castanedo, R. You, and X. P. V. Maldague, "The multi-dimensional ensemble empirical mode decomposition (MEEMD)," *Journal of Thermal Analysis and Calorimetry*, vol. 128, no. 3, pp. 1841–1858, 2017.
- [41] D. Mandic, G. Souretis, W. Y. Leong, D. Looney, M. M. V. Hulle, and T. Tanaka, "Complex empirical mode decomposition for multichannel information fusion," in *Signal Processing Techniques for Knowledge Extraction and Information Fusion*, pp. 243–260, Springer, Berlin, Germany, 2008.
- [42] A. K. Mohammadi, R. Mohebian, and A. Moradzadeh, "HIGH-RESOLUTION seismic impedance inversion using improved ceemd with adaptive noise," *Journal of Seismic Exploration*, vol. 30, no. 5, pp. 481–504, 2021.
- [43] M. Barbosh, P. Singh, and A. Sadhu, "Empirical mode decomposition and its variants: a review with applications in structural health monitoring," *Smart Materials and Structures*, vol. 29, no. 9, Article ID 093001, 2020.
- [44] K. Brzostowski and J. Świątek, "Dictionary adaptation and variational mode decomposition for gyroscope signal enhancement," *Applied Intelligence*, vol. 51, no. 4, pp. 2312–2330, 2021.
- [45] G. J. Chen, L. Q. Zou, H. Y. Zhao, and Y. Q. Li, "An improved local mean decomposition method and its application for fault diagnosis of reciprocating compressor," *Journal of Vibroengineering*, vol. 18, no. 3, pp. 1474–1485, 2016.
- [46] A. R. Hassan, A. Subasi, and Y. Zhang, "Epilepsy seizure detection using complete ensemble empirical mode decomposition with adaptive noise," *Knowledge-Based Systems*, vol. 191, Article ID 105333, 2020.
- [47] R. Kumar, W. Zhao, and V. Singh, "Joint time-frequency analysis of seismic signals: a critical review," *Structural Durability and Health Monitoring*, vol. 12, no. 2, p. 65, 2018.
- [48] F. Ghembaza and A. Djebbari, "Epileptic seizure detection by quadratic time-frequency distributions of electroencephalogram signals," in *Proceedings of the 2019 International Conference on Advanced Electrical Engineering (ICAEE)*, pp. 1–6, IEEE, Algiers, Algeria, November 2019.
- [49] M. Dai and S. L. Lian, "Removal of baseline wander from dynamic electrocardiogram signals," in *Proceedings of the 2009 2nd international congress on image and signal processing*, pp. 1–4, IEEE, Tianjin, China, October 2009.
- [50] N. Sasirekha, P. V. Karthick, T. Premakumari, J. Harirajkumar, and S. Aishwarya, "Noise removal in ECG signal using digital filters," *European Journal of Molecular and Clinical Medicine*, vol. 7, no. 2, pp. 5145–5149, 2020.
- [51] N. Prashar, M. Sood, and S. Jain, "Design and implementation of a robust noise removal system in ECG signals using dual-tree complex wavelet transform," *Biomedical Signal Processing and Control*, vol. 63, Article ID 102212, 2021.
- [52] S. Chatterjee, R. S. Thakur, R. N. Yadav, L. Gupta, and D. K. Raghuvanshi, "Review of noise removal techniques in ECG signals," *IET Signal Processing*, vol. 14, no. 9, pp. 569–590, 2020.
- [53] A. Dikshit-Ratnaparkhi, D. Bormane, R. Ghongade, and R. Raut, "Performance analysis of symmetric uncertainty based optimal attribute generation algorithm for multiclass ECG in fuzzy rough domain," in *Proceedings of the 2019 6th International Conference on Computing for Sustainable Global Development (INDIACom)*, pp. 1303–1310, IEEE, New Delhi, India, March 2019.
- [54] L. El Bouny, M. Khalil, and A. Adib, "ECG signal denoising based on ensemble emd thresholding and higher order statistics," in *Proceedings of the 2017 International Conference on Advanced Technologies for Signal and Image Processing (ATSIP)*, pp. 1–6, IEEE, Fez, Morocco, May 2017.
- [55] S. Rachakonda and R. Mahesh, "Automated noise detection and classification for unsupervised ECG analysis systems using CEEMD and wavelet packet decomposition," in *Proceedings of the TENCON 2019-2019 IEEE Region 10 Conference (TENCON)*, pp. 373–377, IEEE, Kochi, India, October 2019.
- [56] J. X. Low and K. W. Choo, "IoT-enabled heart monitoring device with signal de-noising and segmentation using discrete wavelet transform," in *Proceedings of the 2018 15th International Conference on Control, Automation, Robotics and Vision (ICARCV)*, pp. 119–124, IEEE, Singapore, November 2018.
- [57] Á. Fehér, "Denoising ECG signals by applying discrete wavelet transform," in *Proceedings of the 2017 International Conference on Optimization of Electrical and Electronic Equipment (OPTIM) and 2017 Intl Aegean Conference on Electrical Machines and Power Electronics (ACEMP)*, pp. 863–868, IEEE, Brasov, Romania, May 2017.
- [58] P. M. Warriar, B. Manju, and R. P. Sreedharan, "A survey of pre-processing techniques using wavelets and empirical-mode decomposition on biomedical signals," in *Inventive Communication and Computational Technologies*, pp. 993–1002, Springer, Berlin, Germany, 2020.
- [59] R. Kapoor and R. Birok, "Genetic particle filter improved fuzzy-AEEMD for ECG signal de-noising," *Computer Methods in Biomechanics and Biomedical Engineering*, vol. 24, no. 13, pp. 1426–1436, 2021.
- [60] S. Thakran, "A hybrid GPFA-EEMD_Fuzzy threshold method for ECG signal de-noising," *Journal of Intelligent and Fuzzy Systems*, vol. 39, no. 5, pp. 1–10, 2020.
- [61] D. Zhang, S. Wang, F. Li et al., "An ECG signal de-noising approach based on wavelet energy and sub-band smoothing filter," *Applied Sciences*, vol. 9, no. 22, 2019.
- [62] H. Xiong, C. Zheng, J. Liu, and L. Song, "ECG signal in-band noise de-noising base on EMD," *Journal of Circuits, Systems, and Computers*, vol. 28, no. 1, Article ID 1950017, 2019.
- [63] D. Li, H. Zhang, and M. Zhang, "Wavelet de-noising and genetic algorithm-based least squares twin SVM for classification of arrhythmias," *Circuits, Systems, and Signal Processing*, vol. 36, no. 7, pp. 2828–2846, 2017.

- [64] S. Kumar, D. Panigrahy, and P. Sahu, "Denoising of Electrocardiogram (ECG) signal by using empirical mode decomposition (EMD) with non-local mean (NLM) technique," *Biocybernetics and Biomedical Engineering*, vol. 38, no. 2, pp. 297–312, 2018.
- [65] K. K. Patro, M. J. M. Rao, A. Jadav, and P. R. Kumar, "Noise removal in long-term ECG signals using EMD-based threshold method," in *Data Engineering and Communication Technology*, pp. 461–469, Springer, Berlin, Germany, 2021.
- [66] R. N. Vargas and A. C. P. Veiga, "Empirical mode decomposition, viterbi and wavelets applied to electrocardiogram noise removal," *Circuits, Systems, and Signal Processing*, vol. 40, no. 2, pp. 691–718, 2021.
- [67] A. K. Dwivedi, H. Ranjan, A. Menon, and P. Periasamy, "Noise reduction in ECG signal using combined ensemble empirical mode decomposition method with stationary wavelet transform," *Circuits, Systems, and Signal Processing*, vol. 40, no. 2, pp. 827–844, 2021.
- [68] Z. A. A. Alyasseri, A. T. Khader, M. A. Al-Betar, and M. A. Awadallah, "Hybridizing β -hill climbing with wavelet transform for denoising ECG signals," *Information Sciences*, vol. 429, pp. 229–246, 2018.
- [69] D. D. Taralunga, I. Gussi, and R. Strungaru, "Fetal ECG enhancement: adaptive power line interference cancellation based on Hilbert Huang Transform," *Biomedical Signal Processing and Control*, vol. 19, pp. 77–84, 2015.
- [70] A. Singhal, P. Singh, B. Fatimah, and R. B. Pachori, "An efficient removal of power-line interference and baseline wander from ECG signals by employing Fourier decomposition technique," *Biomedical Signal Processing and Control*, vol. 57, Article ID 101741, 2020.
- [71] S. A. Malik, S. A. Parah, and G. Bhat, "Electrocardiogram (ECG) denoising method utilizing Empirical Mode Decomposition (EMD) with SWT and a Mean based filter," in *Proceedings of the 2021 2nd International Conference on Intelligent Engineering and Management (ICIEEM)*, pp. 322–326, IEEE, London, UK, April 2021.
- [72] A. Kumar, H. Tomar, V. K. Mehla, R. Komaragiri, and M. Kumar, "Stationary wavelet transform based ECG signal denoising method," *ISA Transactions*, vol. 114, pp. 251–262, 2021.
- [73] P. G. Malghan and M. Kumar Hota, "Grasshopper optimization algorithm based improved variational mode decomposition technique for muscle artifact removal in ECG using dynamic time warping," *Biomedical Signal Processing and Control*, vol. 73, Article ID 103437, 2022.
- [74] S.-H. Liu, L.-T. Hsu, C.-H. Hsieh, and Y.-F. Huang, "Denoising of ecg signal with power line and emg interference based on ensemble empirical mode decomposition," in *Proceedings of the International Conference on Intelligent Information Hiding and Multimedia Signal Processing*, pp. 175–182, Springer, Berlin, Germany, November 2018.
- [75] W. Mohguen and S. Bouguezel, "Denoising the ECG signal using ensemble empirical mode decomposition," *Engineering, Technology and Applied Science Research*, vol. 11, no. 5, pp. 7536–7541, 2021.
- [76] S. A. Malik, S. A. Parah, and B. A. Malik, "Power line noise and baseline wander removal from ECG signals using empirical mode decomposition and lifting wavelet transform technique," *Health Technology*, vol. 12, no. 4, pp. 745–756, 2022.
- [77] S. Sanamdikar, S. Hamde, and V. Asutkar, "A literature review on arrhythmia analysis of ECG signal," *International Research Journal of Engineering and Technology*, vol. 2, no. 3, pp. 307–312, 2015.
- [78] A. Rizwan, P. Priyanga, E. H. Abualsauod, S. N. Zafrullah, S. H. Serbaya, and A. Halifa, "A machine learning approach for the detection of QRS complexes in electrocardiogram (ECG) using discrete wavelet transform (DWT) algorithm," *Computational Intelligence and Neuroscience*, vol. 2022, Article ID 9023478, 8 pages, 2022.
- [79] F. A. Elhaj, N. Salim, A. R. Harris, T. T. Swee, and T. Ahmed, "Arrhythmia recognition and classification using combined linear and nonlinear features of ECG signals," *Computer Methods and Programs in Biomedicine*, vol. 127, pp. 52–63, 2016.
- [80] V. Gupta, M. Mittal, and V. Mittal, "Chaos theory: an emerging tool for arrhythmia detection," *Sensing and Imaging*, vol. 21, no. 1, pp. 10–22, 2020.
- [81] M. S. Haleem, R. Castaldo, S. M. Pagliara et al., "Time adaptive ECG driven cardiovascular disease detector," *Biomedical Signal Processing and Control*, vol. 70, Article ID 102968, 2021.
- [82] S. Sultan Qurraie and R. Ghorbani Afkhami, "ECG arrhythmia classification using time frequency distribution techniques," *Biomedical engineering letters*, vol. 7, no. 4, pp. 325–332, 2017.
- [83] S. S. Abdeldayem and T. Bourlai, "Automatically detecting arrhythmia-related irregular patterns using the temporal and spectro-temporal textures of ECG signals," in *Proceedings of the 2018 24th International Conference on Pattern Recognition (ICPR)*, pp. 2301–2307, IEEE, Beijing, China, August 2018.
- [84] C. Mateo and J. A. Talavera, "Analysis of atrial and ventricular premature contractions using the Short Time Fourier Transform with the window size fixed in the frequency domain," *Biomedical Signal Processing and Control*, vol. 69, Article ID 102835, 2021.
- [85] M. D. Le, V. S. Rathour, Q. S. Truong, Q. Mai, P. Brijesh, and N. Le, "Multi-module recurrent convolutional neural network with transformer encoder for ECG arrhythmia classification," in *Proceedings of the 2021 IEEE EMBS International Conference on Biomedical and Health Informatics (BHI)*, pp. 1–5, IEEE, Athens, Greece, July 2021.
- [86] A. M. Alqudah, S. Qazan, L. Al-Ebbini, H. Alquran, and I. A. Qasmieh, "ECG heartbeat arrhythmias classification: a comparison study between different types of spectrum representation and convolutional neural networks architectures," *Journal of Ambient Intelligence and Humanized Computing*, vol. 13, no. 10, pp. 4877–4907, 2021.
- [87] L.-M. Tseng and V. S. Tseng, "Predicting ventricular fibrillation through deep learning," *IEEE Access*, vol. 8, pp. 221886–221896, 2020.
- [88] C. Hao, S. Wibowo, M. Majmudar, and K. S. Rajput, "Spectro-temporal feature based multi-channel convolutional neural network for ecg beat classification," in *Proceedings of the 2019 41st Annual International Conference of the IEEE Engineering in Medicine and Biology Society (EMBC)*, pp. 5642–5645, IEEE, Berlin, Germany, July 2019.
- [89] J. Huang, B. Chen, B. Yao, and W. He, "ECG arrhythmia classification using STFT-based spectrogram and convolutional neural network," *IEEE Access*, vol. 7, pp. 92871–92880, 2019.
- [90] T. Wang, C. Lu, Y. Sun, M. Yang, C. Liu, and C. Ou, "Automatic ECG classification using continuous wavelet

- transform and convolutional neural network,” *Entropy*, vol. 23, no. 1, 2021.
- [91] S. M. Anwar, M. Gul, M. Majid, and M. Alnowami, “Arrhythmia classification of ECG signals using hybrid features,” *Computational and Mathematical Methods in Medicine*, vol. 2018, Article ID 1380348, 8 pages, 2018.
- [92] N. Sinha and A. Das, “Automatic diagnosis of cardiac arrhythmias based on three stage feature fusion and classification model using DWT,” *Biomedical Signal Processing and Control*, vol. 62, Article ID 102066, 2020.
- [93] A. Mahgoub, A. Tanveer, and U. Qidwai, “Arrhythmia classification using DWT-coefficient energy ratios,” in *Proceedings of the 2018 IEEE-EMBS Conference on Biomedical Engineering and Sciences (IECBES)*, pp. 259–264, IEEE, Sarawak, Malaysia, December 2018.
- [94] M. Mohanty, P. Biswal, and S. Sabut, “Ventricular tachycardia and fibrillation detection using DWT and decision tree classifier,” *Journal of Mechanics in Medicine and Biology*, vol. 19, no. 3, Article ID 1950008, 2019.
- [95] T. Tuncer, S. Dogan, P. Plawiak, and U. Rajendra Acharya, “Automated arrhythmia detection using novel hexadecimal local pattern and multilevel wavelet transform with ECG signals,” *Knowledge-Based Systems*, vol. 186, Article ID 104923, 2019.
- [96] C. Usha Kumari, A. Sampath Dakshina Murthy, B. Lakshmi Prasanna, M. Pala Prasad Reddy, and A. Kumar Panigrahy, “An automated detection of heart arrhythmias using machine learning technique: SVM,” *Materials Today Proceedings*, vol. 45, pp. 1393–1398, 2021.
- [97] F. Dalal and V. V. Ingale, “Arrhythmia identification and classification using ensemble learning and convolutional neural network,” in *Proceedings of the 2021 2nd Global Conference for Advancement in Technology (GCAT)*, pp. 1–8, IEEE, Bangalore, India, October 2021.
- [98] P. Bera and R. Gupta, “Improved arrhythmia detection from electrocardiogram,” in *Proceedings of the 2019 IEEE Region 10 Symposium (TENSYP)*, pp. 547–552, IEEE, Kolkata, India, June 2019.
- [99] J. Wang, P. Wang, and S. Wang, “Automated detection of atrial fibrillation in ECG signals based on wavelet packet transform and correlation function of random process,” *Biomedical Signal Processing and Control*, vol. 55, Article ID 101662, 2020.
- [100] Z. Wang, H. Li, C. Han, S. Wang, and L. Shi, “Arrhythmia classification based on multiple features fusion and random forest using ECG,” *Journal of Medical Imaging and Health Informatics*, vol. 9, no. 8, pp. 1645–1654, 2019.
- [101] M. Sharma, R.-S. Tan, and U. R. Acharya, “Automated heartbeat classification and detection of arrhythmia using optimal orthogonal wavelet filters,” *Informatics in Medicine Unlocked*, vol. 16, Article ID 100221, 2019.
- [102] S. M. Qaisar, A. Mihoub, M. Krichen, and H. Nisar, “Multirate processing with selective subbands and machine learning for efficient arrhythmia classification,” *Sensors*, vol. 21, no. 4, 2021.
- [103] H. Wang, H. Shi, K. Lin et al., “A high-precision arrhythmia classification method based on dual fully connected neural network,” *Biomedical Signal Processing and Control*, vol. 58, Article ID 101874, 2020.
- [104] G. Altan, N. Allahverdi, and Y. Kutlu, “A multistage deep learning algorithm for detecting arrhythmia,” in *Proceedings of the 2018 1st international conference on computer applications and information security (ICCAIS)*, pp. 1–5, IEEE, Riyadh, Saudi Arabia, April 2018.
- [105] M. Mohanty, M. Dash, P. Biswal, and S. Sabut, “Classification of ventricular arrhythmias using empirical mode decomposition and machine learning algorithms,” *Progress in Artificial Intelligence*, vol. 10, no. 4, pp. 489–504, 2021.
- [106] E. Izci, M. A. Ozdemir, R. Sadighzadeh, and A. Akan, “Arrhythmia detection on ECG signals by using empirical mode decomposition,” in *Proceedings of the 2018 Medical Technologies National Congress (TIPTEKNO)*, pp. 1–4, IEEE, Magusa, Cyprus, November 2018.
- [107] S. K. Mohapatra and M. N. Mohanty, “Convolutional neural network based arrhythmia classification with selective features from empirical mode decomposition,” in *Proceedings of the Second International Conference on Information Management and Machine Intelligence*, pp. 375–383, Springer, Singapore, January 2021.
- [108] S. Sahoo, A. Subudhi, M. Dash, and S. Sabut, “Automatic classification of cardiac arrhythmias based on hybrid features and decision tree algorithm,” *International Journal of Automation and Computing*, vol. 17, no. 4, pp. 551–561, 2020.
- [109] S. Sabut, O. Pandey, B. S. P. Mishra, and M. Mohanty, “Detection of ventricular arrhythmia using hybrid time-frequency-based features and deep neural network,” *Physical and Engineering Sciences in Medicine*, vol. 44, no. 1, pp. 135–145, 2021.
- [110] I. Kayikcioglu, F. Akdeniz, C. Köse, and T. Kayikcioglu, “Time-frequency approach to ECG classification of myocardial infarction,” *Computers and Electrical Engineering*, vol. 84, Article ID 106621, 2020.
- [111] Y. Zhang, J. Li, S. Wei, F. Zhou, and D. Li, “Heartbeats classification using hybrid time-frequency analysis and transfer learning based on ResNet,” *IEEE Journal of Biomedical and Health Informatics*, vol. 25, no. 11, pp. 4175–4184, 2021.
- [112] A. Kumar, V. K. Mehla, H. Tomar, M. Kumar, and R. Komaragiri, “Classification of normal and abnormal ECG signals using support vector machine and Fourier decomposition method,” in *Proceedings of the 2020 IEEE International symposium on smart electronic systems (iSES)(Formerly iNiS)*, pp. 161–166, IEEE, Chennai, India, December 2020.
- [113] B. Fatimah, P. Singh, A. Singhal, D. Pramanick, S. Pranav, and R. B. Pachori, “Efficient detection of myocardial infarction from single lead ECG signal,” *Biomedical Signal Processing and Control*, vol. 68, Article ID 102678, 2021.
- [114] C. K. Jha and M. H. Kolekar, “Cardiac arrhythmia classification using tunable Q-wavelet transform based features and support vector machine classifier,” *Biomedical Signal Processing and Control*, vol. 59, Article ID 101875, 2020.
- [115] J. Liu, C. Zhang, T. Ristaniemi, and F. Cong, “Detection of myocardial infarction from multi-lead ECG using dual-Q tunable Q-factor wavelet transform,” in *Proceedings of the 2019 41st Annual International Conference of the IEEE Engineering in Medicine and Biology Society (EMBC)*, pp. 1496–1499, IEEE, Berlin, Germany, July 2019.
- [116] W. Zeng, J. Yuan, C. Yuan, Q. Wang, F. Liu, and Y. Wang, “Classification of myocardial infarction based on hybrid feature extraction and artificial intelligence tools by adopting tunable-Q wavelet transform (TQWT), variational mode decomposition (VMD) and neural networks,” *Artificial Intelligence in Medicine*, vol. 106, Article ID 101848, 2020.
- [117] N. Kar, B. Sahu, S. Sabut, and S. Sahoo, “Effective ECG beat classification and decision support system using dual-tree complex wavelet transform,” in *Advances in Intelligent*

- Computing and Communication*, pp. 366–374, Springer, Berlin, Germany, 2020.
- [118] I. Fehrzi, I. K. E. Purnama, and M. H. Purnomo, “Screening of non-overlapping apnea and non-apnea from single lead ECG-apnea recordings using time-frequency approach,” in *Proceedings of the 2019 International Conference on Computer Engineering, Network, and Intelligent Multimedia (CENIM)*, pp. 1–6, IEEE, Surabaya, Indonesia, November 2019.
- [119] H. Yue, Y. Lin, Y. Wu et al., “Deep learning for diagnosis and classification of obstructive sleep apnea: a nasal airflow-based multi-resolution residual network,” *Nature and Science of Sleep*, vol. 13, pp. 361–373, 2021.
- [120] A. V. Benjafield, N. T. Ayas, P. R. Eastwood et al., “Estimation of the global prevalence and burden of obstructive sleep apnoea: a literature-based analysis,” *The Lancet Respiratory Medicine*, vol. 7, no. 8, pp. 687–698, 2019.
- [121] B. Fatimah, P. Singh, A. Singhal, and R. B. Pachori, “Detection of apnea events from ECG segments using Fourier decomposition method,” *Biomedical Signal Processing and Control*, vol. 61, Article ID 102005, 2020.
- [122] A. Sheta, H. Turabieh, T. Thaher et al., “Diagnosis of obstructive sleep apnea from ECG signals using machine learning and deep learning classifiers,” *Applied Sciences*, vol. 11, no. 14, 2021.
- [123] J. Gubbi, A. Khandoker, and M. Palaniswami, “Classification of sleep apnea types using wavelet packet analysis of short-term ECG signals,” *Journal of Clinical Monitoring and Computing*, vol. 26, no. 1, pp. 1–11, 2012.
- [124] C. Avci, İ. Delibaşoğlu, and A. Akbaş, “Sleep apnea detection using wavelet analysis of ECG derived respiratory signal,” in *Proceedings of the 2012 International Conference on Biomedical Engineering (ICoBE)*, pp. 272–275, IEEE, Penang, Malaysia, February 2012.
- [125] R. Rohan and L. R. Kumari, “Classification of sleep apneas using decision tree classifier,” in *Proceedings of the 2021 5th International Conference on Intelligent Computing and Control Systems (ICICCS)*, pp. 1310–1316, IEEE, Madurai, India, May 2021.
- [126] G. E. Gangan and S. Sahare, “Derive respiratory signal form ECG using KPCA for application of sleep apnea detection,” in *Proceedings of the 2018 Second International Conference on Intelligent Computing and Control Systems (ICICCS)*, pp. 1511–1516, IEEE, Madurai, India, June 2018.
- [127] K. N. Rajesh, R. Dhuli, and T. S. Kumar, “Obstructive sleep apnea detection using discrete wavelet transform-based statistical features,” *Computers in Biology and Medicine*, vol. 130, Article ID 104199, 2021.
- [128] N. S. S. K. Suraj, V. Muppalla, V. Y. S. Reddy, and D. Suman, “Classification and diagnosis of sleep apnea and congestive heart failure using DWT based statistical features: an extensive study,” in *Proceedings of the 2018 15th IEEE India Council International Conference (INDICON)*, pp. 1–6, IEEE, Coimbatore, India, December 2018.
- [129] S. Chattopadhyay, G. Sarkar, and A. Das, “Sleep apnea diagnosis by DWT-based kurtosis, radar and histogram analysis of electrocardiogram,” *IETE Journal of Research*, vol. 66, no. 4, pp. 518–526, 2020.
- [130] L. R. Kumari, A. Lohitha, and N. Tarakeswar, “Detection of sleep apnea from ECG signal using various machine learning algorithms,” in *Proceedings of the 2021 IEEE 8th Uttar Pradesh Section International Conference on Electrical, Electronics and Computer Engineering (UPCON)*, pp. 1–7, IEEE, Dehradun, India, November 2021.
- [131] M. A. Al-abed, A. K. Al-Bashir, N. Obidat et al., “Spectral analysis of ECG ventricular waveform parameters in obese sleep apnea patients,” in *Proceedings of the 2021 IEEE Jordan International Joint Conference on Electrical Engineering and Information Technology (JEEIT)*, pp. 262–265, IEEE, Amman, Jordan, November 2021.
- [132] S. M. I. Niroshana, X. Zhu, K. Nakamura, and W. Chen, “A fused-image-based approach to detect obstructive sleep apnea using a single-lead ECG and a 2D convolutional neural network,” *PLoS One*, vol. 16, no. 4, 2021.
- [133] S. Dhok, V. Pimpalkhute, A. Chandurkar, A. A. Bhurane, M. Sharma, and U. R. Acharya, “Automated phase classification in cyclic alternating patterns in sleep stages using Wigner–Ville distribution based features,” *Computers in Biology and Medicine*, vol. 119, Article ID 103691, 2020.
- [134] H. Singh, R. K. Tripathy, and R. B. Pachori, “Detection of sleep apnea from heart beat interval and ECG derived respiration signals using sliding mode singular spectrum analysis,” *Digital Signal Processing*, vol. 104, Article ID 102796, 2020.
- [135] A. Smruthy and M. Suchetha, “An empirical mode decomposition-based method for feature extraction and classification of sleep apnea,” in *Computational Signal Processing and Analysis*, pp. 279–286, Springer, Berlin, Germany, 2018.
- [136] D. S. B. Sundaram, R. Balasubramani, S. Shivaram, A. Muthyala, and S. P. Arunachalam, “Single lead ECG discrimination between normal sinus rhythm and sleep apnea with intrinsic mode function complexity index using empirical mode decomposition,” in *Proceedings of the 2018 IEEE International Conference on Electro/Information Technology (EIT)*, pp. 0719–0722, IEEE, Rochester, MI, USA, May 2018.
- [137] F. R. Mashrur, M. S. Islam, D. K. Saha, S. R. Islam, and M. A. Moni, “SCNN: scalogram-based convolutional neural network to detect obstructive sleep apnea using single-lead electrocardiogram signals,” *Computers in Biology and Medicine*, vol. 134, Article ID 104532, 2021.
- [138] K. Wang, G. Yang, L. Yang, Y. Huang, and Y. Yin, “STERLING: towards effective ECG biometric recognition,” in *Proceedings of the 2021 IEEE International Joint Conference on Biometrics (IJCB)*, pp. 1–8, IEEE, Shenzhen, China, August 2021.
- [139] M. O. Diab, A. Seif, M. Sabbah, M. El-Abed, and N. Aloulou, “A review on ecg-based biometric authentication systems,” in *Hidden Biometrics*, pp. 17–44, Springer, Berlin, Germany, 2020.
- [140] T. N. Alotaiby, F. Aljabarti, G. Alotibi, and S. A. Alshebeili, “A nonfiducial PPG-based subject authentication approach using the statistical features of DWT-based filtered signals,” *Journal of Sensors*, vol. 2020, Article ID 8849845, 14 pages, 2020.
- [141] Y.-H. Byeon, S.-B. Pan, and K.-C. Kwak, “Ensemble deep learning models for ecg-based biometrics,” in *Proceedings of the 2020 Cybernetics and Informatics (K&I)*, pp. 1–5, IEEE, Velke Karlovice, Czech Republic, January 2020.
- [142] S.-C. Wu, P.-L. Hung, and A. L. Swindlehurst, “ECG biometric recognition: unlinkability, irreversibility, and security,” *IEEE Internet of Things Journal*, vol. 8, no. 1, pp. 487–500, 2021.
- [143] O. Boumbarov, Y. Velchev, and S. Sokolov, “ECG personal identification in subspaces using radial basis neural networks,” in *Proceedings of the 2009 IEEE international workshop on intelligent data acquisition and advanced*

- computing systems: technology and applications*, pp. 446–451, IEEE, Rende, Italy, September 2009.
- [144] Z. Hassan, S. Omer Gilani, and M. Jamil, “Review of fiducial and non-fiducial techniques of feature extraction in ECG based biometric systems,” *Indian Journal of Science and Technology*, vol. 9, no. 21, pp. 850–855, 2016.
- [145] M. A. Rahhal, Y. Bazi, H. AlHichri, N. Alajlan, F. Melgani, and R. R. Yager, “Deep learning approach for active classification of electrocardiogram signals,” *Information Sciences*, vol. 345, pp. 340–354, 2016.
- [146] A. D. C. Chan, M. M. Hamdy, A. Badre, and V. Badee, “Wavelet distance measure for person identification using electrocardiograms,” *IEEE Transactions on Instrumentation and Measurement*, vol. 57, no. 2, pp. 248–253, 2008.
- [147] Y.-T. Tsao, T.-W. Shen, T.-F. Ko, and T.-H. Lin, “The morphology of the electrocardiogram for evaluating ECG biometrics,” in *Proceedings of the 2007 9th International Conference on e-Health Networking, Application and Services*, pp. 233–235, IEEE, Taipei, Taiwan, June 2007.
- [148] Y. Wang, F. Agrafioti, D. Hatzinakos, and K. N. Plataniotis, “Analysis of human electrocardiogram for biometric recognition,” *EURASIP Journal on Applied Signal Processing*, vol. 2008, Article ID 148658, 11 pages, 2008.
- [149] M. M. Tantawi, K. Revett, A.-B. Salem, and M. F. Tolba, “A wavelet feature extraction method for electrocardiogram (ECG)-based biometric recognition,” *Signal, Image and Video Processing*, vol. 9, no. 6, pp. 1271–1280, 2015.
- [150] S. Pal and M. Mitra, “Increasing the accuracy of ECG based biometric analysis by data modelling,” *Measurement*, vol. 45, no. 7, pp. 1927–1932, 2012.
- [151] Y.-H. Byeon and K.-C. Kwak, “Pre-configured deep convolutional neural networks with various time-frequency representations for biometrics from ECG signals,” *Applied Sciences*, vol. 9, no. 22, 2019.
- [152] S. S. Abdeldayem and T. Bourlai, “ECG-based human authentication using high-levels spectro-temporal signal features,” in *Proceedings of the 2018 IEEE international conference on big data (big data)*, pp. 4984–4993, IEEE, Seattle, WA, USA, December 2018.
- [153] A. Biran and A. Jeremic, “Non-segmented ECG bi-identification using short time fourier transform and fréchet mean distance,” in *Proceedings of the 2020 42nd Annual International Conference of the IEEE Engineering in Medicine and Biology Society (EMBC)*, pp. 5506–5509, IEEE, Montreal, Canada, July 2020.
- [154] M. Hammad, Y. Liu, and K. Wang, “Multimodal biometric authentication systems using convolution neural network based on different level fusion of ECG and fingerprint,” *IEEE Access*, vol. 7, pp. 26527–26542, 2019.
- [155] S. Aziz, M. U. Khan, Z. A. Choudhry, A. Aymin, and A. Usman, “ECG-based biometric authentication using empirical mode decomposition and support vector machines,” in *Proceedings of the 2019 IEEE 10th Annual Information Technology, Electronics and Mobile Communication Conference (IEMCON)*, pp. 0906–0912, IEEE, Vancouver, Canada, October 2019.
- [156] D. Wang, Y. Si, W. Yang, G. Zhang, and J. Li, “A novel electrocardiogram biometric identification method based on temporal-frequency autoencoding,” *Electronics*, vol. 8, no. 6, 2019.
- [157] M. U. Khan, S. Aziz, K. Iqtidar, A. Saud, and Z. Azhar, “Biometric authentication system based on electrocardiogram (ECG),” in *Proceedings of the 2019 13th International Conference on Mathematics, Actuarial Science, Computer Science and Statistics (MACS)*, pp. 1–6, IEEE, Karachi, Pakistan, December 2019.
- [158] S. Hadiyoso, A. Rizal, and S. Aulia, “ECG based person authentication using empirical mode decomposition and discriminant analysis,” *Journal of Physics: Conference Series*, vol. 1367, no. 1, Article ID 012014, 2019.
- [159] S. Hadiyoso, I. Wijayanto, and E. M. Dewi, “ECG based biometric identification system using EEMD, VMD and renyi entropy,” in *Proceedings of the 2020 8th International Conference on Information and Communication Technology (ICoICT)*, pp. 1–5, IEEE, Yogyakarta, Indonesia, June 2020.
- [160] R. Boostani, M. Sabeti, S. Omranian, and S. Kouchaki, “ECG-based personal identification using empirical mode decomposition and Hilbert transform,” *Iranian Journal of Science and Technology, Transactions of Electrical Engineering*, vol. 43, no. 1, pp. 67–75, 2019.
- [161] S. Hadiyoso, I. Wijayanto, A. Rizal, and S. Aulia, “Biometric systems based on ecg using ensemble empirical mode decomposition and variational mode decomposition,” *Journal of Applied Engineering Science*, vol. 18, no. 2, pp. 181–191, 2020.
- [162] P. Sarkar and A. Etemad, “Self-supervised ecg representation learning for emotion recognition,” *IEEE Transactions on Affective Computing*, vol. 13, no. 3, pp. 1541–1554, 2022.
- [163] J. Domínguez-Jiménez, K. Campo-Landines, J. Martínez-Santos, and S. Contreras-Ortiz, “Emotion detection through biomedical signals: a pilot study,” vol. 10975, pp. 40–49, in *Proceedings of the 14th International Symposium on Medical Information Processing and Analysis*, vol. 10975, pp. 40–49, SPIE, Mazatlán, Mexico, December 2018.
- [164] H. Ferdinando, T. Seppänen, and E. Alasaarela, “Emotion recognition using neighborhood components analysis and ECG/HRV-based features,” in *Proceedings of the International Conference on Pattern Recognition Applications and Methods*, pp. 99–113, Springer, Berlin, Germany, June 2017.
- [165] Z. Cheng, L. Shu, J. Xie, and C. P. Chen, “A novel ECG-based real-time detection method of negative emotions in wearable applications,” in *Proceedings of the 2017 International Conference on Security, Pattern Analysis, and Cybernetics (SPAC)*, pp. 296–301, IEEE, Shenzhen, China, December 2017.
- [166] T. Dissanayake, Y. Rajapaksha, R. Ragel, and I. Nawinne, “An ensemble learning approach for electrocardiogram sensor based human emotion recognition,” *Sensors*, vol. 19, no. 20, 2019.
- [167] A. Sepúlveda, F. Castillo, C. Palma, and M. Rodríguez-Fernandez, “Emotion recognition from ecg signals using wavelet scattering and machine learning,” *Applied Sciences*, vol. 11, no. 11, 2021.
- [168] P. Chettupuzhakkaran and N. Sindhu, “Emotion recognition from physiological signals using time-frequency analysis methods,” in *Proceedings of the 2018 International Conference on Emerging Trends and Innovations In Engineering And Technological Research (ICETIETR)*, pp. 1–5, IEEE, Ernakulam, India, July 2018.
- [169] A. Goshvarpour and A. Abbasi, “An emotion recognition approach based on wavelet transform and second-order difference plot of ECG,” *Journal of AI and Data Mining*, vol. 5, no. 2, pp. 211–221, 2017.
- [170] R. Surges, C. A. Scott, and M. C. Walker, “Enhanced QT shortening and persistent tachycardia after generalized seizures,” *Neurology*, vol. 74, no. 5, pp. 421–426, 2010.

- [171] M. Zijlmans, D. Flanagan, and J. Gotman, "Heart rate changes and ECG abnormalities during epileptic seizures: prevalence and definition of an objective clinical sign," *Epilepsia*, vol. 43, no. 8, pp. 847–854, 2002.
- [172] I. B. Slimen, L. Boubchir, Z. Mbarki, and H. Seddik, "EEG epileptic seizure detection and classification based on dual-tree complex wavelet transform and machine learning algorithms," *The Journal of Biomedical Research*, vol. 34, no. 3, p. 151, 2020.
- [173] F. Asharinda, M. Shamim Hossain, A. Thacham et al., "A forecasting tool for prediction of epileptic seizures using a machine learning approach," *Concurrency and Computation: Practice and Experience*, vol. 32, no. 1, 2020.
- [174] A. J. Almahdi, A. J. Yaseen, and A. F. Dakhil, "EEG signals analysis for epileptic seizure detection using DWT method with SVM and KNN classifiers," *Iraqi Journal of Science*, pp. 54–62, 2021.
- [175] A. Zarei and B. M. Asl, "Automatic seizure detection using orthogonal matching pursuit, discrete wavelet transform, and entropy based features of EEG signals," *Computers in Biology and Medicine*, vol. 131, Article ID 104250, 2021.
- [176] Y. Yang, N. D. Truong, C. Maher, A. Nikpour, and O. Kavehei, "A comparative study of AI systems for epileptic seizure recognition based on EEG or ECG," in *Proceedings of the 2021 43rd Annual International Conference of the IEEE Engineering in Medicine and Biology Society (EMBC)*, pp. 2191–2196, IEEE, Mexico, November 2021.
- [177] S. Deshmukh and O. Dehzangi, "Identification of real-time driver distraction using optimal subband detection powered by Wavelet Packet Transform," in *Proceedings of the 2017 IEEE 14th International Conference on Wearable and Implantable Body Sensor Networks (BSN)*, pp. 9–12, IEEE, Eindhoven, Netherlands, May 2017.
- [178] S. V. Deshmukh and O. Dehzangi, "ECG-based driver distraction identification using wavelet packet transform and discriminative kernel-based features," in *Proceedings of the 2017 IEEE International Conference on Smart Computing (SMARTCOMP)*, pp. 1–7, IEEE, Hong Kong, China, May 2017.
- [179] O. Dehzangi, V. Sahu, M. Taherisadr, and S. Galster, "Multi-modal system to detect on-the-road driver distraction," in *Proceedings of the 2018 21st International Conference on Intelligent Transportation Systems (ITSC)*, pp. 2191–2196, IEEE, Maui, HI, USA, November 2018.
- [180] D. Tran, H. Manh Do, W. Sheng, H. Bai, and G. Chowdhary, "Real-time detection of distracted driving based on deep learning," *IET Intelligent Transport Systems*, vol. 12, no. 10, pp. 1210–1219, 2018.
- [181] Y. Zhang, Y. Chen, and C. Gao, "Deep unsupervised multi-modal fusion network for detecting driver distraction," *Neurocomputing*, vol. 421, pp. 26–38, 2021.
- [182] A. F. Manini, A. P. Nair, R. Vedanthan, D. Vlahov, and R. S. Hoffman, "Validation of the prognostic utility of the electrocardiogram for acute drug overdose," *Journal of American Heart Association*, vol. 6, no. 2, 2017.
- [183] G. Aksel, M. M. Islam, T. Aslan, and S. E. Eroglu, "Prolongation of QT interval due to hydroxychloroquine overdose used in COVID-19 treatment," *Turkish journal of emergency medicine*, vol. 20, no. 3, 2020.
- [184] S. L. Campleman, J. Brent, A. F. Pizon, J. Shulman, P. Wax, and A. F. Manini, "Drug-specific risk of severe QT prolongation following acute drug overdose," *Clinical Toxicology*, vol. 58, no. 12, pp. 1326–1334, 2020.
- [185] H. Raheja, V. Namana, K. Chopra et al., "Electrocardiogram changes with acute alcohol intoxication: a systematic review," *The Open Cardiovascular Medicine Journal*, vol. 12, pp. 1–6, 2018.
- [186] B. K. Pradhan and K. Pal, "Statistical and entropy-based features can efficiently detect the short-term effect of caffeinated coffee on the cardiac physiology," *Medical Hypotheses*, vol. 145, Article ID 110323, 2020.
- [187] B. K. Pradhan, M. Jarzębski, A. Gramza-Michałowska, and K. Pal, "Automated detection of caffeinated coffee-induced short-term effects on ECG signals using EMD, DWT, and WPD," *Nutrients*, vol. 14, no. 4, 2022.
- [188] J. Allen, "Short term spectral analysis, synthesis, and modification by discrete Fourier transform," *IEEE Transactions on Acoustics, Speech, and Signal Processing*, vol. 25, no. 3, pp. 235–238, 1977.
- [189] P. M. Tripathi, A. Kumar, R. Komaragiri, and M. Kumar, "A review on computational methods for denoising and detecting ECG signals to detect cardiovascular diseases," *Archives of Computational Methods in Engineering*, vol. 29, no. 3, pp. 1875–1914, 2021.
- [190] S. Pattnaik, N. Rout, and S. Sabut, "Machine learning approach for epileptic seizure detection using the tunable-Q wavelet transform based time–frequency features," *International Journal of Information Technology*, vol. 14, no. 7, pp. 3495–3505, 2022.
- [191] A. Subasi and S. M. Qaisar, "Surface EMG signal classification using TQWT, Bagging and Boosting for hand movement recognition," *Journal of Ambient Intelligence and Humanized Computing*, vol. 13, no. 7, pp. 3539–3554, 2020.
- [192] M. Z. I. Ahmed, N. Sinha, S. Phadikar, and E. Ghaderpour, "Automated feature extraction on AsMap for emotion classification using EEG," *Sensors*, vol. 22, no. 6, 2022.
- [193] P. Gaur, V. Malaviya, A. Gupta, G. Bhatia, R. B. Pachori, and D. Sharma, "COVID-19 disease identification from chest CT images using empirical wavelet transformation and transfer learning," *Biomedical Signal Processing and Control*, vol. 71, Article ID 103076, 2022.
- [194] S. Jukić, D. Kečo, and J. Kevrić, "Majority vote of ensemble machine learning methods for real-time epilepsy prediction applied on EEG pediatric data," *TEM Journal*, vol. 7, no. 2, 2018.
- [195] G. He, G. Lu, W. Shang, Z. Xie, and F. Xu, "A new statistical model for timely-detection of dynamical change in EEG signals," in *Proceedings of the 4th International Conference on Biometric Engineering and Applications*, pp. 1–6, Taiyuan, China, May 2021.
- [196] C. Zhou, B. Li, S. Li, and K. Huang, "Detection of vigilance in L3 autonomous driving based on EEG," in *Proceedings of the 2021 IEEE International Conference on Unmanned Systems (ICUS)*, pp. 359–365, IEEE, Beijing, China, October 2021.
- [197] I. Sadek and M. Mohktari, "Nonintrusive remote monitoring of sleep in home-based situation," *Journal of Medical Systems*, vol. 42, no. 4, pp. 64–10, 2018.
- [198] H. Alqahtani, *Deep Learning Approach to Real-Time Health Monitoring for Fatigue Damage Detection and Classification*, The Pennsylvania State University, Pennsylvania, PA, USA, 2021.
- [199] Y. Fan, F. Gu, J. Wang, J. Wang, K. Lu, and J. Niu, "Safe-Driving: an effective abnormal driving behavior detection system based on EMG signals," *IEEE Internet of Things Journal*, vol. 9, no. 14, pp. 12338–12350, 2022.

Research Article

A New Approach to Noninvasive-Prolonged Fatigue Identification Based on Surface EMG Time-Frequency and Wavelet Features

Fauzani N. Jamaluddin ¹, Fatimah Ibrahim ^{1,2,3} and Siti A. Ahmad ^{4,5}

¹Center for Innovation in Medical Engineering, Faculty of Engineering, Universiti Malaya, Kuala Lumpur 50603, Malaysia

²Department of Biomedical Engineering, Faculty of Engineering, Universiti Malaya, Kuala Lumpur 50603, Malaysia

³Center for Printable Electronics, Universiti Malaya, Kuala Lumpur 50603, Malaysia

⁴Department of Electrical and Electronics Engineering, Faculty of Engineering, Universiti Putra Malaysia, Serdang 43400, Selangor, Malaysia

⁵Malaysian Research Institute on Ageing, Universiti Putra Malaysia, Serdang 43400, Selangor, Malaysia

Correspondence should be addressed to Fatimah Ibrahim; fatimah@um.edu.my and Siti A. Ahmad; sanom@upm.edu.my

Received 22 December 2021; Revised 29 July 2022; Accepted 24 November 2022; Published 30 January 2023

Academic Editor: Kunal Pal

Copyright © 2023 Fauzani N. Jamaluddin et al. This is an open access article distributed under the Creative Commons Attribution License, which permits unrestricted use, distribution, and reproduction in any medium, provided the original work is properly cited.

In sports, fatigue management is vital as adequate rest builds strength and enhances performance, whereas inadequate rest exposes the body to prolonged fatigue (PF) or also known as overtraining. This paper presents PF identification and classification based on surface electromyography (EMG) signals. An experiment was performed on twenty participants to investigate the behaviour of surface EMG during the inception of PF. PF symptoms were induced in accord with a five-day Bruce Protocol treadmill test on four lower extremity muscles: the biceps femoris (BF), rectus femoris (RF), vastus medialis (VM), and vastus lateralis (VL). The results demonstrate that the experiment successfully induces soreness, unexplained lethargy, and performance decrement and also indicate that the progression of PF can be observed based on changes in frequency features (ΔF_{med} and ΔF_{mean}) and time features (ΔRMS and ΔMAV) of surface EMG. This study also demonstrates the ability of wavelet index features in PF identification. Using a naïve Bayes (NB) classifier exhibits the highest accuracy based on time and frequency features with 98% in distinguishing PF on RF, 94% on BF, 9% on VL, and 97% on VM. Thus, this study has positively indicated that surface EMG can be used in identifying the inception of PF. The implication of the findings is significant in sports to prevent a greater risk of PF.

1. Introduction

Surface electromyography (sEMG) is an electrical field of human skeletal musculature [1]. It is acquired by placing electrodes on the skin surface near the human muscle. The frequency and amplitude of the signals represent the behaviour and condition of the muscle's motor unit, conduction velocity, and ionic alteration of the muscle. Fatigue can be determined by the changes in its frequency content and amplitude either during an activity by analyzing every interval time length [2], at the beginning and ending of the activity [3, 4], or before and after the activity [5–8].

In fatigue detection, frequency shifting represents the changes in muscle fibre conduction velocities and

subsequent changes in the duration of the motor unit action potential waveform and fluctuations of muscle force and muscle fibre types as well as their decomposition [8, 9]. Most of the opinions agree that fatigue can be identified when its frequency shifts to a lower value to indicate that the muscle conduction velocities are slowing down [10, 11]. Other than frequency, fatigue can be detected through the amplitude of sEMG signals. The changes in the sEMG amplitude depend on the number of active motor units [12], discharge or firing rates, and the shape and propagation velocity of the intracellular action potential [10]. The amplitude of sEMG tends to increase during submaximal voluntary contraction (during motor unit recruitment) and decrease during maximal voluntary contraction [10, 13–16].

Other than time and frequency features, a new time-frequency feature representation to track fatigue was introduced and is known as the wavelet index (WI) method [17]. WI was introduced since it is more suitable to deal with nonstationary signals such as sEMG [17]. There are five WI features introduced by Malanda and Izquierdo, including the wavelet index ratio between moment -1 at scale 5 and moment 5 at scale 1 (WIRM1551), wavelet index of the ratio between moment -1 at the maximum energy scale and moment 5 at scale 1 (WIRM1M51), wavelet index of the ratio between moment -1 at scale 5 and moment 2 at scale 2 (WIRM1522), wavelet index of the ratio of energies at scale 5 and 1 (WIRE51), and wavelet index ratio between square waveform lengths at different scales (WIRW51). Through WI, the distribution shifting of sEMG energy can be assessed based on its scale and frequency band of decomposition.

In normal conditions, fatigue usually disappears by itself after a while. Recovering from fatigue indicates that biochemical reactions during sports activity are able to return to a normal level [18]. Under normal fatigue (NF) conditions, most opinions agree that the degree of fatigue begins with an increment in amplitude, followed by unchanged and decreased trends, as well as accompanied by a decrement in frequency centers. WI features tend to increase, indicating the distribution of energy shifting to a lower value under NF conditions.

However, high-intensity training activity will commonly lead to more biochemical reactions such as releasing of stress hormones (cortisol, epinephrine, and prolactin) [19, 20], glycogen depletion [21], and the existence of lactate [22]. Fatigue due to intense training will require a longer recovery period than normal physical activity. It is crucial for improvement and recuperation [23]. During the period, it will enable hormones to return to a normal level [18] and allow physiological adaptation to a cardiovascular and muscular system to provide a higher level of performance [24]. If the training load is imbalanced with an inadequate recovery period, fatigue can be continuous and accumulated. This situation leads to prolonged fatigue (PF). Under this condition, more biochemical or maladaptive hormonal responses may occur [24, 25]. The alteration in biochemicals, which leads to PF, can be signified by reduced performance, lethargy, soreness, insomnia, psychological disturbance, restlessness, hypertension, and increased incidence of injury [21, 26]. It commonly requires several days to a week to recover from [23, 27]. This condition needs to be treated accordingly to avoid a more severe condition, known as chronic fatigue syndrome. A report shows that about 20–60% of athletes, 60% of elite runners, and 33% of nonelite runners experienced chronic fatigue syndrome at least once in their career life [23, 26, 28].

In current practice, PF signs can be assessed invasively or noninvasively. Blood tests are invasive and used to investigate biochemical concentrations associated with PF such as lactate, glycogen depletion, creatine kinase, and iron levels [22, 28]. Meanwhile, muscle biopsies are utilized to evaluate the condition of the injured muscle and ionic concentration in the muscle layer. During the collection of muscle tissue, numbing medicine is required. Although both blood tests

and biopsies are reliable and accurate, they cause discomfort and are not suitable for frequent measurement. Furthermore, these methods are time-consuming, need to be analyzed in a laboratory environment, and require full supervision from an expert [29].

Due to the limitation of invasive methods, PF can also be traced through noninvasive diagnostic tools because the alteration in biochemicals can be observed physically. For example, glycogen depletion and lactate accumulation are commonly associated with a decline in performance, the oxidative stress increment leads to muscle pain, and cytokine leads to unexplained lethargy, decreased appetite, depression, and sleep disturbance [26, 28]. The commonly used noninvasive tools are interviews, athlete-coach monitoring approaches [18], questionnaires [26, 28], training logs [30], and perceived exertion ratings. The current practice requires more than one diagnostic tool to comprehensively screen off PF signs. Diagnostic tools such as interviews, training logs, and questionnaires often require close supervision by the practitioner and personal coach. Nevertheless, using many tools for the PF identification process is ineffective, particularly, in monitoring a large group of athletes because these tools are time-consuming and have many procedures. Even so, many agree that PF condition prevention is the best solution [26]. The reason is that the treatment of PF is time-consuming and cost-ineffective, depending on the degree of PF. Furthermore, PF signs endured are too risky for athletes.

Later, findings reveal that the center frequency shifting of sEMG to the upper value was attributed to the alteration of ionic concentrations such as lactate and glycogen and the existence of soreness following high-intensity exercise [6, 31]. This finding is opposed to the earlier findings that state a decrement in the center frequency of sEMG following short duration and light exercise refers to fatigue conditions. This situation demonstrates that duration, the intensity of exercise, biochemical reactions, and the existence of PF signs may affect the sEMG signal behaviour. This situation also demonstrates the potential of sEMG as a new tool which is noninvasive, comfortable, fast, easy to use, and quantifiable to detect signs of PF. The detection at the earliest stage helps prevent a more serious state of PF.

Therefore, this paper aims to investigate the ability of sEMG signals to identify the inception of PF in four muscles with different percentages of muscle activation. This paper also investigates the ability of wavelet index features in PF identification. The performance of the surface EMG features was evaluated by the naïve Bayes classification accuracy in predicting the PF condition.

2. Materials and Methods

2.1. Study Protocol. Twenty participants (age \pm standard deviation (SD): 24 ± 3 years old; body mass index: 22.7 ± 2 kg/m²) were recruited for this study. Participants were screened using a Physical Activeness Questionnaire (PAR-Q and You) (Supplementary Appendix S1) to rule out any pre-existing health contraindications and risk factors for exercise. The exclusion criteria were participants with diabetes, high blood pressure, heart disease, any chronic

disease, joint or bone problems, and taking any medication to control blood pressure and blood sugar. The approval, to conduct the experiment procedure, was obtained from the Ethical Committee, Universiti Putra Malaysia (UPM/TNCPI/RMC/1.4.18.1(JKEUPM)/F2).

The participants were given a written and verbal explanation, including the potential risks and discomfort that they might experience. The participants signed written informed consent before the experiment began. As a precaution, the participants were also protected by insurance (policy number: P809067176) during the whole experiment period.

2.2. Procedure. The experimental design was divided into two phases: Phase I was meant for familiarization and Phase II was for intensive training. Each participant had to take part in both phases. Phase I enabled the participants to familiarize themselves with the equipment and procedures, while Phase II was designed to induce PF signs. Between Phase I and Phase II, the participants were requested to rest and refrain from exercising or doing any heavy physical activity. Phase I was carried out on alternate days to avoid the emergence of PF, and Phase II was carried out on five consecutive days (see Supplementary Table S1. Schedule of Experiment).

The participants were instructed to refrain from any heavy physical exercise, alcohol, and caffeine consumption 24 hours before the running test in both phases. They also required taking meals two hours before the assessment to avoid lack of energy and dehydration. The experiment was conducted in accordance with the Bruce Protocol treadmill test (see Supplementary Table S2). In the protocol, the inclination and speed of the treadmill were increased every three minutes. The total duration of the protocol was 21 minutes. The participants were required to run for five consecutive days and requested to improve their performance daily. As individual fatigue response is highly variable, no specific distance and time duration were fixed [32].

2.3. Data Collection. In this study, training logs (see Supplementary Appendix S2) were used to record measurements before, during, and after the running activity. The measurements were used to monitor the daily performance and identify the emergence of PF conditions during Phase II of the experiment. The flowchart of the experiment procedure and measurements is shown in Supplementary Figure S1, and the equipment utilized throughout the experiment was the COSMED T170 treadmill, Polar chest strap heart rate monitor, Watsons blood pressure monitor, and custom-made surface EMG data collection tool (see Supplementary Figures S2(a) and S2(b) for the schematic circuit of surface EMG systems).

The recorded measurements during Phase II were as follows:

(a) Percentage of the maximal heart rate

Percentage of the maximal heart rate ($\%HR_{\max}$) is recorded to indicate running efforts performed by the participant. $\%HR_{\max}$ is determined as

$$\%HR_{\max} = \frac{HR_{\max}(\text{running}) \times 100}{(220 - \text{Age})}. \quad (1)$$

(b) Percentage of endurance time

Endurance time of running on the treadmill is calculated [33] based on the following equation:

$$\%T_{\text{endurance}} = \frac{T_{\text{recorded}} \times 100}{21 \text{ minutes}}. \quad (2)$$

(c) Prolonged fatigue sign identification

The participants were also requested to fill in a 24-hour training distress questionnaire (see Supplementary Appendix S3) daily [28]. The questionnaire was used to identify sleeping and psychological disturbance and muscle soreness. During the experiment, the participants were also interviewed before the running activity. The interview session was conducted to identify whether the participants experienced lethargy. After running, the participant requested to scale the running activity experiment to indicate the difficulty of the experiment. The emergence of PF signs was monitored based on noninvasive diagnostic tools, as summarized in Table 1.

The prolonged fatigue diagnosis was important as surface EMG signals were then grouped and classified based on PF signs experienced by the participants. Due to ethical reasons and potential risks endured by the participants, only symptoms developed within five days of the experiment were monitored. The earliest PF signs that appeared during the training were sufficient to indicate the emergence of PF. The participants were also reminded about two symptoms of fatigue. The symptoms were observed based on two conditions as follows:

(a) Fatigue symptom 1 (monitored before the running activity)

The participant was not allowed to run and was terminated from the experiment if any of the following fatigue symptoms were observed before the assessment:

- (i) Heart rate >100 bpm
 - (ii) Blood pressure >140/90
 - (iii) Showing performance decrements in the previous experiment
 - (iv) Psychology scores in the 24-hour training distress questionnaire >14 for at least three days
 - (v) Collapsing in the previous experiment
- (b) Fatigue symptom 2 (monitored during running activity)

The participant must stop running if the following symptoms are observed while running:

- (i) Lack of energy
- (ii) Feel dizzy
- (iii) Blurred vision

2.4. Surface Electromyography. SEMG signals were collected from the biceps femoris (BF), rectus femoris (RF), vastus lateralis (VL), and vastus medialis (VM). These muscles were

selected based on the activation muscles during running and suffer a high rate of injury in sports involving running [35, 36]. Running at 10° grade inclination activates $79 \pm 7\%$ of BF, $76 \pm 14\%$ of vastus, and $44 \pm 20\%$ of RF, and the activation is elevated as the inclination increases [36, 37]. The sEMG signals were collected using the custom-built sEMG acquisition system, as shown in Figure 1.

The sEMG system was designed based on an AD620 instrumentation amplifier system. AD620 was selected as it provides a 130 dB common-mode rejection ratio (CMRR), low power consumption, that is, 1.3 mA, and comprises a low input voltage noise of $9 \text{ nV}/\sqrt{\text{Hz}}$ at 1 kHz and $0.28 \mu\text{V}$ p-p in the 0.1 Hz–10 Hz band. The full system offers a signal-to-noise ratio (SNR) of 25 dB and gains an amplifier at 248. The 50 Hz notch filter is designed according to the following equation:

$$F_n = \frac{1}{2\pi RC}, \quad (3)$$

where $R = 68 \text{ k } \Omega$ and $C = 47 \text{ nF}$.

The schematic diagram of the sEMG data acquisition board is depicted in Supplementary Figures S2(a) and S2(b). The analog signals of surface EMG were digitized into 12 bits by using National Instrument Data Acquisition (NI-DAQ) 6008 with frequency sampling, F_s , at 1 kHz. 1 kHz was selected to avoid aliasing as suggested by De Luca. Then, the collected data were filtered using a digital finite impulse response (FIR), a high-pass filter (HPF), 301 taps, and a cutoff at 20 Hz. This HPF is essential for removing baseline wander during data acquisition. F_s and HPF specifications were set using data logger software, LabVIEW.

Ag/Ag Cl electrodes from Kendall MediTrace 200 were used to acquire the signals. Bipolar electrodes with 20 mm inner distance were attached to the involved muscles, and one reference electrode was placed at the knee of the participants. The electrodes were positioned at BF, RF, VL, and VM based on the Surface EMG for the Noninvasive Assessment of Muscles (SENIAM) standard [38]. The RF muscle was determined by 50% distance between the patella upper borders and the anterior iliac spine (AIS), VL was at 25% distance from Gerdy prominence to AIS, and VM was at 25% distance from the joint space to AIS. After measuring and marking the muscle, palpation of the involved muscle was carried out to ensure that the electrodes were placed correctly. During palpation, the participants were asked to flex and extend knee movements to activate the muscles, as shown in Supplementary Table S3 [38, 39].

In data collection, the participants were asked to move their legs to activate the observed muscles. Only one leg was involved in data collection, and it was observed that the participants were comfortable using the left leg in the study. The investigation on one leg was enough in this study to observe PF conditions based on surface EMG. RF, VL, and VM were activated when the hip was flexed, while the knee was extended to 180. As shown in Figure 2(a), the participants were asked to sit on a chair and were requested to move their legs from Point A to Point B to activate the quadriceps muscle group. They were asked to stay at each point for ten seconds and then repeat the movement three

times. It was discovered that the RF, VL, and VM muscles contracted when the leg was at Point B and were at rest when the leg was at point A, as suggested by Konrad.

Other than RF, VL, and VM, surface EMG signals were also collected from the BF muscle. The location of the electrodes for BF was at 50% distance from the lateral epicondyle of the tibia to the ischial tuberosity. To collect surface EMG signals from BF, the participants were asked to stand and move their legs from Point D to Point E, as shown in Figure 2(b). Before that, the participants needed to place one (1) of their legs one foot (1 ft) away from Point C, which was Point D. BF contracted when the hip was extended, while the knee flexed [34]. When the body gesture was about 30 forward, the knee flexed until the leg was lifted about 15 cm to Point E. This distance was chosen as it provides the maximum activation of BF during movement [40]. The participants were requested to move their legs from Point D to Point E three times at (10) seconds intervals. The sEMG signals were collected during before and after running activities. Figure 3 shows the example of sEMG signals when the knee is flexed and extended during the position and movement in Figures 2(a) and 2(b).

2.5. Feature Extraction. A nonoverlapping windowing technique was employed with samples $n = 5000$, as shown in Figure 4. The moment at which the muscles started to contract and relax was ignored because the dynamic movement during data collection might result in false information [41]. The number of n was selected because the authors of [2] have demonstrated that segmentation length is suitable for muscle fatigue identification. The features were extracted at each contraction and averaged.

Specific features were extracted based on the frequency, time, and wavelet index (WI). The spectral content of surface EMG was determined according to the Fourier transform, and the frequency parameter was quantified based on its median (F_{med}) in (4) and mean (F_{mean}) in (5):

$$F_{\text{med}} = \frac{1}{2} \sum_{j=1}^M P_j, \quad (4)$$

$$F_{\text{mean}} = \frac{\sum_{j=1}^M f_j P_j}{\sum_{j=1}^M P_j}, \quad (5)$$

where f_j = frequency of the spectrum at frequency bin j , P_j = EMG power spectrum at frequency bin j , and M = length of the frequency bin.

The time features can be quantified based on the mean absolute value (MAV) in (6) and the root mean square (RMS) [42] in (7) [42]:

$$\text{MAV} = \frac{1}{n} \sum_{j=1}^n |x_j|, \quad (6)$$

$$\text{RMS} = \sqrt{\frac{1}{n} \sum_{j=1}^n x_j^2}, \quad (7)$$

TABLE 1: Prolonged fatigue sign identification.

Tools	Prolonged fatigue signs	Identification
Training log	Performance decrement Restlessness Hypertension	Endurance time previous workout better HR > 100 before running BP > 140/90 before running
24-hour training distress questionnaire [28]	Sleeping disturbance Psychological disturbance Muscle soreness	The different time duration between before and during intensive training Psychological score >14 Soreness scale (scale 4: tender but not sore to scale, 7: very sore)
Interview	Unexplained lethargy	Feel lethargy before running
Borg Scale CR10 [34]	The difficulty level of exercise increases	Increasing of the scale

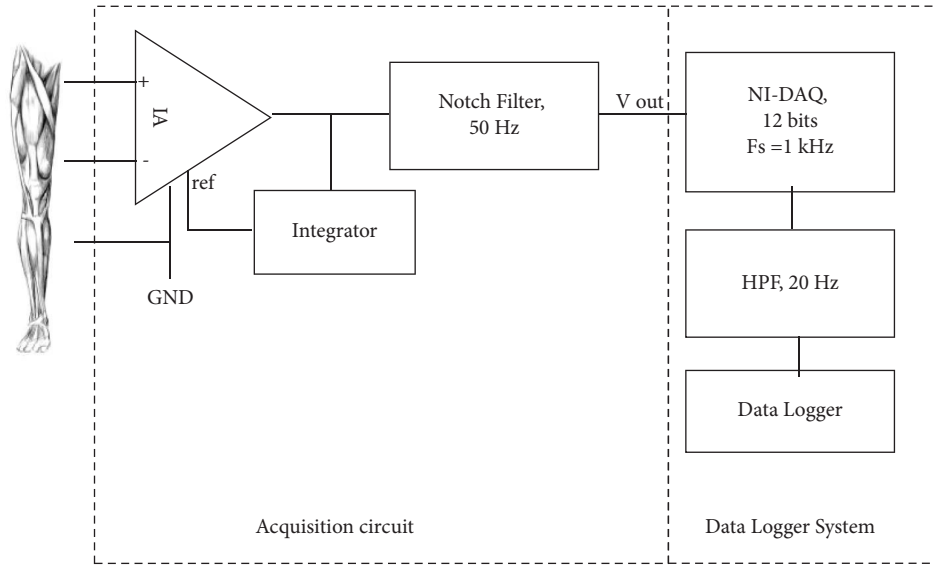


FIGURE 1: Block diagram of the sEMG data acquisition system.

where x = signals and n = number of samples [43].

This study also investigates the ability of WI features in PF [43] identification since it was never tested in determining fatigue under high-intensity conditions. WI features were used to evaluate the distribution shifting of sEMG energy based on its scale and frequency band decomposition. WI was calculated based on the discrete wavelet transform (DWT) which was decomposed into five levels by using symlet 5 (sym5) and Daubechies (db5) as the mother wavelet [17]. The decomposition process consisted of a series of filter banks, where at every i level of decomposition, the signal was filtered into half of the frequency band [44]. The low-pass filter produced an approximation coefficient, while the high-pass filter produced a detail coefficient (D_i) (scales). Figure 5 shows the five levels of sEMG decomposition details and the power spectra of decomposition details at scales 1–5 that are determined based on the Fourier transform.

The wavelet index ratios between moments at different scales were then determined based on the power spectrum of wavelet details, D_i .

The five WI features were tested as follows:

- (a) The WI ratio is between moment -1 at scale 5 and moment 5 at scale 1 (WIRM1551).

$$\text{WIRM1551} = \frac{\int_{f_1}^{f_2} f^{-1} D_5(f) \cdot df}{\int_{f_1}^{f_2} f^5 D_1(f) \cdot df}, \quad (8)$$

where $\psi(t)$ used was sym5, $f_1 = 10$ Hz and $f_2 = 500$ Hz, and $D_5(f)$ and $D_1(f)$ are the power spectra of the five and first scales of decomposition details [14].

- (b) The WI ratio is between moment -1 at the maximum energy scale and moment 5 at scale 1 (WIRM1M51).

$$\text{WIRM1M51} = \frac{\int_{f_1}^{f_2} f^{-1} D_{\max}(f) \cdot df}{\int_{f_1}^{f_2} f^5 D_1(f) \cdot df}, \quad (9)$$

where $\psi(t)$ used was db5, $f_1 = 10$ Hz and $f_2 = 500$ Hz, and D_{\max} in this work was scale 4 [14].

- (c) The WI ratio is between moment -1 at scale 5 and moment 2 at scale 2 (WIRM1522).

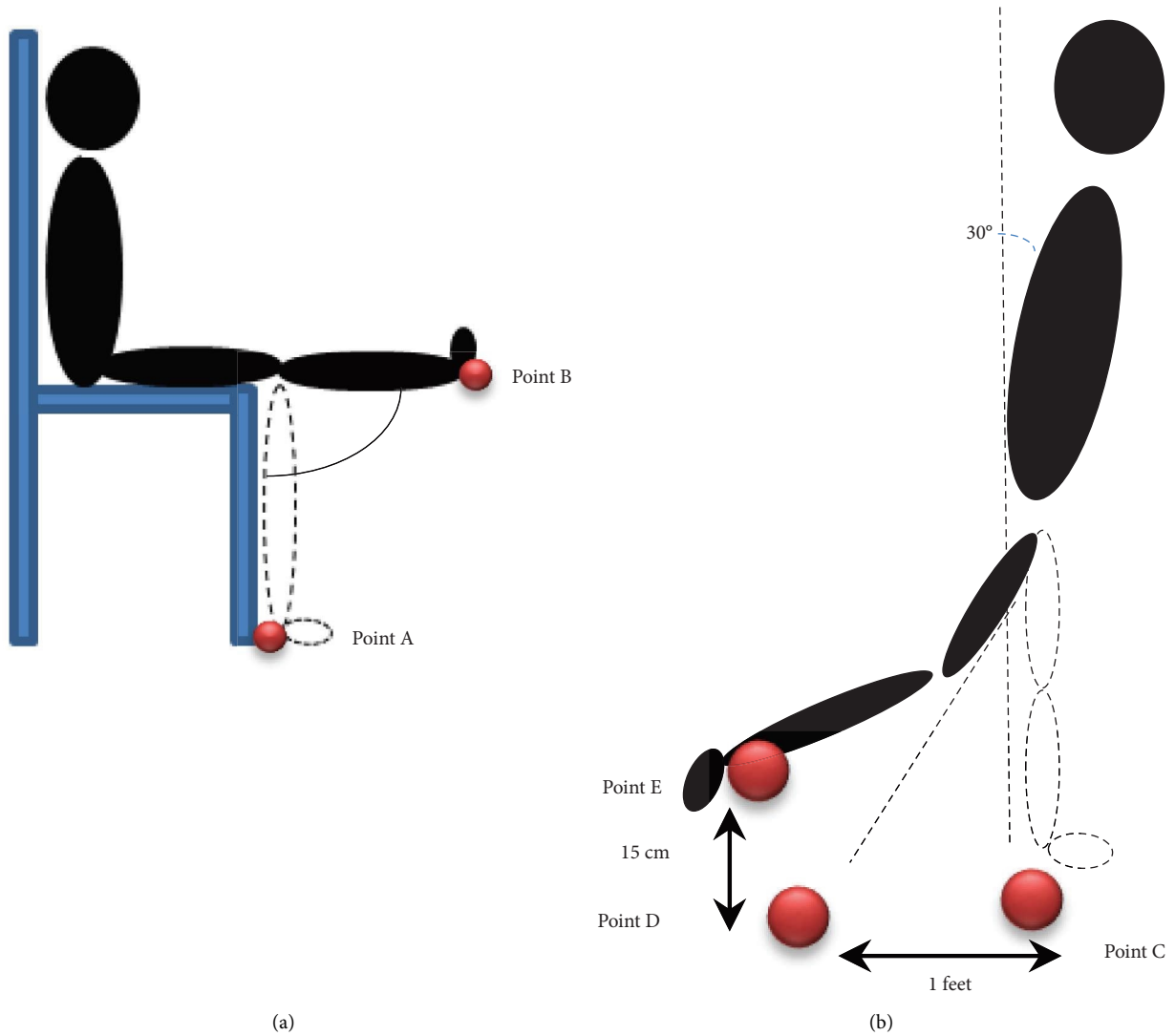


FIGURE 2: Leg movement to activate (a) RF, VL, and VM muscles and (b) BF.

$$\text{WIRM1522} = \frac{\int_{f_1}^{f_2} D_5(f) \cdot df}{\int_{f_1}^{f_2} f^2 D_2(f) \cdot df}, \quad (10)$$

where $\psi(t)$ used was db5 and $f_1 = 10$ Hz and $f_2 = 500$ Hz. [14]

(d) The WI ratio of energy at scales 5 and 1 (WIRE51) is

$$\text{WIRE51} = \frac{\sum_{j=1}^N D_5^2[n]}{\sum_{j=1}^N D_1^2[n]}, \quad (11)$$

where $\psi(t)$ used was sym5 [14].

(e) The WI ratio is between square waveform lengths at different scales (WIRW51).

$$\text{WIRW51} = \frac{\sum_{j=2}^N |D_5[j] - D_5[j-1]|^2}{\sum_{j=2}^N |D_1[j] - D_1[j-1]|^2}, \quad (12)$$

where $\psi(t)$ used was sym5 [14].

During the extraction of WI features, frequency sampling $F_s = 1$ kHz [44] and $n = 1024$ were used. The WI features were then log-transformed to follow the normal distribution.

Fatigue identification always refers to the increment or decrement in the features before and after the activity [45]. The changes and shift of the features (F) in this study were quantified by

$$\Delta F = F_{\text{post}} - F_{\text{pre}}. \quad (13)$$

The positive value of ΔF indicates a feature increment for postexercise, whereas the negative value indicates feature decrements.

2.6. Statistical Analysis. The features of BF, RF, VL, and VM were preliminarily grouped into two categories: normal fatigue (NF) and prolonged fatigue (PF). They

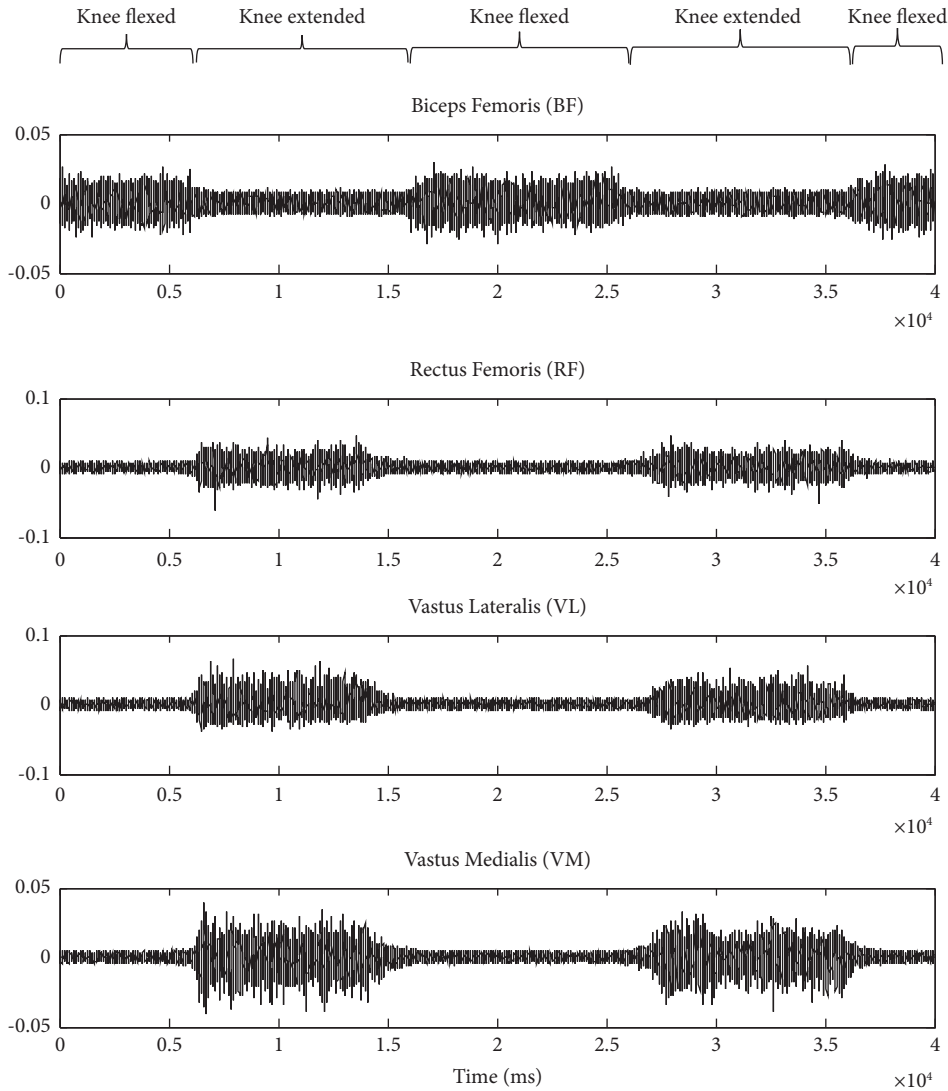


FIGURE 3: Example of sEMG signals collected from BF, RF, VL, and VM.

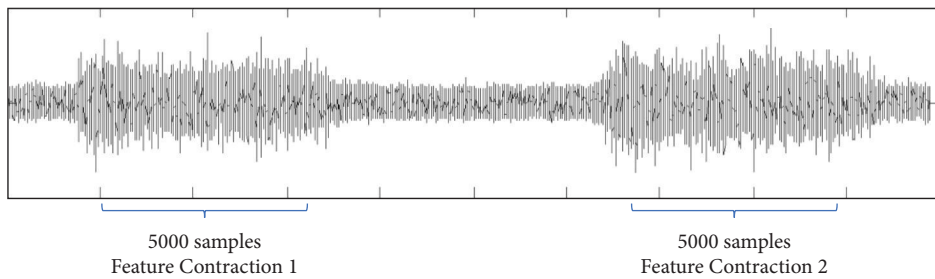


FIGURE 4: Nonoverlapping windowing technique in feature extraction.

were distinguished based on PF signs explained in Table 1. While the features of the participants who did not experience PF conditions were grouped into NF, the features of the participants who experienced PF conditions were grouped into PF. A t -test was conducted, and a significant value was set at $P < 0.05$.

2.7. Daily Plot of Surface EMG Behaviour. The daily plot of sEMG behaviour for NF and PF conditions was performed to investigate the progression of fatigue in different muscles with different activation percentages. It was plotted based on ΔF_{med} and ΔRMS since these two features commonly represent time and frequency information on surface EMG in

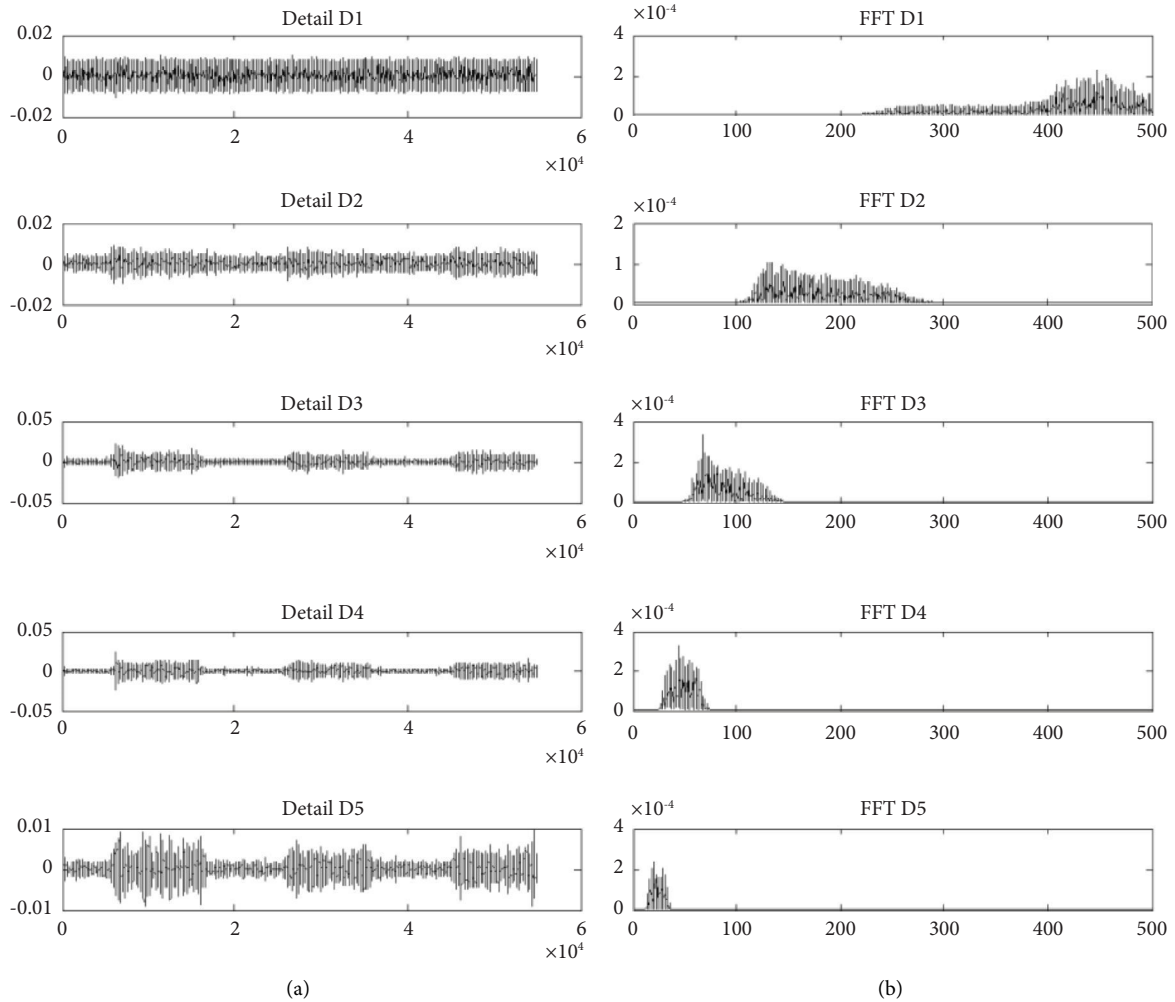


FIGURE 5: (a) sEMG wavelet details at scales 1–5. (b) Power spectra using the Fourier transform of wavelet details at scales 1–5.

fatigue identification. A daily plot was also conducted based on five Δ WI features. To identify the changing behaviour of the features during the emergence of PF, the features were normalized by plotting them from a day before the emergence of PF and the first three days under PF conditions. The reasons were the individual's responses to PF signs that varied, and the normalization will help understand the trend line of sEMG features during the intensive training period specifically under PF conditions.

2.8. Classification. The classification process began with selecting features and reducing the dimension of the features. The classification was performed based on different feature selections to investigate the optimum classification performance based on the selection. The feature selections were based on the following features:

- (a) Time features: Δ MAV and Δ RMS
- (b) Frequency features: ΔF_{med} and ΔF_{mean}
- (c) Time and frequency features: Δ MAV, Δ RMS, ΔF_{med} , and ΔF_{mean}

- (d) Wavelet index features: Δ WIRM1551, Δ WIRM1M51, Δ WIRM1522, Δ WIRE51, and Δ WIRW51

- (e) Time, frequency, and wavelet index features: Δ MAV, Δ RMS, ΔF_{med} , ΔF_{mean} , Δ WIRM1551, Δ WIRM1M51, Δ WIRM1522, Δ WIRE51, and Δ WIRW51

From the feature selection, dimensionality reduction was employed to reduce the complexity and computation time of the classification algorithm, increase accuracy, and decrease overfitting problems [46]. Data reduction in this work was carried out based on linear discriminant analysis (LDA). This method maximizes the intercluster distance between classes and minimizes the intracluster distance within classes in the transformation of reduced features. In LDA, the original dimensional feature space was transformed into a lower dimensional feature space, without losing any important information [46].

In the classification stage, the naïve Bayes (NB) technique was applied to discriminate NF and PF classes. This method was selected as it was previously utilized in experiments studying fatigue classification [36, 37]. NB is one

of the established statistical pattern recognition methods [46]. NB classifier functions are based on the probability distribution of the feature vector, x . x belongs to class ω_m which is computed from probability distribution conditioned on the class ω_m , $P(x|\omega_m)$, by assuming class-conditional independence of the features:

$$P(\mathbf{x} | \omega_m) = \prod_{k=1}^d P(x^{(k)} | \omega_m), \quad (14)$$

where d is a dimension of the feature instance x . Equation (13) requires that the k -th features of the instance, which is $x^{(k)}$, are independent of all other features, given the class information.

The probability of the x class itself is characterized by

$$P(\mathbf{x}) = \prod_{k=1}^d P(x^{(k)}). \quad (15)$$

The classification rule was computed from the discriminant function $g_m(x)$ to represent posterior probabilities as

$$g_m(\mathbf{x}) = P(\omega_m) \prod_{k=1}^d P(y^{(k)} | \omega_m). \quad (16)$$

It was represented for each m -class. Meanwhile, the x class is determined by the largest $g_m(x)$ computation.

In this work, k -fold cross-validation (CV) was adopted for training the classifier. The performance of the classification was evaluated for the accuracy, specificity, precision, and average CV error (CVer).

3. Results and Discussion

3.1. Physiological Measurements. Table 2 shows a daily % HRmax record. It indicates that about 18 participants ran at their maximal effort by showing %HRmax >80%, based on the Edwards Intensity Zone 1992. Running at this rate caused the participants to experience heavy breathing and muscular fatigue. It proves that the Bruce Protocol treadmill test provides the high training intensity required in this experiment. High-intensity exercise is essential for inducing faster PF signs. Physiological fatigue responses under PF conditions are tabulated in Table 3. It shows that the first PF sign developed was muscle soreness, which was on day 2 (D_2) of the assessment. This situation was found to be similar to other studies in [6, 47], whereby soreness developed as early as 24 hours after strenuous exercise.

Table 3 also indicates that PF signs accumulated with performance decrement starting at day 4 (D_4) of intensive training. The results agree with [16] as the untreated PF condition develops more PF signs. Apart from that, the results suggest that only three PF signs appeared within five days of intensive training including soreness and performance decrement. Moreover, the results reveal that these are the earliest signs of PF developed in the study. The result in Table 3 further shows that none of the participants experienced psychological and sleeping disturbance, restlessness,

and hypertension following intensive training. Hence, the classification of collected surface EMG signal features was based on physiological responses identified in Table 3. The term PF condition afterward refers to muscle soreness, performance decrement, and lethargy.

3.2. Surface Electromyography. The daily plot of sEMG feature behaviour is displayed in Figure 6, while the bar plot represents standard deviation, “o,” and “x,” symbols represent the mean value of features in NF and PF conditions, respectively. The features under NF conditions were plotted from day 1 to day 5 (D_1 – D_5) of the assessment, whereas the plots under PF conditions were normalized from the day before the emergence of PF (D_{NF}) to the first three days of the occurrence of PF signs (D_1 – D_3).

3.2.1. Frequency Feature. Theoretically, the frequency information changes in sEMG describe the behaviour of conduction velocities inside the muscle and subsequent changes in the duration of the motor unit action potential waveform and fluctuation of muscle force and muscle fibre types as well as their decomposition [8, 9]. The frequency spectrum shift information is represented by its mean (F_{mean}) and median (F_{med}) in assessing muscle fatigue [42].

Figure 6 shows that ΔF_{med} resulted in a negative value for BF, RF, VL, and VM under NF conditions. The negative values of ΔF_{med} demonstrate that F_{med} was decreasing postrunning activities. The decrement in F_{med} was like the most dominant opinion where frequency tends to shift to a lower value to characterize fatigue. The decrease in the centre of frequency as a result of reduced muscle conduction velocity and a change in the frequency spectrum was brought on by the absence of high threshold motor unit recruitment. However, ΔF_{med} shows positive values for BF, VL, and VM on day 4 (D_4) and day 5 (D_5) under the NF condition. The positive values of ΔF_{med} indicate that the median frequency spectrum was shifted upwards. An increase in F_{med} was also identified on the day before PF signs appeared (D_{NF}) for the BF, VL, and VM muscles, and this behaviour was sustained throughout the PF condition.

The plot in Figure 6 also indicates that the positive values of ΔF_{med} only occurred in RF during PF conditions. Statistical analysis reveals that an increment in ΔF_{med} under PF is significant at $P < 0.05$ for BF, RF, VL, and VM, as tabulated in Table 4. An increase in F_{med} of sEMG during fatigue was rarely reported. The increasing center of frequency was once reported by [48] during the first 30 minutes of recovery from dynamic exercise at a load of 80% of the VO_2 max. The increasing center of the frequency was reported following the elevation of temperature and lactate after high-intensity dynamic exercise [48]. The relationship between the skin and muscle temperature and the increasing center of the sEMG frequency spectrum was later confirmed in [49]. The positive linear relationship between the temperature and median frequency might be due to an increase in the muscle conduction velocity to increase the power output [49, 50]. The relationship between the frequency of sEMG and temperature was also discussed in [51].

TABLE 2: Intensity of training based on percentage of the maximal heart rate.

Intensity zone % HRmax	Day_1	Day_2	Day_3	Day_4	Day_5
Very hard 90–100	10	8	8	11	10
Hard 80–89	8	9	7	5	4
Moderate 70–79	—	1	3	2	1
Light < 69	2	2	2	2	2
Mean \pm SD	86 \pm 13	86 \pm 12	84 \pm 14	85 \pm 15	87 \pm 14

In [51], the authors demonstrated that there is a less effect of temperature on muscle strength and frequency of sEMG but related other possibilities that affected the frequency features such as different recruitment properties of the motor units and the percent of fast and slow twitch motor units under electrodes. Heavy dynamic exercise might also contribute to the substitution of muscle groups following an effect on the alpha motor neuron pool through reflex inhibition that alters recruitment properties. The effect of the neural drive on the muscle and its motor unit action potential was also identified as one of the factors that affect sEMG components [52].

The neural drive for the muscle factor might be related to fatigue induced in the peripheral and central systems. Fatigue in the central system occurs when neurochemical in the brain is altered and stress hormones are secreted. When this happens, it will modify the peripheral information in the contracting muscles and affect the characteristic of sEMG [53–56].

The increment in frequency information features ΔF_{med} under PF conditions also might be due to fatigue at the peripheral system. Fatigue at the peripheral system arises from the muscle itself when there is impairment of the peripheral mechanism due to high-intensity exercise as demonstrated by participants in this experiment [45, 49, 50]. High-intensity exercise reduces blood flow due to intense muscle contraction which causes the inadequacy of oxygen supply to the muscle. This situation is also known as an anaerobic condition [54]. The inability to get enough oxygen triggers a biochemical reaction in allowing muscle contraction [57, 58]. An inadequate recovery period causes the inability of ionic alteration during high-intensity exercise to return to its normal level and continue to accumulate. This situation is signified by the emerging PF signs such as soreness and performance decrement. The ionic changes most probably involve glycogen breakdown and the presence of lactate concentration. It is supported by the recorded %HRmax during the running activity, of which 80% and above commonly involves anaerobic contraction. In anaerobic contraction, glycogen and lactate concentration play important roles in ensuring muscle continuous contraction [57, 58]. Furthermore, the alteration in glycogen stores normally leads to soreness and performance decrement due to inadequate fuel for workload [22, 31], and the release of lactate contributes to fatigue and muscle pain, as experienced by the participants in this study. This situation is supported in [31, 48] that also demonstrated that the

alteration of both concentrations led the frequency of sEMG to shift to the upper value.

Figure 6 also demonstrates that there were different increment trends in ΔF_{med} among the investigated muscles. The trends that happened might be related to muscle activation during running activity. Running at a higher slope such as in the Bruce Protocol treadmill test requires more muscle activation from BF, VL, and VM than from RF, as demonstrated in [36, 37]. A previous study shows that more muscle activation leads to faster progression of fatigue [59]. This study has demonstrated that changes in ΔF_{med} happen faster in more activated muscles than in less activated ones. The fast changes in the frequency made the observation of PF signs through more activated muscles rather difficult. The reason was the frequency feature increased even without the emergence of PF signs. Indirectly, an increase in the median frequency might be due to an increase in the muscle temperature and muscle conduction velocity to increase the power output, substitution of the muscle group and recruitment properties, and alteration of ionic concentration underlying the muscle that progressed faster in muscle activation during running. This study has also proved that PF conditions could be easily observed from less activated muscles such as RF because the increment in frequency only occurred under PF conditions. It indicates that PF can be easily identified when frequency from less activated muscles starts to increase.

3.2.2. Time Features. Muscle activity can be observed through its amplitude during the contraction in time-domain representations. In fatigue identification, changes in its amplitude signify the degree of fatigue experienced by the subjects. As exhibited in Figure 6, ΔRMS of BF, RF, and VM under NF conditions increased on D₁ and decreased on the following days. This progression is similar to dominant opinions that with an increment in amplitude, the decrement in behaviour in characterizing the degree of fatigue soon follows [10].

However, the ΔRMS increased again, as shown in D₅, in the BF and VM muscles (Figure 6). Theoretically, in normal conditions, when the load increases, the amplitude tends to have a larger decrement. In this study, the load refers to the endurance time, for which the participants were asked to improve their performance daily. Based on the plot of ΔF_{med} on similar days D₅ on BF and VM, the median frequency shows an increment. In the previous section, the increments in ΔF_{med} were related to an increase in temperature. However, the findings in [48, 49] have shown that the increment in the muscle and skin temperature will reduce the amplitude of sEMG signals. The increment in ΔRMS indicated by the BF and VL muscles in D₅ might be due to the release of free-resting calcium which resulted in force potentiation and led to the increment in EMG, as demonstrated by [60].

The increment in ΔRMS especially under PF might also be due to the changes in ionic concentration. The changes in the ionic concentration were observed through frequency feature behaviour in the previous section. The

TABLE 3: Number of participants under prolonged fatigue conditions based on physiological responses.

	Day 1	Day 2	Day 3	Day 4	Day 5
Performance improvement		20	20	17	12
Performance decrement		—	—	3	5
Muscle scale	1 (excellent)	2	1	1	1
	2 (very good)	6	5	4	3
	3 (good)	12	12	10	11
	4 (tender, but not sore)	—	1	3	4
	5 (sore)	—	1	2	2
Psychology score <14	20	20	20	20	20
No sleeping disturbance	20	20	20	20	20
No lethargy	20	20	17	16	15
Lethargy	—	—	3	4	5
HR before run <100	20	20	20	20	20
BP before run <140/90	20	20	20	20	20

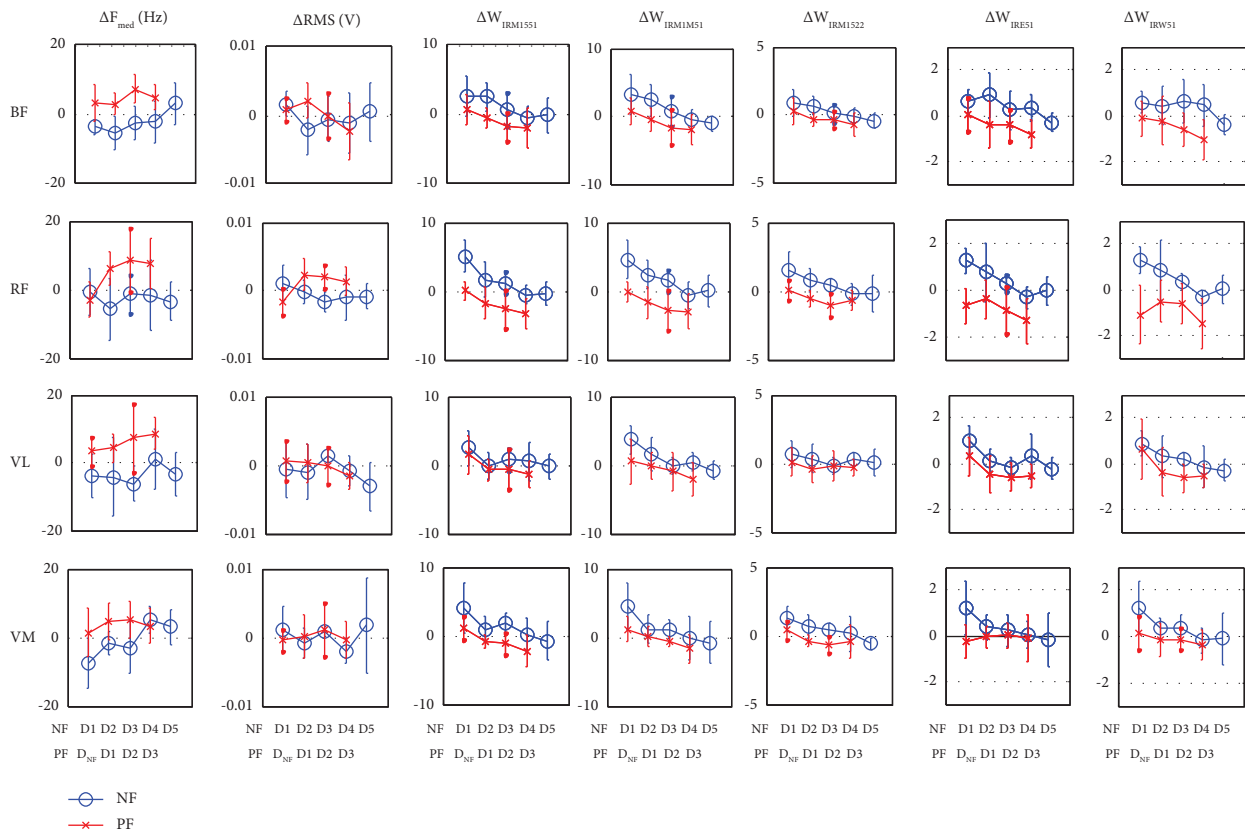


FIGURE 6: Daily plot of changes in muscle features under NF and PF conditions.

findings in [61] reported that there was a curvilinear positive relationship between lactate concentration (after reaching a certain lactate threshold) and the amplitude of sEMG.

Apart from that, Figure 6 discloses that ΔRMS started to decrease again on D_2 of PF, specifically in BF and VL. The decrement in ΔRMS under PF conditions was discovered in [31, 62]. Both studies have proved that amplitude decreases during the emergence of soreness. Nevertheless, another study reveals that the amplitude increases under similar conditions [63]. Therefore, it is reliable to state that the amplitude increases or decreases under PF conditions. The

increment and decrement in amplitude under PF also show the degree of fatigue experienced by the muscle. This is attributed to the decrement in amplitude under PF which occurred in highly activated muscles like BF, VL, and VM. High activation led to the fast progression of fatigue. It began when the frequency features started to increase, followed by the amplitude which also increased. Then, it continued with the decreased behaviour to show a certain degree of fatigue experience. This finding was also supported by the progression of fatigue mapped on RF, which was less activated in the study. Figure 6 demonstrates that the RF muscle under NF conditions for ΔRMS continued to decrease (by showing

TABLE 4: Statistical analysis on the four muscle features.

Muscles		Features (mean \pm SD)								
		ΔF_{mean}	ΔF_{med}	ΔMAV	ΔRMS	Δ WIRM1551	Δ WIRM1M51	Δ WIRM1522	Δ WIRE51	ΔWIRW51
Biceps femoris	NF	*-2.04 (10.4)	*-0.45 (9.74)	-0.00034 (0.003)	-0.00043 (0.004)	*0.80 (2.36)	*0.75 (2.33)	0.09 (0.82)	*0.24 (0.78)	*0.22 (0.80)
	PF	7.55 (8.23)	5.11 (6.46)	-0.00033 (0.0028)	-0.00049 (0.0037)	-0.70 (2.69)	-0.80 (2.30)	-0.22 (0.85)	-0.27 (0.92)	-0.34 (0.98)
Rectus femoris	NF	*-4.67 (9.91)	*-2.37 (6.67)	*-0.00061 (0.0018)	*-0.00066 (0.0024)	*1.02 (2.60)	*1.03 (2.64)	*0.36 (1.11)	*0.10 (1.02)	*0.10 (1.13)
	PF	5.77 (10.22)	6.43 (8.56)	0.001388 (0.0020)	0.0017 (0.0024)	-2.29 (2.51)	-2.36 (2.61)	-0.75 (0.76)	-0.66 (1.01)	-0.74 (1.14)
Vastus lateralis	NF	*-2.07 (8.45)	*-2.15 (9.00)	-0.00038 (0.0022)	-0.00054 (0.0029)	0.40 (2.74)	*0.66 (2.66)	0.17 (0.94)	*0.13 (0.87)	0.11 (0.88)
	PF	6.34 (7.85)	4.64 (7.58)	-0.00052 (0.0024)	-0.00064 (0.0031)	-0.59 (2.38)	-0.60 (2.41)	-0.21 (0.83)	-0.26 (0.85)	-0.25 (0.92)
Vastus medialis	NF	*-0.75 (7.59)	*-0.30 (7.42)	0.0001 (0.002)	0.0001 (0.003)	0.58 (2.74)	0.54 (3.17)	0.24 (1.02)	0.12 (0.96)	0.11 (0.95)
	PF	4.06 (4.81)	4.28 (5.77)	0.00022 (0.0024)	0.000246 (0.0032)	-0.330 (1.75)	-0.38 (1.73)	-0.10 (0.96)	-0.02 (0.66)	-0.01 (0.58)

*The differences differ significantly tested using the t -test at $P < 0.05$.

a negative value) and only increased for ΔRMS under PF conditions. The transition behaviour of ΔRMS in the RF muscle was actually similar to that of the ΔF_{med} situation, whereby the shifts (from decreasing to increasing) only occurred under PF conditions. The behaviour of ΔRMS for the RF muscle, which decreased under NF and increased under PF conditions, is statistically significant at $P < 0.05$ (Table 4). The statistical test also indicates that the behaviour of ΔRMS under both conditions for BF, VL, and VM is not significant at $P < 0.05$ due to the fluctuation trend in the daily plot (see Figure 6).

3.2.3. Wavelet Indices. This study also investigates the ability of WI features in PF identification. The five WI features were studied, as proposed by [43]. WI features tended to have similar behaviour and response to BF, RF, VL, and VM, as observed in Figure 6. They also tended to increase under NF conditions and decrease under PF conditions.

Figure 6 for $\Delta \text{WIRM1551}$, $\Delta \text{WIRM1M51}$, and $\Delta \text{WIRM1522}$ illustrates the transition of the increment and decrement in WI features under NF conditions. It is also important to note that the features were constantly decreased under PF conditions. The increment (positive value) in WI features under NF in Figure 6 is similar to the results demonstrated in [17]. The increment in the features specifies that the energy distribution shifted to a lower frequency band indicating similar behaviour of frequency, which tended to decrease to show fatigue conditions [10].

Figure 6 also demonstrates that the increment and decrement transitions occurred faster in high-activated muscles such as BF and VL. These situations can be observed under NF conditions on D_4 and D_5 for $\Delta \text{WIRM1551}$, $\Delta \text{WIRM1M51}$, and $\Delta \text{WIRM1522}$. $\Delta \text{WIRM1551}$, $\Delta \text{WIRM1M51}$, and $\Delta \text{WIRM1522}$ features also demonstrate that PF could be easily identified in RF, as it occurred on the ΔF_{med} and ΔRMS daily plot. The decrement in ΔWI features

was caused by energy distribution which slowly shifted to a higher frequency band, which caused the energy distribution at the lower frequency band of decomposition to decrease.

The WIRE51 feature was quantified in accord with its coefficient details D of decomposition. The increment in ΔWIRE51 features showed a higher value of D at level 5 postexercise than preexercise. Figure 6 indicates that similar trends also appeared in another daily plot of WI features, of which $\Delta \text{W}_{\text{IRE51}}$ gradually decreased under NF plots. Furthermore, the value constantly decreased under PF conditions. Although D indicates the time representation of decomposition, ΔWIRE51 proved that the behaviour of the features did not rapidly fluctuate as demonstrated by ΔRMS behaviour. The robustness and sensitivity of WI in dealing with nonstationary behaviour in sEMG were exhibited.

ΔWIRW51 was used to show accumulated changes in the waveform length ratio at D level 5 to D level 1. Through waveform length behaviour, the duration, frequency, and amplitude of the surface EMG signals were effectively compressed [17]. The increment in ΔWIRW51 in Figure 6 under NF suggests that the surface EMG waveform fluctuated faster postexercise than preexercise. The features gradually decreased to indicate the fluctuation of the surface EMG waveform at D level 5 which was getting slower during postexercise. ΔWIRW51 persistently decreased under PF conditions. Hence, it signifies that, apart from the amplitude and energy distribution in the spectra, the waveform characteristic of surface EMG also changed due to PF.

Although BF, RF, VL, and VM demonstrate similar behaviour of WI features under NF and PF conditions, statistical results indicate that all five ΔWI features are only significant at $P < 0.05$ for the RF muscle, as tabulated in Table 4.

3.3. Classification. Table 5 indicates the classification results based on the NB method in identifying PF conditions. This result reveals the ability of sEMG features to distinguish

TABLE 5: Classification results of prolonged fatigue based on the naïve Bayes method.

Features	Parameter	Muscles			
		Performance	BF	RF	VL
Time features (ΔMAV , ΔRMS)	Accuracy (%)	70	78	64	56
	Specificity (%)	100	84	83	97
	Precision (%)	0	67	36	0
	CVErr	0.31	0.25	0.43	0.44
Frequency features (ΔF_{med} , ΔF_{mean})	Accuracy (%)	86	95	68	77
	Specificity (%)	88	94	89	83
	Precision (%)	79	96	36	69
	CVErr	0.15	0.04	0.39	0.23
Time and frequency features (ΔMAV , ΔRMS , ΔF_{med} , ΔF_{mean})	Accuracy (%)	94	98	95	97
	Specificity (%)	97	100	100	97
	Precision (%)	86	96	88	96
	CVErr	0.06	0.01	0.07	0.02
Wavelet index features ($\Delta WIRM1551$, $\Delta WIRM1M51$, $\Delta WIRM1522$, $\Delta WIRE51$, $\Delta WIRW51$)	Accuracy (%)	82	91	80	66
	Specificity (%)	85	93	78	71
	Precision (%)	77	89	84	58
	CVErr	0.18	0.09	0.23	0.38
Time, frequency, and wavelet index features (ΔMAV , ΔRMS , ΔF_{med} , ΔF_{mean} , $\Delta WIRM1551$, $\Delta WIRM1M51$, $\Delta WIRM1522$, $\Delta WIRE51$, $\Delta WIRW51$)	Accuracy	87	88	77	90
	Specificity	86	91	79	83
	Precision	89	85	80	100
	CVErr	0.16	0.15	0.23	0.2

between NF and PF based on the naïve Bayes (NB) classification method. Table 5 tabulates the lowest accuracy results from time features of BF, VL, and VM, due to fast fluctuation and overlapping plots of time feature values displayed in Figure 6. This condition makes predicting PF conditions through these features quite difficult. The results revealed in Table 5 indicate that the frequency features had better classification accuracy than time features. Better accuracy was assisted by the significant statistical test results and daily plots to distinguish between NF and PF of frequency features.

The results in Table 5 reveal that the feature selection based on time and frequency offers high-performance accuracy, specificity, and precision in comparison with other feature selections. Thus, it can be concluded that both the time and frequency features of sEMG are significant for PF identification. In this study, the combination of time and frequency feature selections offers accuracy at a rate of 94% on BF, 98% on RF, 95% on VL, and 98% on VL in distinguishing PF conditions. The classification of performances in Table 5 proves the ability of WI features in PF detection. The result shows that WI features produced good classification accuracy in BF (82%), RF (91%), and VL (80%) and less in VM (66%).

4. Conclusions

In conclusion, this study has demonstrated that the presence of PF can be identified using the surface EMG signals. The study also introduced a new quantitative noninvasive method to monitor the progression of fatigue, specifically in the muscle of athletes. This monitoring method can provide

information to athletes on their performance, and they can perform at their optimum energy. This noninvasive method is suitable to be applied in the sports field for fatigue management and prevent chronic fatigue syndrome for athletes.

Data Availability

The surface electromyography physiology data used to support the findings of this study have not been made available because they involve the third-party right and participant privacy.

Conflicts of Interest

The authors declare that there are no conflicts of interest regarding the publication of this paper.

Acknowledgments

This work was supported by Universiti Putra Malaysia under IPS Putra Grant.

Supplementary Materials

Table S1: schedule of the experiment. Table S2: Bruce Protocol treadmill test. Table S3: prolonged fatigue sign identification. Table S4: quadriceps muscle movement based on the flexed and extended knee. Appendix S1: PAR-Q and You. Appendix S2: training log data collection form. Appendix S3: 24-hour history training distress questionnaire. Figure S1: flowchart of the experimental procedure and data

collection. Figure S2: schematic circuit of the surface EMG data acquisition system. (*Supplementary Materials*)

References

- [1] E. J. D. J. H. Nagel, Bronzino, and B. Amplifiers, *The Biomedical Engineering Handbook*, CRC Press LLC, Boca Raton, FL, USA, 2000.
- [2] N. A. Mohd Ishak, P. I. Khalid, N. H. Mahmood, and M. Harun, "Determination of epoch length and regression model for 15-second segment of SEMG signal used in joiny analysis of spectrum and amplitude," *Jurnal Teknologi*, vol. 5, no. 78, pp. 7–13, 2016.
- [3] J. B. Dingwell, J. E. Joubert, F. Diefenthaler, and J. D. Trinity, "Changes in muscle activity and kinematics of highly trained cyclists during fatigue," *IEEE Transactions on Biomedical Engineering*, vol. 55, no. 11, pp. 2666–2674, 2008.
- [4] M. Z. C. Hassan, P. I. K.-I. Member, N. A. Kamaruddin, and N. A. Ishak, "Derivation of Simple Muscle Fatigue Index for Biceps Muscle Based on Surface Electromyography Temporal Characteristics," in *Proceedings of the IEEE Conference on Biomedical Engineering and Sciences*, pp. 8–10, Kuala Lumpur, Malaysia, December 2014.
- [5] I. Cosic, S. L. Giudice, J. Hawley, D. K. Kumar, and V. P. Singh, "Strategies to identify changes in SEMG due to muscle fatigue during cycling," in *Proceedings of the 27th Annual Conference IEEE Engineering in Medicine and Biology Shanghai, China*, 2005.
- [6] N. Hedayatpour, D. Falla, L. Arendt-Nielsen, and D. Farina, "Effect of delayed-onset muscle soreness on muscle recovery after a fatiguing isometric contraction," *Scandinavian Journal of Medicine & Science in Sports*, vol. 20, no. 1, pp. 145–153, 2010.
- [7] D. H. Gates, *The Role of Muscle Fatigue on Movement Timing and Stability during Repetitive Tasks*, University of Texas, Austin, TX, USA, 2009.
- [8] M. González-Izal, A. Malanda, E. Gorostiaga, and M. Izquierdo, "Electromyographic models to assess muscle fatigue," *Journal of Electromyography and Kinesiology*, vol. 22, no. 4, pp. 501–512, 2012.
- [9] E. J. Kupa, S. H. Roy, S. C. De Luca, C. J. Kupa, S. H. Roy, and S. C. Kandarian, "Effects of muscle fiber type and size on EMG median frequency and conduction velocity," *Journal of Applied Physiology*, vol. 79, no. 1, pp. 23–32, 1995.
- [10] N. A. Dimitrova and G. Dimitrov, "Interpretation of EMG changes with fatigue: facts , pitfalls , and fallacies," *Journal of Electromyography and Kinesiology*, vol. 13, no. 1, pp. 13–36, 2003.
- [11] M. González-Izal, A. Malanda, I. Navarro-Amezqueta et al., "EMG spectral indices and muscle power fatigue during dynamic contractions," *Journal of Electromyography and Kinesiology*, vol. 20, no. 2, pp. 233–240, 2010.
- [12] T. Moritani and M. Muro, "Motor unit activity and surface electromyogram power spectrum during increasing force of contraction," *European Journal of Applied Physiology and Occupational Physiology*, vol. 56, no. 3, pp. 260–265, 1987.
- [13] S. Cobb and A. Forbes, "Electromyographic studies of muscular fatigue in man," *American Journal of Physiology-Legacy Content*, vol. 65, no. 2, pp. 234–251, 1923.
- [14] M. González-Izal, I. Rodriguez-Carreno, A. Malanda et al., "sEMG wavelet-based indices predicts muscle power loss during dynamic contractions," *Journal of Electromyography and Kinesiology*, vol. 20, no. 6, pp. 1097–1106, 2010.
- [15] J. R. Potvin and L. R. Bent, "A validation of techniques using surface EMG signals from dynamic contractions to quantify muscle fatigue during repetitive tasks," *Journal of Electromyography and Kinesiology*, vol. 7, no. 2, pp. 131–139, Jun. 1997.
- [16] L. Arendt-Nielsen and T. Sinkjær, "Quantification of human dynamic muscle fatigue by electromyography and kinematic profiles," *Journal of Electromyography and Kinesiology*, vol. 1, no. 1, pp. 1–8, 1991.
- [17] A. Malanda and M. Izquierdo, "New wavelet indices to assess muscle fatigue during dynamic contractions," *World Academy of Science, Engineering and Technology*, vol. 3, pp. 456–461, 2009.
- [18] P. Z. Pearce, "A practical approach to the overtraining syndrome," *Current Sports Medicine Reports*, vol. 1, no. 3, pp. 179–183, 2002.
- [19] C.-Y. Guezennec, "Review overtraining syndrome," *Bulletin de l'Académie nationale de médecine*, vol. 188, no. 6, pp. 923–931, 2004.
- [20] J. C. Ka Brooks, "Overtraining, exercise, and adrenal insufficiency," *Journal of Novel Physiotherapies*, vol. 3, no. 125, pp. 1–10, 2013.
- [21] A. E. Jeukendrup, "Overtraining: how to monitor and how to prevent?" *Sport Nutrition Conference*, vol. 5, pp. 12–15, 2010.
- [22] H. Ishii and Y. Nishida, "Effect of Lactate Accumulation during Exercise-induced Muscle Fatigue on the Sensorimotor Cortex," *Journal of Physical Therapy Science*, vol. 25, no. 12, pp. 1637–1642, 2013.
- [23] K. M. Myrick and D. N. P. Aprn, "Syndrome in Overtraining and Overreaching Syndrome in Athletes," *The Journal for Nurse Practitioners*, vol. 11, no. 10, pp. 1018–1022, 2015.
- [24] C. Y. Guezennec, "Overtraining [Overtraining syndrome].yndrome," *Bulletin de l'Académie nationale de médecine*, vol. 188, no. 6, pp. 923–930, 2004.
- [25] M. Hug, P. E. Mullis, M. Vogt, N. Ventura, and H. Hoppeler, "Training modalities: over-reaching and over-training in athletes , including a study of the role of hormones," *Best Practice & Research Clinical Endocrinology & Metabolism*, vol. 17, no. 2, pp. 191–209, 2003.
- [26] J. B. Kreher and J. B. Schwartz, "Overtraining Overtraining Syndrome: a practical guide," *Sports Health: A Multidisciplinary Approach*, vol. 4, no. 2, pp. 128–138, 2012.
- [27] R. Meeusen, M. Duclos, C. Foster et al., "European College of Sport Science, American College of Sports Medicine. Prevention, diagnosis, and treatment of the overtraining syndrome: joint consensus statement of the European College of Sport Science and the American College of Sports Medicine," *Medicine and science in sports and exercise*, vol. 45, no. 1, pp. 186–205, 2013.
- [28] D. Purvis, S. Gonsalves, and P. A. Deuster, "Physiological and psychological fatigue in extreme conditions: overtraining and elite athletes," *PM&R: The Journal of Injury, Function, and Rehabilitation*, vol. 2, no. 5, pp. 442–450, 2010.
- [29] V. P. Singh, "Strategies to identify muscle fatigue from SEMG during cycling," in *Proceedings of the 2004 Intelligent Sensors, Sensor Networks and Information Processing Conference*, pp. 547–552, Melbourne, Australia, December 2004.
- [30] M. Haddad, A. Chaouachi, D. P. Wong et al., "Influence of fatigue, stress, muscle soreness and sleep on perceived exertion during submaximal effort," *Physiology & Behavior*, vol. 119, pp. 185–189, 2013.
- [31] J. P. Gavin, S. D. Myers, and M. E. T. Willems, "Neuro-muscular responses to mild-muscle damaging eccentric

- exercise in a low glycogen state," *Journal of Electromyography and Kinesiology*, vol. 25, no. 1, pp. 53–60, 2015.
- [32] K. Birch and K. George, "Overtraining the female athlete," *Journal of Bodywork and Movement Therapies*, vol. 3, no. 1, pp. 24–29, 1999.
- [33] S. M. Fox, J. P. Naughton, and W. L. Haskell, "Physical activity and the prevention of coronary heart disease," *Annals of Clinical Research*, vol. 3, no. 6, pp. 404–432, 1971.
- [34] G. Borg, *An Introduction to Borg's RPE-Scale*, Movement Publication, New York, 1985.
- [35] D. R. Armfield, D. H. M. Kim, J. D. Towers, J. P. Bradley, and D. D. Robertson, "Sports-related muscle injury in the lower extremity," *Clinics in Sports Medicine*, vol. 25, no. 4, pp. 803–84242, Oct. 2006.
- [36] M. A. Sloniger, K. J. Cureton, B. M. Prior, and E. M. Evans, "Lower extremity muscle activation during horizontal and uphill running," *Journal of Applied Physiology*, vol. 83, no. 6, pp. 2073–2079, 1997.
- [37] W. B. Edwards, "Biomechanics and Physiology of Uphill and Downhill Running," *Sports Medicion*, pp. 1–16, 2016.
- [38] D. Stegeman and H. Hermens, "Standards for Surface Electromyography: The European Project Surface EMG for Non-invasive Assessment of Muscles (SENIAM)," 2007, <http://www.seniam.org/%5Cnhttp://www.med.uni-jena.de/motorik/pdf/stegeman.pdf>.
- [39] E. Kwatny, D. H. Thomas, and H. G. Kwatny, "An application of signal processing techniques to the study of myoelectric signals," *IEEE Transactions on Biomedical Engineering*, vol. 17, no. 4, pp. 303–31313, 1970.
- [40] P. Konrad, "The ABC of EMG: A Practical Introduction to Kinesiological Electromyography. Noraxon Inc., Scottsdale, AZ, USA," 2005.
- [41] G. Pioggia, G. Tartarisco, G. Ricci, L. Volpi, G. Siciliano, and S. Bonfiglio, "A wearable pervasive platform for the intelligent monitoring of muscular fatigue," in *Proceedings of the 2010 10th International Conference On Intelligent Systems Design And Applications*, pp. 132–135, Cairo, Egypt, November 2010.
- [42] A. Phinyomark, S. Thongpanja, and H. Hu, "The usefulness of mean and median frequencies in electromyography analysis," *Computational Intelligence in Electromyography Analysis-A Perspective on Current Applications and Future Challenges*, vol. 23, pp. 195–220, 2012.
- [43] A. June, M. Cifrek, V. Medved, and S. Tonkovic, "Surface EMG Based Muscle Fatigue Evaluation in Biomechanics," *Clinical Biomechanics*, 2009.
- [44] M. Sarillee et al., "Classification of muscle fatigue condition using," *IEEE International Conference on Control System, Computing and Engineering*, pp. 27–29, 2015.
- [45] S. Kattla and M. M. Lowery, "Fatigue related changes in electromyographic coherence between synergistic hand muscles," *Experimental Brain Research*, vol. 202, no. 1, pp. 89–99, Apr. 2010.
- [46] R. Polikar, *Pattern Recognition*, pp. 1–22, Wiley Encyclopedia of Biomedical Engineering, New Jersey, NJ, USA, 2006.
- [47] A. McKune, S. Semple, and E. Peters-Futre, "Acute exercise-induced muscle injury," *Biology of Sport*, vol. 29, no. 1, pp. 3–10, 2012.
- [48] J. S. Petrofsky, "Applied Frequency and amplitude analysis of the EMG during exercise on the bicycle ergometerphysiology during exercise on the bicycle ergometer," *European Journal of Applied Physiology and Occupational Physiology*, vol. 41, no. 1, pp. 1–15, 1979.
- [49] D. Stewart, A. Macaluso, and G. De Vito, "The effect of an active warm-up on surface EMG and muscle performance in healthy humans," *European Journal of Applied Physiology*, vol. 89, no. 6, pp. 509–513, 2003.
- [50] K. Watanabe, T. Sakai, S. Kato et al., "Conduction Velocity of Muscle Action Potential of Knee Extensor Muscle During Evoked and Voluntary Contractions After Exhaustive Leg Pedaling Exercise.elocity of muscle action potential of knee extensor muscle during evoked and voluntary contractions after exhaustive leg pedaling exercise," *Frontiers in Physiology*, vol. 11, pp. 546–8, 2020.
- [51] J. Petrofsky and M. Laymon, "The relationship between muscle temperature , MUAP conduction velocity and the amplitude and frequency components of the surface EMG during isometric contractions," *Basic and Applied Myology*, vol. 15, no. 2, pp. 61–74, 2005.
- [52] D. Farina, R. Merletti, and R. M. Enoka, "The extraction of neural strategies from the surface EMG: The extraction of neural strategies from the surface EMG: an updaten update," *Journal of Applied Physiology*, vol. 117, no. 11, pp. 1215–1230, 2014.
- [53] B. Sesboué and J.-Y. Guincestre, "Muscular fatigue," *Annales de Réadaptation et de Médecine Physique: revue scientifique de la Societe francaise de reeducation fonctionnelle de readaptation et de medecine physique*, vol. 49, no. 6, pp. 257–264, 2006.
- [54] M. P. Davis, D. Walsh, and F. Edin, "Mechanisms of fatigue," *Journal of Supportive Oncology*, vol. 8, no. 4, pp. 164–174, 2010.
- [55] S. C. C. Gandevia, "Spinal and Spinal and Supraspinal Factors in Human Muscle Fatigueupraspinal factors in human muscle fatigue," *Physiological Reviews*, vol. 81, no. 4, pp. 1725–1789, 2001.
- [56] S. Zakyntinos and C. Roussos, "Respiratory muscle fatigue," *Physiologic Basis of Respiratory Disease*, vol. 9, pp. 289–306, 2005.
- [57] M. S. Tenan, J. T. Blackburn, and G. Robert, "Exercise-induced glycogen reduction increases muscle activity," *International Journal of Exercise Science*, vol. 9, no. 3, pp. 336–346, 2016.
- [58] J. Finsterer, "Biomarkers of peripheral muscle fatigue during exercise," *BMC Musculoskeletal Disorders*, vol. 13, no. 1, p. 218, 2012.
- [59] C. Hernandez, E. Estrada, L. Garcia, G. Sierra, and H. Nazeran, "Traditional SEMG fatigue indicators applied to a real-world sport functional activity: roundhouse kick," *Electronics, Communications and Computer*, vol. 55, pp. 154–158, 2010.
- [60] T. I. Arabadzhiev, V. G. Dimitrov, and G. V. Dimitrov, "The increase in surface EMG could be a misleading measure of neural adaptation during the early gains in strength," pp. 1645–1655, 2014.
- [61] C. T. Candotti, J. Loss, M. Melo et al., "Comparing the lactate and EMG thresholds of recreational cyclists during incremental pedaling exercise," *Canadian Journal of Physiology and Pharmacology*, vol. 86, no. 5, pp. 272–278, 2008.
- [62] H. Nie, L. Arendt-nielsen, A. Kawczynski, and P. Madeleine, "Gender effects on trapezius surface EMG during delayed onset muscle soreness due to eccentric shoulder exercise," *Journal of Electromyography and Kinesiology*, vol. 17, no. 4, pp. 401–409, 2007.
- [63] H. A. D. Vries, "Quantitative electromyographic investigation of the spasm theory of muscle pain," *Journal of Physical Medicin*, vol. 45, p. 119, 1967.